



**HAL**  
open science

# Thermoelectric phenomena in superconducting nanostructures

Angelo Di Marco

► **To cite this version:**

Angelo Di Marco. Thermoelectric phenomena in superconducting nanostructures. Materials Science [cond-mat.mtrl-sci]. Université Grenoble Alpes, 2015. English. NNT : 2015GREAY099 . tel-01686644

**HAL Id: tel-01686644**

**<https://theses.hal.science/tel-01686644>**

Submitted on 17 Jan 2018

**HAL** is a multi-disciplinary open access archive for the deposit and dissemination of scientific research documents, whether they are published or not. The documents may come from teaching and research institutions in France or abroad, or from public or private research centers.

L'archive ouverte pluridisciplinaire **HAL**, est destinée au dépôt et à la diffusion de documents scientifiques de niveau recherche, publiés ou non, émanant des établissements d'enseignement et de recherche français ou étrangers, des laboratoires publics ou privés.

## **THÈSE**

Pour obtenir le grade de

### **DOCTEUR DE LA COMMUNAUTÉ UNIVERSITÉ GRENOBLE ALPES**

Spécialité : Physique de la Matière Condensée et du Rayonnement

Arrêté ministériel : 25 mai 2016

Présentée par

**Angelo DI MARCO**

Thèse dirigée par **Frank W.J. HEKKING**

préparée au sein du **Laboratoire de Physique et de Modélisation  
des Milieux Condensés**  
dans l'**École Doctorale Physique**

### **Phénomènes thermo-électriques dans des nanostructures supraconductrices**

### **Thermoelectric phenomena in superconducting nanostructures**

Thèse soutenue publiquement le **2 mars 2015**,  
devant le jury composé de :

**Monsieur FRANK HEKKING**

PROFESSEUR, UNIVERSITE GRENOBLE 1, Directeur de thèse

**Monsieur ROSARIO FAZIO**

PROFESSEUR, ECOLE NORMALE SUPERIEURE PISE - ITALIE,  
Rapporteur

**Madame INES SAFI**

CHARGE DE RECHERCHE, CNRS DELEGATION ILE-DE-FRANCE SUD,  
Rapporteur

**Madame WIEBKE GUICHARD**

PROFESSEUR, UNIVERSITE GRENOBLE 1, Président

**Monsieur JUKKA P. PEKOLA**

PROFESSEUR, UNIVERSITE AALTO - FINLANDE, Examineur



## **THÈSE**

Pour obtenir le grade de

### **DOCTEUR DE LA COMMUNAUTÉ UNIVERSITÉ GRENOBLE ALPES**

Spécialité : Physique de la Matière Condensée et du Rayonnement

Arrêté ministériel : 25 mai 2016

Présentée par

**Angelo DI MARCO**

Thèse dirigée par **Frank HEKKING**

préparée au sein du **Laboratoire de Physique et de  
Modélisation des Milieux Condensés**  
dans l'**École Doctorale Physique**

### **Phénomènes thermo-électriques dans des nanostructures supraconductrices**

### **Thermoelectric phenomena in superconducting nanostructures**

Thèse soutenue publiquement le **2 mars 2015**,  
devant le jury composé de :

**Monsieur FRANK HEKKING**

PROFESSEUR, UNIVERSITE GRENOBLE 1, Directeur de thèse

**Monsieur ROSARIO FAZIO**

PROFESSEUR, ECOLE NORMALE SUPERIEURE PISE - ITALIE,  
Rapporteur

**Madame INES SAFI**

CHARGE DE RECHERCHE, CNRS DELEGATION ILE-DE-FRANCE  
SUD, Rapporteur

**Madame WIEBKE GUICHARD**

PROFESSEUR, UNIVERSITE GRENOBLE 1, Président

**Monsieur JUKKA P. PEKOLA**

PROFESSEUR, UNIVERSITE AALTO - FINLANDE, Examineur





*To My Family*



Cui dono lepidum novum libellum  
arida modo pumice expolitum?  
Corneli, tibi: namque tu solebas  
meas esse aliquid putare nugas,  
iam tum, cum ausus es unus Italorum  
omne aevum tribus explicare cartis,  
doctis, Iuppiter, et laboriosis.  
Quare habe tibi quidquid hoc libelli  
qualecumque; quod, o patrona Virgo,  
plus uno maneat perenne saeclo.

**Gaius Valerius Catullus**, *Liber*, Carmen I

Jieru chi lavuravu mminzu maru  
e mi vinna la nova ca jiera natu patrima.  
Allura mi misu aa rata pi shcuppetta,  
la vommira pi bbaiunetta,  
e tira camina camina camina  
ngundraiu lu niru ri na pulicissa.  
Cci nn'erini tria. Jivu ji e ci misu fucu.  
Guna si vrushajia, n'ata si ni scappajia  
e l'ata nun pusu viri chi vvvia pigghjiaia.  
Pi la pressa mi cci scurdajiu la cchetta.  
La cchetta si vrushajia e lu manicu cci ristajia.

**Anonymous**, Canzun'aa l'immersa  
(Dialect of Papisidero – Calabria – Italy)



# **Electric and Thermal Phenomena in Superconducting Nanostructures**



# Contents

<b>Résumé de la Thèse</b>	<b>xiii</b>
<b>List of publications and author's contribution</b>	<b>xv</b>
<b>Introduction</b>	<b>xvii</b>
<b>1 Leakage Current of a Superconductor-Normal Metal Tunnel Junction Connected to a High-Temperature Environment</b>	<b>1</b>
Introduction . . . . .	1
1.1 NIS junction coupled to a high-temperature environment . . . . .	4
1.1.1 Single-particle current . . . . .	4
1.1.2 Weak and strong coupling regimes . . . . .	7
1.1.3 Subgap leakage current: weak coupling . . . . .	9
1.1.4 Subgap leakage current: strong coupling . . . . .	12
1.2 NIS junction coupled to a high-temperature environment by means of a transmission line . . . . .	12
1.2.1 Voltage fluctuations in the presence of a transmission line	13
1.2.2 Correlation function for the transmission line circuit . . .	15
1.2.3 The transmission function . . . . .	16
1.2.4 Subgap leakage current: weak coupling . . . . .	18
1.3 Multi-particle tunneling . . . . .	21
1.4 Conclusions . . . . .	22
<b>2 Effect of Photon-Assisted Andreev Reflection in the Accuracy of a SINIS Turnstile</b>	<b>23</b>
Introduction . . . . .	23
2.1 Electronic transport in a SINIS turnstile . . . . .	24
2.1.1 Single-electron tunneling . . . . .	25
2.1.2 Andreev reflection and higher-order processes . . . . .	27
2.2 Environment-assisted Andreev reflection . . . . .	28
2.2.1 The effect of the electromagnetic environment on the electronic transport . . . . .	28

2.2.2	Single-photon-assisted two-electron tunneling rate . . . . .	28
2.2.3	Results . . . . .	33
2.3	Conclusions . . . . .	37
<b>3</b>	<b>Design of an Efficient Superconducting Junctions-Based Cascade Electron Refrigerator</b>	<b>39</b>
	Introduction . . . . .	39
3.1	Superconducting electron refrigerators . . . . .	41
3.1.1	(SI)NIS cooler . . . . .	42
3.1.2	(SI)SIS cooler . . . . .	45
3.2	Superconducting cascade electron refrigerator . . . . .	48
3.2.1	System and thermal equilibrium equations . . . . .	48
3.2.2	The role of the tunnel resistance ratio . . . . .	50
3.2.3	Different materials and volume ratios . . . . .	52
3.2.4	Quasiparticle thermalization . . . . .	52
3.3	Conclusions . . . . .	53
<b>4</b>	<b>Quantum Phase-Slip Junction Under Microwave Irradiation</b>	<b>55</b>
	Introduction . . . . .	55
4.1	Qualitative discussion of the main results . . . . .	57
4.2	Current-biased QPSJ . . . . .	62
4.2.1	QPSJ Hamiltonian . . . . .	62
4.2.2	Current-voltage characteristic . . . . .	63
4.3	Dual Shapiro's steps: non-perturbative formal approach . . . . .	67
4.4	Lowest order results . . . . .	69
4.4.1	DC-current-biased QPSJ . . . . .	69
4.4.2	Microwave irradiated QPSJ . . . . .	72
4.4.3	Accuracy of the current Shapiro steps . . . . .	73
4.4.4	The effect of Joule heating . . . . .	75
4.5	Conclusions . . . . .	77
<b>5</b>	<b>Conclusions</b>	<b>79</b>
	<b>Appendices</b>	<b>83</b>
<b>A</b>	<b>Electron Tunneling in a SINIS Turnstile</b>	<b>83</b>
	Introduction . . . . .	83
A.1	Energy of a single-island circuit . . . . .	83
A.2	The single-electron transistor (SET) . . . . .	85
A.2.1	Energy cost . . . . .	85
A.2.2	Single-electron tunneling . . . . .	86

---

A.2.3	Two-electron tunneling . . . . .	89
<b>B</b>	<b>Caldeira-Legget Model and Fluctuation-Dissipation Theorem</b>	<b>93</b>
<b>C</b>	<b>Current and Heat Peak in a <math>S_1IS_2</math> Josephson Junction</b>	<b>95</b>
	Introduction . . . . .	95
C.1	Current peak . . . . .	95
C.1.1	Positive energies . . . . .	96
C.1.2	Negative energies . . . . .	97
C.1.3	Total charge current . . . . .	99
C.2	Heat peak . . . . .	100
<b>D</b>	<b>QPSJ Hamiltonian for an Underdamped Josephson Junction</b>	<b>103</b>
	Introduction . . . . .	103
D.1	Current-biased representation . . . . .	103
D.1.1	The QPSJ Hamiltonian . . . . .	103
D.1.2	The quasi-charge equation of motion . . . . .	105
D.2	Voltage-biased representation . . . . .	107
D.2.1	The QPSJ Hamiltonian . . . . .	107
D.2.2	The quasi-charge equation of motion . . . . .	108
<b>E</b>	<b>Voltage Across a Microwave Irradiated Quantum Phase-Slip Junction</b>	<b>111</b>
	Introduction . . . . .	111
E.1	Perturbative expansion at all orders in $U_0$ : Keldysh formalism . . . . .	111
E.1.1	The mean value $F_q$ . . . . .	114
E.1.2	The mean value $F_{\text{env}}$ . . . . .	115
E.1.3	Final formula . . . . .	119
E.2	First-order term . . . . .	121
	<b>Bibliography</b>	<b>125</b>



# Résumé de la Thèse

Ma thèse de doctorat traite de l'étude théorique des phénomènes électriques et thermiques qui se produisent dans des nanostructures supraconductrices qui sont l'objet de plusieurs lignes de recherche de la physique de la matière condensée. Nous nous focalisons sur quatre dispositifs basés sur les supraconducteurs et de minces barrières isolantes où le transport de la charge et de la chaleur est gouverné par l'effet tunnel quantique.

Nous commençons par analyser une jonction métal Normal-Isolant-Supraconducteur (N-I-S). En principe, aucun courant à une particule ne peut s'écouler dans ce circuit quand le voltage de polarisation est en dessous du gap d'énergie de S. Pourtant, un courant de fuite en dessous du gap est observé dans la courbe caractéristique courant-voltage (I-V) expérimental de ce dispositif, même à très basses températures. Nous montrons que l'absorption de photons de l'environnement électromagnétique à haute température connecté à la jonction est une origine possible du processus de tunnel à un électron en dessous du gap. Nous considérons une jonction N-I-S connectée à l'environnement soit directement soit indirectement au moyen d'une ligne de transmission résistif à basse température. Nous analysons analytiquement et numériquement le courant en dessous du gap dans ces deux circuits.

Ensuite nous considérons un transistor hybride à un électron (SET) constitué d'une île de métal normal N contrôlée avec une tension de grille et connectée, au moyen de deux jonctions à effet tunnel, à deux fils supraconducteurs S polarisés en tension (S-I-N-I-S). Lorsque l'on fait varier le voltage de N correctement dans le temps, un courant contrôlable à un électron s'écoule entre les deux supraconducteurs. En principe, la réflexion d'Andreev, c'est-à-dire l'effet tunnel à deux électrons de N à S, peut être interdite. Expérimentalement, ce processus à deux particules contribue aussi au courant total à travers le SET. Nous montrons que l'échange de photons entre ce dispositif et l'environnement électromagnétique où il est disposé rend la réflexion d'Andreev énergétiquement possible. De plus, nous discutons comment cet effet limite la précision du processus de tunnel à un électron nécessaire pour les applications métrologiques.

Ensuite nous nous focalisons sur les caractéristiques thermodynamiques des jonctions supraconductrices à effet tunnel. Nous discutons d'abord des capacités de refroidissement électronique des dispositifs à double jonction S1-I-N-I-S1 et S2-I-S1-I-S2, où les supraconducteurs S2 et S1 ont un gap d'énergie différent. Après nous étudions le design et le fonctionnement d'un nanoréfrigérateur électro-

nique à cascade basé sur une combinaison de ces deux structures. Nous montrons numériquement que une île de métal normal peut être réfrigérée au dessous de 100 mK à partir d'une température de 500 mK. Nous discutons ensuite de la réalisation pratique et des limitations d'un tel dispositif.

Enfin, nous considérons la dynamique d'une jonction à sauts de phase quantique (QPSJ) connectée à une source de micro-ondes. En ce qui concerne une jonction Josephson ordinaire, une QPSJ peut montrer des marches de Shapiro duels, c'est-à-dire des plateaux de courant bien définis situés à des multiples entiers de la fréquence des micro-ondes dans la courbe caractéristique I-V. Aucune observation expérimentale n'a abouti jusqu'à maintenant. Les fluctuations thermiques et quantiques peuvent nettement étaler la courbe I-V. Pour comprendre ces effets, nous déterminons la caractéristique I-V d'une QPSJ polarisée en courant, irradiée avec des micro-ondes et connectée à un environnement résistif et inductif. Nous montrons que l'effet de ces fluctuations est gouverné par la résistance de l'environnement et par le rapport entre l'énergie de phase-slip et l'énergie inductive. Nos résultats sont importants pour les expériences qui visent à l'observation des marches de Shapiro duels dans les QPSJ pour la définition du courant quantique standard.

# List of publications and author's contribution

The papers published, submitted and in preparation arising from the scientific results illustrated in this thesis are the following:

1. A. Di Marco, V. F. Maisi, J. P. Pekola, and F. W. J. Hekking, “Leakage current in a superconductor-normal metal tunnel junction connected to a high-temperature environment”, *Physical Review B*, vol. **88**, p. 174507 (November 2013).
  - The author did the major part of the calculations, prepared all the figures, and wrote most of the manuscript.
2. M. Camarasa-Gomez, A. Di Marco, F. W. J. Hekking, C. B. Winkelmann, H. Courtois, and F. Giazotto, “Superconducting cascade electron refrigerator”, *Applied Physics Letters*, vol. **104**, p. 192601 (May 2014).
  - The author did the analytical estimations, performed the major part of the numerical simulations, prepared all the figures, and contributed in the preparation of the manuscript.
3. A. Di Marco, F. W. J. Hekking, and G. Rastelli, “Quantum phase-slip junction under microwave irradiation”, arXiv:1502.04878, submitted to *Physical Review B* (February 2015).
  - The author revised and contributed to the calculations, performed the numerical analysis, prepared all the figures, and wrote most of the manuscript.
4. A. Di Marco, V. F. Maisi, J. P. Pekola, and F. W. J. Hekking, “Effect of photon-assisted Andreev reflection in the accuracy of a SINIS turnstile”, manuscript in preparation, to be submitted to *Physical Review B*.
  - The author did the major part of the calculations, performed the numerical analysis, prepared all the figures, and wrote the manuscript.



# Introduction

## General Scientific Context

Miniaturization of solid state electronic components has known a fast growth during the last 25 years. The constant improvement of the lithographic techniques allows the fabrication of devices at the nanometric scale with a wide range of possible applications. Nowadays, such nanostructures are the building blocks of most of the electronic equipment commonly used in science, in the industry as well as in the daily life. For instance, the central processing unit (CPU) of a modern computer is an integrated circuit containing billions of nanosized transistors, distributed over a surface of a hundred of squared millimeters.

The development of nanoelectronics proceeded in parallel with the enhancement of the efficiency of the refrigeration techniques. The possibility to routinely achieve cryogenic temperatures, even well below a Kelvin, allowed to decrease significantly the thermal noise in the electrical circuits and to create new nanoscale devices, such as very accurate nano-sensors and Carnot-type nanomachines, thereby widening the range of applicability of nanoelectronics.

In this context, the progressive reduction of the size of the solid state electronic components together with the use of very low temperatures gave rise to a wealth of phenomena related to the quantum mechanical nature of the electrons in the nanoscale systems. To design the cryogenic electronic nanostructures and to understand and improve their functioning one has to face up to new fundamental quantum effects, typically related to the nanometric size and to the particle-particle interactions. The quantized conductance observed in quantum point contacts and the weak localization in disordered nanostructures are two examples of quantum phenomena caused by the nanoscale size of the devices. These two quantum mechanical effects show up when the wave-length and the phase-coherence length, respectively, of the electrons are comparable with the size of the involved conductors. On the other hand, interaction effects give rise, for instance, to the Coulomb blockade phenomenon, which is related to the discreteness of the electric charge.

More recently, it has been realized that the energy transfer and relaxation processes in nanostructured electronic devices are not only determined by phonons. Rather, the black body radiation produced by the external electromagnetic environment, where the nanostructures are embedded, can play an important role,

especially at subkelvin temperatures. Understanding and controlling this kind of interaction is crucial for the thermoelectric applications of the nanoscale circuits. The exchange of energy by means of photons between the main system and the environment can be detrimental, limiting the performances of the nanostructured devices. On the other hand, a properly engineered environment can be fundamental in the implementation of a certain particular function arising from the interplay between the electronic nanostructure and the environment itself.

The use of superconducting metals in the fabrication of nanoelectronic devices has opened the road for new technological possibilities. The peculiarity of this kind of materials is that they show quantum properties also at the macroscopic scale. The dissipationless current of Cooper pairs and the presence of the energy gap in the density of states of a superconductor are fundamental for the realization of a huge number of applications. New quantum mechanical features can be accessed and are expected when their size is decreased till the nanoscale, e.g., the observation of both phase-slip tunneling events and energy filtering effects. Particularly interesting is the combination of nanostructured superconductors with normal metals which allows to build devices aimed to have accurate charge (metrology) and heat (nanorefrigeration) transfer.

## Summary

The aim of this Ph.D. thesis is to study, from a theoretical point of view, the electric and thermal phenomena occurring in some superconducting nanostructures which are the object of various research lines in condensed matter physics. Specifically, we focus on four different devices based on superconductors and insulating tunnel barriers where both charge and heat transport are governed by the quantum tunneling effect.

In the *first chapter*, we start by considering a voltage-biased Normal metal-Insulator-Superconductor (NIS) tunnel junction. No single-particle current is expected to flow in this circuit when the applied voltage  $V$  is below the superconducting energy gap  $\Delta$  of S,  $|eV| < \Delta$ . However, in real experiments, a subgap leakage current is observed in the current-voltage characteristic of the NIS junction, even at very low temperatures. Such a current limits the applications of this superconducting device based on the existence of the energy gap. We show that the absorption of photons from the high-temperature external electromagnetic environment connected to the junction is a possible origin of the single-particle tunneling below the gap. Specifically, we first consider a NIS junction directly coupled to the environment and then we focus on a circuit where a low-temperature lossy transmission line is inserted between them. For both these circuits, we analyze analytically and numerically the subgap leakage current by means of the so-called

---

$P(E)$  theory developed by G.-L. Ingold and Yu. V. Nazarov [1]. In particular, we find that such an environment-assisted current is exponentially suppressed as the length and the resistance per unit length of the line are increased. These results have been obtained in close collaboration with Prof. J. P. Pekola and Dr. V. F. Maisi from the “Low Temperature Laboratory” of the Aalto University (Finland) and published in Physical Review B, vol. 88, p. 174507 (2013).

In the *second chapter*, we go beyond the single NIS junction considering a hybrid single-electron transistor (SET) constituted by a gate-controlled normal-metal island (N) connected to two voltage-biased superconducting leads (S) by means of two tunnel junctions (SINIS). In the Coulomb blockade regime, this device is expected to work as a perfect charge pump: a controlled single-electron current flows between the two superconductors by properly changing in time the gate potential of N. In principle, the Andreev reflection, i.e., the tunneling of two electrons from N to S can be ideally suppressed when the charging energy  $E_C$  of N is larger than the energy gap  $\Delta$  of S. Actually, in real experiments, this two-particle tunneling process also contributes to the total current through the SET, even though the condition  $E_C > \Delta$  holds. We show that the exchange of photons between the SINIS device and the high-temperature electromagnetic environment where it is embedded makes the Andreev reflection energetically possible. We discuss how this effect limits the single-electron tunneling accuracy needed for metrological applications. Also the achievement of these results has been possible thanks to the fruitful collaboration with Prof. J. P. Pekola and Dr. V. F. Maisi. A paper about this project is in preparation and will be soon submitted to a peer reviewed international journal, such as Physical Review B.

In the *third chapter*, we focus on the thermodynamical features of the superconductor-based tunnel junctions. We start by describing the electronic cooling capabilities of the  $S_1INIS_1$  and  $S_2IS_1IS_2$  double-junction devices, where  $S_2$  and  $S_1$  are different superconductors with energy gaps  $\Delta_2 > \Delta_1$ . We then study the design and operation of an electronic nanorefrigerator based on a combination of these two structures, namely the  $S_2IS_1INIS_1IS_2$  device. Thanks to the cascade extraction of hot-quasiparticles, we show numerically that the normal-metal central electrode N can be cooled down to about 100 mK starting from a bath temperature of 500 mK. We discuss the practical implementation, potential performance and limitations of such a device, proving that it is more efficient than a  $S_1INIS_1$  cooler. This project has been carried on in collaboration with Dr. F. Giazotto and M. Camarasa-Gomez from the “NEST Laboratory” of “Scuola Normale Superiore” of Pisa (Italy), and with Prof. H. Courtois and Dr. C. B. Winkelmann from “Institut Néel” of Grenoble. Our findings have been published in Applied Physics Letters, vol. 104, p. 192601 (2014).

In the *forth chapter*, we consider the dynamics of a quantum phase-slip junction (QPSJ) – a dual Josephson junction – connected to a microwave source with

frequency  $\omega_{\text{mw}}$ . With respect to an ordinary Josephson junction, a QPSJ can sustain dual Shapiro steps, consisting of well-defined current plateaus at multiple integers of  $e\omega_{\text{mw}}/\pi$  in the current-voltage (I-V) characteristic. The experimental observation of these plateaus has been elusive up to now. We argue that thermal as well as quantum fluctuations can smear the I-V characteristic considerably. In order to understand these effects, we derive, by means of the Keldysh formalism, the I-V curve of a current-biased QPSJ under microwave irradiation and connected to an inductive and resistive environment. We find that the effect of these fluctuations is governed by the resistance of the environment and by the ratio of the phase-slip energy and the inductive energy. Our results are of interest for experiments aiming at the observation of dual Shapiro steps in QPSJ devices for the definition of the quantum current standard. In this project, the supervision of Dr. G. Rastelli from the “Quantum Transport Group” of the University of Konstanz (Germany) has been essential. The obtained results are presented in a paper available in arXiv.org (1502.04878). We have also submitted the manuscript to Physical Review B.

In the *fifth chapter*, we finally list our main findings and in the *appendices* at the end of the manuscript provide the details of some derivations/calculations discussed in the first four chapters. The latter and the corresponding appendices are independent. Consequently, the physical meaning of the used symbols may change.

# Leakage Current of a Superconductor-Normal Metal Tunnel Junction Connected to a High-Temperature Environment

## Introduction

The peculiar nature of single-particle electronic transport through a normal metal-insulator-superconductor (NIS) junction is at the origin of several interesting applications [see Fig. 1.1(a)]. Such junctions are widely used in experiments of mesoscopic physics as a spectroscopic tool [2,3], as a very sensitive thermometer [4–6] and as a key element in nano-refrigeration [4, 7, 8]. Furthermore, NIS junctions are currently investigated in view of achieving a high accuracy when controlling the current through a single-electron SINIS turnstile. Such a device is one of the interesting candidates for the completion of the so-called quantum metrological triangle, *i.e.*, it can be used to obtain a precise realization of current [9, 10]. These applications are all based on the existence of the Bardeen-Cooper-Schrieffer (BCS) energy gap  $\Delta$  in the density of states (DoS) of the superconductor [11]. Ideally one would expect no single-electron current to flow through a NIS junction at low temperature as long as the bias voltage  $V$  satisfies the inequality  $-\Delta < eV < \Delta$ , see Fig. 1.1(b).

In practice, the subgap current is different from zero. This is a central problem which limits the performance of applications based on energy-selective single-particle transport in NIS junctions. The presence of unwanted accessible states in the subgap region manifests itself as a smearing of the junction's current-voltage ( $I$ - $V$ ) characteristic as well as of its differential conductance. Giaever was the first to experimentally study the NIS junction. He noticed that this deviation from the ideal behavior was present even if the junction was kept at a temperature much

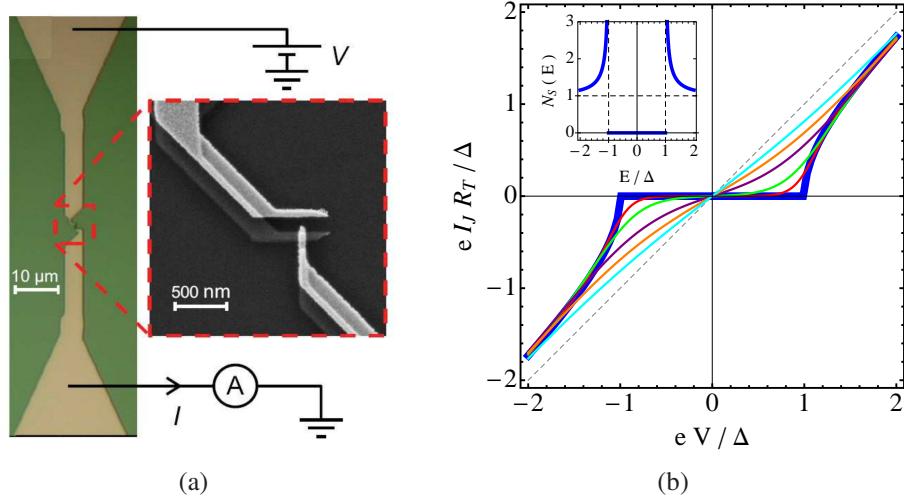


Figure 1.1: (a) Optical microscope picture (left; colored) and scanning electron micrograph (right; black and white) of a NIS junction made of aluminum (low contrast) and copper (high contrast), the superconductor and the normal metal respectively [16]. (b) Plot of the current-voltage characteristic of an ideal NIS junction for different values of its temperature,  $k_B T_{\text{jun}}/\Delta$ : 0 (blue thick line), 0.1 (red), 0.2 (green), 0.4 (purple), 0.6 (orange), 0.9 (cyan). The black dashed line is  $V = R_T I_J$ . The inset shows the zero-temperature BCS density of states  $N_S(E)$  as a function of the rescaled energy  $E/\Delta$ .

lower than the critical one  $T_c$  of the superconductor [12]. A possible source of subgap leakage currents is the occurrence of many-electron tunneling processes, such as Andreev reflection [13–15]. However, these many-electron processes are strongly suppressed if the tunnel resistance  $R_T$  of the junction is chosen high enough and do not account for the observed residual subgap transport either.

Dynes modified the BCS superconducting DoS introducing a single phenomenological dimensionless parameter,  $\gamma_{\text{Dynes}}$ , in order to fit the behavior of the subgap quasi-particle tunneling current through a Josephson junction [17]. The modified DoS, normalized to the corresponding normal-state DoS at the Fermi energy, is given by

$$N_S^{\text{Dynes}}(E) = \left| \Re \left[ \frac{E/\Delta + i\gamma_{\text{Dynes}}}{\sqrt{(E/\Delta + i\gamma_{\text{Dynes}})^2 - 1}} \right] \right|. \quad (1.1)$$

It can be seen that  $\gamma_{\text{Dynes}}$  indeed accounts for the broadening of the DoS around  $\Delta$  and the occurrence of states within the gap, see Fig 1.2. This expression is frequently used in both numerical and analytical calculations [18], but concerning the microscopic origin of the Dynes parameter  $\gamma_{\text{Dynes}}$ , for temperatures far below

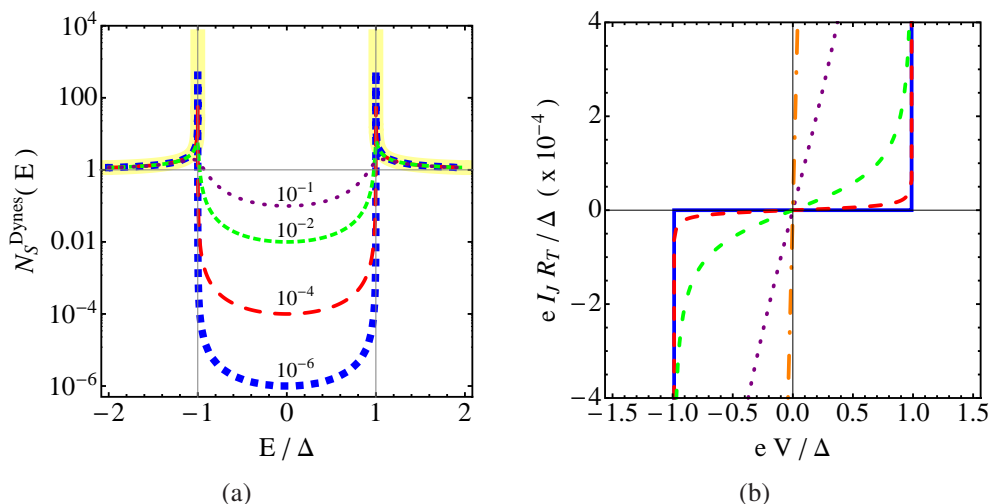


Figure 1.2: (a) Plot in logarithmic scale of the Dynes DoS Eq. (1.1) as a function of the rescaled energy  $E/\Delta$  for different values of  $\gamma_{\text{Dynes}}$ :  $10^{-6}$  (blue),  $10^{-4}$  (red),  $10^{-2}$  (green),  $10^{-1}$  (purple). Notice that  $N_S^{\text{Dynes}}(0) \simeq \gamma_{\text{Dynes}}$  and  $N_S^{\text{Dynes}}(\pm\Delta) \approx 1/2\sqrt{\gamma_{\text{Dynes}}}$ . Also shown is the ideal BCS DoS,  $N_S(E)$ , (yellow thick line). (b) Close view of the subgap region of the zero-temperature  $I$ - $V$  characteristic for different Dynes parameters. From the flatter to the steeper curve,  $\gamma_{\text{Dynes}}$  is equal to 0 (blue),  $10^{-5}$  (red),  $10^{-4}$  (green),  $10^{-3}$  (purple),  $10^{-2}$  (orange).

$T_c$ , relatively little is known. In general, the smearing of the DoS can be energy-dependent.

Recently it was realized that the exchange of energy between the NIS junction and its surrounding electromagnetic environment may be one of the causes of the smearing of the BCS DoS [16, 19]. Indeed, under certain conditions, energy absorption from such an environment enables the crossing of the tunnel barrier by single electrons even for  $|V|$  much less than  $\Delta/e$ . Within this framework an analytical expression for  $\gamma_{\text{Dynes}}$  has been obtained in terms of the parameters characterizing the NIS junction's environment [16]. In this particular case, the Dynes parameter found describes the smearing at all energies.

Following the idea of photon-assisted tunneling demonstrated in Ref. [16], we generalize the approach here for an external circuit characterized by an arbitrary impedance  $Z(\omega)$ , kept at a temperature  $T_{\text{env}}$  that is not necessarily the temperature  $T_{\text{jun}}$  of the NIS junction, see Fig. 1.3(a). We obtain expressions for the subgap leakage current and the subgap Dynes parameter  $\gamma_{\text{Dynes}}^{\text{sub}}$ , valid for energies smaller than the gap  $\Delta$ . Then we turn our attention to the circuit depicted in Fig. 1.3(b), where we study the effects of the insertion of a lossy transmission line, meant to act as a frequency-dependent filter, between the cold junction and

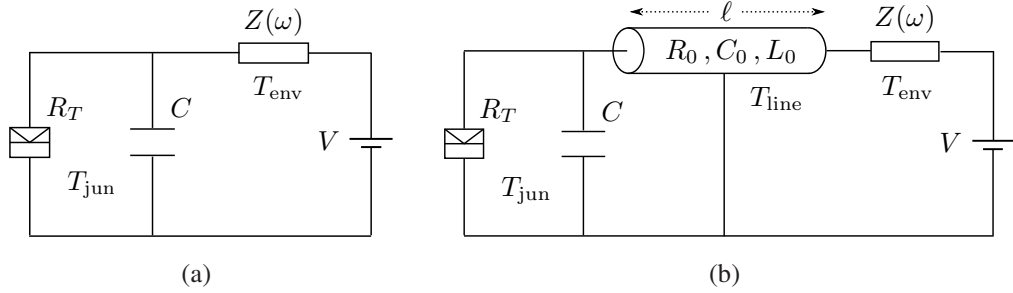


Figure 1.3: Circuit representation of the two studied configurations. (a) A NIS junction at temperature  $T_{\text{jun}}$  is connected in parallel to its capacitance  $C$  and to an impedance  $Z(\omega)$  which represents the high-temperature environment at temperature  $T_{\text{env}} \gg T_{\text{jun}}$ . The whole circuit is biased by the constant voltage  $V$ . (b) A transmission line of length  $\ell$  is inserted between the junction and the impedance  $Z(\omega)$  of circuit (a). It is described by the parameters  $R_0, C_0, L_0$ , the resistance, the capacitance and the inductance per unit length, respectively, as well as by its temperature  $T_{\text{line}}$  which is assumed equal to  $T_{\text{jun}}$ .

the high-temperature external impedance  $Z(\omega)$ . In particular we use our results to understand under which conditions the transmission line will behave as a filter capable of reducing the photon-assisted tunneling induced by the high-temperature external impedance and thus reducing  $\gamma_{\text{Dynes}}^{\text{sub}}$  to values that are compatible with the accuracy requirements for applications such as the SINIS turnstile.

## 1.1 NIS junction coupled to a high-temperature environment

### 1.1.1 Single-particle current

We start by considering the basic circuit illustrated in Fig. 1.3(a) where a NIS junction is connected in series to an effective high-temperature impedance  $Z(\omega)$ . The junction itself is characterized by a tunnel resistance  $R_T$  in parallel with a capacitance  $C$ . The entire circuit is voltage biased. This constitutes a minimal model for a junction embedded in an external electromagnetic environment at temperature  $T_{\text{env}}$ , which can be much higher than the temperature  $T_{\text{jun}}$  of the junction.

According to the so-called  $P(E)$  theory [1], the single-particle tunneling cur-

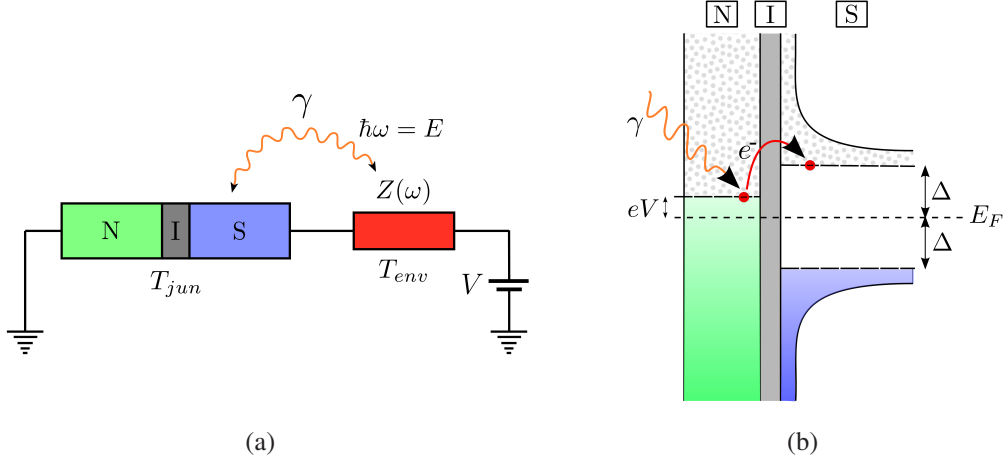


Figure 1.4: NIS junction connected to an external electromagnetic environment. (a) The exchange of the energy  $E = \hbar\omega$  between the junction and the effective impedance  $Z(\omega)$  occurs by means of a certain number of photons. (b) The absorption of just one photon with frequency  $(\Delta - eV)/\hbar$  allows one electron to overcome the insulating barrier even if the bias voltage  $eV$  is below the energy gap  $\Delta$ .

rent through a NIS junction coupled to an external environment is given by

$$I_{\text{NS}}(V) = \frac{1}{eR_T} \int dE \int dE' N_S(E') [1 - f(E')] \times \left\{ f(E - eV) - f(E + eV) \right\} P(E - E'). \quad (1.2)$$

Here, the energy  $E$  refers to the electrons of the normal metal,  $E'$  is the energy of the superconductor quasi-particles,  $N_S(E')$  is the BCS density of states of the superconducting wire divided by the normal-metal DoS at the Fermi level and  $f(E) = [e^{\beta_{\text{jun}} E} + 1]^{-1}$  is the Fermi-Dirac distribution with  $\beta_{\text{jun}} = 1/k_B T_{\text{jun}}$  the inverse temperature of the junction. Expression (1.2) does not take into account the higher order processes in tunneling which will be ignored throughout this chapter. The validity of this assumption will be discussed in Sec.1.3.

The function  $P(E)$  in Eq. (1.2) is the probability density that the tunneling electron exchanges an amount of energy  $E$  with the environment. This process takes place through the emission or absorption of photons [see Fig 1.4]. It is defined as

$$P(E) = \frac{1}{2\pi\hbar} \int_{-\infty}^{+\infty} dt e^{iEt/\hbar} e^{J(t)}, \quad (1.3)$$

*i.e.*, it is the Fourier transform of the exponential of the correlation function

$$J(t) = 2 \int_0^{+\infty} \frac{d\omega}{\omega} \frac{\Re[Z_{\text{tot}}(\omega)]}{R_K} \times \left\{ \coth\left(\frac{1}{2}\beta_{\text{env}}\hbar\omega\right) [\cos(\omega t) - 1] - i \sin(\omega t) \right\}. \quad (1.4)$$

Here  $Z_{\text{tot}}(\omega)$  is the total impedance seen by the junction, resulting from the connection in parallel of  $C$  and  $Z(\omega)$ ,  $R_K = h/e^2$  is the quantum resistance and  $\beta_{\text{env}} = 1/k_B T_{\text{env}}$ .

The function  $J(t)$  determines the strength of the coupling between the NIS junction and the environment. Indeed if  $J(t) = 0$ , the probability density  $P(E)$  is equal to a Dirac delta  $\delta(E)$  and the single-particle tunneling current is elastic. Expression (1.2) then reduces to the standard expression for single-particle tunneling in NIS junctions valid in the absence of environment. The environment-induced inelastic tunneling processes occur only when  $J(t) \neq 0$ . In general, the time intervals where the inelastic effects are important are related to the energy ranges where  $P(E) \neq 0$ . The order of magnitude of  $J(t)$  sets the number of photons responsible for the single-particle tunneling. Depending on this number, the coupling between the NIS junction and the multi-mode environment can be considered weak or strong. We will treat both regimes of weak and strong coupling in more detail.

In order to analyze the smearing of the NIS junction's  $I$ - $V$  characteristic due to the presence of the high-temperature environment, we will ignore the thermal smearing induced by finite temperature of the N and S electrodes. This is an adequate approximation under standard experimental conditions where  $T_{\text{jun}} \ll \Delta/k_B$ . Hereafter we will set the temperature of the junction  $T_{\text{jun}}$  to zero. Under this assumption the single-particle current (1.2) becomes

$$I_{\text{NS}}(V) \simeq \frac{1}{eR_T} \int_{-eV}^{+eV} dE \int_{\Delta}^{+\infty} dE' N_S(E') P(E - E'). \quad (1.5)$$

We furthermore will focus on the subgap region of the  $I$ - $V$  curve considering  $|eV| \ll \Delta$ . As a result, the integration variables  $|E| \ll E'$  in (1.5), and we can approximate  $P(E - E') \approx P(-E')$ . The resulting integral over  $E$  can be performed immediately to yield

$$I_{\text{NS}}^{\text{sub}}(V) \simeq \gamma_{\text{env}} \frac{V}{R_T}, \quad (1.6)$$

where the factor  $\gamma_{\text{env}}$  is given by the integral

$$\gamma_{\text{env}} = 2 \int_{\Delta}^{+\infty} dE' N_S(E') P(-E'). \quad (1.7)$$

We see that for the parameter  $\gamma_{\text{env}}$ , Eq. (1.7), and hence the subgap current given by Eq. (1.6) to be nonzero, the function  $P(E)$  should be nonzero for energies  $E \leq -\Delta$ . This reflects the fact that under subgap conditions  $eV, k_B T_{\text{jun}} \ll \Delta$ , a nonzero single-particle current occurs only if the tunneling electrons absorb an energy  $\gtrsim \Delta$  from the environment. For instance,  $\gamma_{\text{env}} = 0$  for elastic tunneling in the absence of an environment, when  $P(E) = \delta(E)$ . We also expect  $\gamma_{\text{env}}$  to vanish when the temperature of the environment  $k_B T_{\text{env}}$  is much less than the energy gap  $\Delta$ . Indeed, due to detailed balance [1],  $P(-E) = e^{-E/k_B T_{\text{env}}} P(E)$ , the function  $P(E)$  is strongly suppressed for negative energies  $E < -k_B T_{\text{env}}$ . This means that the integral in (1.7) will vanish unless the environment is sufficiently hot,  $k_B T_{\text{env}} \gtrsim \Delta$ .

In order to make a connection with the aforementioned approach due to Dynes, we linearize the usual expression for elastic single-particle tunneling in a NIS junction, using the Dynes DoS (1.1) to characterize the superconducting electrode:

$$I_{\text{NS}}^{\text{D}}(V) = \frac{1}{eR_T} \int_{-\infty}^{+\infty} dE' N_S^{\text{Dynes}}(E') [1 - f(E')] \left\{ f(E' - eV) - f(E' + eV) \right\}.$$

By means of this expression, one obtains the linear subgap current-voltage relationship

$$I_{\text{NS}}^{\text{sub}}(V) = \sqrt{\frac{\gamma_{\text{Dynes}}^2}{\gamma_{\text{Dynes}}^2 + 1}} \frac{V}{R_T}.$$

Comparing this result with Eq. (1.6) above, we conclude that, in the linear regime,  $\gamma_{\text{env}}$  can be related to the Dynes parameter in the subgap region,  $\gamma_{\text{Dynes}}^{\text{sub}}$ , according to  $\gamma_{\text{env}} = \sqrt{\gamma_{\text{Dynes}}^{\text{sub}2} / (\gamma_{\text{Dynes}}^{\text{sub}2} + 1)}$ . We see in particular that the two parameters coincide  $\gamma_{\text{Dynes}}^{\text{sub}} = \gamma_{\text{env}}$  whenever  $\gamma_{\text{env}}, \gamma_{\text{Dynes}}^{\text{sub}} \ll 1$ . This shows that fluctuations of a high-temperature electromagnetic environment constitute a possible microscopic source of the phenomenological Dynes parameter, at least under subgap conditions,  $eV, k_B T_{\text{jun}} \ll \Delta$ .

### 1.1.2 Weak and strong coupling regimes

As we have seen above, the strength of the coupling between the NIS junction and the environment is determined by the function  $J(t)$ . Let us assume that this function is small, in a sense to be detailed below. Expanding the exponential function  $\exp[J(t)]$  up to the first order in  $J(t)$ , Eq. (1.3) becomes

$$P(E) \simeq \frac{1}{2\pi\hbar} \int_{-\infty}^{+\infty} dt e^{iEt/\hbar} [1 + J(t)]. \quad (1.8)$$

The evaluation of the integral over time in (1.8) gives<sup>1</sup>

$$\begin{aligned}
P(E) &\simeq \delta(E) + \frac{1}{\hbar} \int_0^{+\infty} \frac{d\omega}{\omega} \frac{\Re[Z_{\text{tot}}(\omega)]}{R_K} \\
&\times \left\{ \left[ \coth\left(\frac{1}{2}\beta_{\text{env}}\hbar\omega\right) - 1 \right] \delta\left(\frac{E}{\hbar} + \omega\right) \right. \\
&+ \left[ \coth\left(\frac{1}{2}\beta_{\text{env}}\hbar\omega\right) + 1 \right] \delta\left(\frac{E}{\hbar} - \omega\right) \\
&\left. - 2\hbar \coth\left(\frac{1}{2}\beta_{\text{env}}\hbar\omega\right) \delta(E) \right\}. \tag{1.9}
\end{aligned}$$

We see that the function  $P(E)$  has an elastic contribution and an inelastic one involving the exchange of exactly one photon between the junction and the environment. In fact the first and the fourth terms represent the elastic tunneling involving zero and one virtual photon, respectively. The second and third terms are related to the process of absorption and emission of one real photon, respectively. We define this one-photon regime as weak coupling. On the other hand, the coupling becomes strong whenever the single-photon exchange between the junction and the environment is no longer the dominant effect. In this case, the higher-order terms cannot be neglected in the series expansion of  $\exp[J(t)]$ , indicating that multi-photon processes have to be taken into account.

We proceed by determining the time interval where the expansion (1.8) holds. Given the fact that  $J(t=0) = 0$ , we expect this to be the short time interval [1]. We set  $Z(\omega) = R$  for simplicity and introduce the dimensionless time  $\tau = t/R_K C$  as well as the ratio  $\rho = R/R_K$ . The quantity  $\exp\{\Re[J(\tau, \rho)]\}$  decays monotonically with increasing time  $\tau$ , starting from unity at  $\tau = 0$ , see Figs. 1.5(a) and 1.5(b). The rate at which it decays depends on  $\rho$ : the larger  $\rho$ , the faster it decays, in agreement with Ref. [1]. We determine the relevant short time interval by determining the characteristic time  $\tau_{10\%}$ , at which the quantity  $\exp\{\Re[J(\tau, \rho)]\}$  dropped by 10%.<sup>2</sup> Figure 1.5(c) shows  $\tau_{10\%}$  as a function of the parameter  $\rho$ , keeping  $T_{\text{env}}$  and  $C$  fixed. The line  $\tau_{10\%}(\rho)$  separates the weak coupling regime found at short times from the strong coupling regimes reached for longer times. As expected [1], with increasing  $\rho$ , the separatrix  $\tau_{10\%}(\rho)$  decreases as  $1/\rho$ , and then saturates at a value  $\tau_S \sim \sqrt{\hbar/k_B T_{\text{env}} R_K C}$  for  $\rho > \rho_{\text{th}} \sim \tau_S$ . As shown in Fig. 1.5(d), the curve  $\tau_{10\%}(\rho)$  shifts up when decreasing the temperature of the

<sup>1</sup>note that the function  $P(E)$  given by Eq. (1.9) is normalized

<sup>2</sup>we consider the real part of  $J(t)$  because (i) it is responsible for the decay of the function  $P(E)$  and (ii) typically  $\Re[J(t)] \gtrsim \Im[J(t)]$  in the time interval  $\tau_e < \tau < \tau_\Delta$  where the photon-assisted tunneling is relevant.

environment,  $T_{\text{env}}$ , thereby increasing the time interval where the expansion (1.8) holds.

We now return to the inelastic tunneling of single electrons through the NIS junction. Under subgap conditions  $k_B T_{\text{jun}}, eV \ll \Delta$ , the energy  $E$  relevant for the photon-assisted tunneling processes is in the interval  $\Delta \lesssim E \lesssim k_B T_{\text{env}}$ . The upper bound corresponds to the largest energy the junction can absorb from the environment. In time domain, we thus have to consider the interval  $\tau_e < \tau < \tau_\Delta$  where  $\tau_\Delta = \hbar/\Delta R_K C$  and  $\tau_e = \hbar/k_B T_{\text{env}} R_K C$ . This interval is represented by the colored strip in Fig. 1.5(c). Note that on the logarithmic scale used here, the lower bound  $\tau_e$  almost coincides with the value  $\tau_S$  at which the separatrix saturates for large values of  $\rho$ . The intersection between  $\tau_\Delta$  and the 10% curve  $\tau_{10\%}(\rho)$  defines the characteristic resistance  $\rho_\Delta$  separating the weak and strong coupling regimes. When  $\rho < \rho_\Delta$ , coupling is weak and only single-photon absorption processes occur (green area); if  $\rho \sim \rho_\Delta$  both single- and multi-photon processes occur during single-electron tunneling (yellow-orange area); as soon as  $\rho \gg \rho_\Delta$ , multi-photon processes become dominant (red area). In particular, the two limiting cases  $\rho \ll \rho_\Delta, \rho_{\text{th}}$  and  $\rho \gg \rho_\Delta, \rho_{\text{th}}$  are equivalent to the conditions  $R/R_K \ll \Delta/k_B T_{\text{env}}$  and  $R/R_K \gg \Delta/k_B T_{\text{env}}$  respectively.

### 1.1.3 Subgap leakage current: weak coupling

We start by dealing with the weak coupling case. Since we are interested in the subgap region of the  $I$ - $V$  characteristic,  $k_B T_{\text{jun}}, eV \ll \Delta$ , the behavior of the function  $P(E)$  at energies  $E > -\Delta$  is irrelevant. Therefore we can ignore the elastic contributions in Eq. (1.9). Evaluating the integral over frequencies in Eq. (1.9), the relevant contribution to the function  $P(E)$  for energies  $E \neq 0$  reads

$$P(E) \simeq 2 \frac{\Re[Z_{\text{tot}}(E/\hbar)]}{R_K} \left( \frac{1+n(E)}{E} \right). \quad (1.10)$$

Here  $n(E) = [e^{\beta_{\text{env}} E} - 1]^{-1}$  is the Bose-Einstein distribution of the photons of the environment.

The probability density (1.10) can be used to get a limiting expression for  $\gamma_{\text{env}}$ ,

$$\gamma_{\text{env}} = 4 \int_{\Delta}^{+\infty} dE N_S(E) \frac{\Re[Z_{\text{tot}}(E/\hbar)]}{R_K} \frac{n(E)}{E}. \quad (1.11)$$

Let us apply this result to the example of a purely resistive external environment. This model has been used before to study devices based on tunnel junctions in connection with experiments [16, 20, 21]. Replacing the external impedance  $Z(\omega)$  of the circuit of Fig. 1.3(a) by a pure resistance  $R$ , the real part of the total impedance

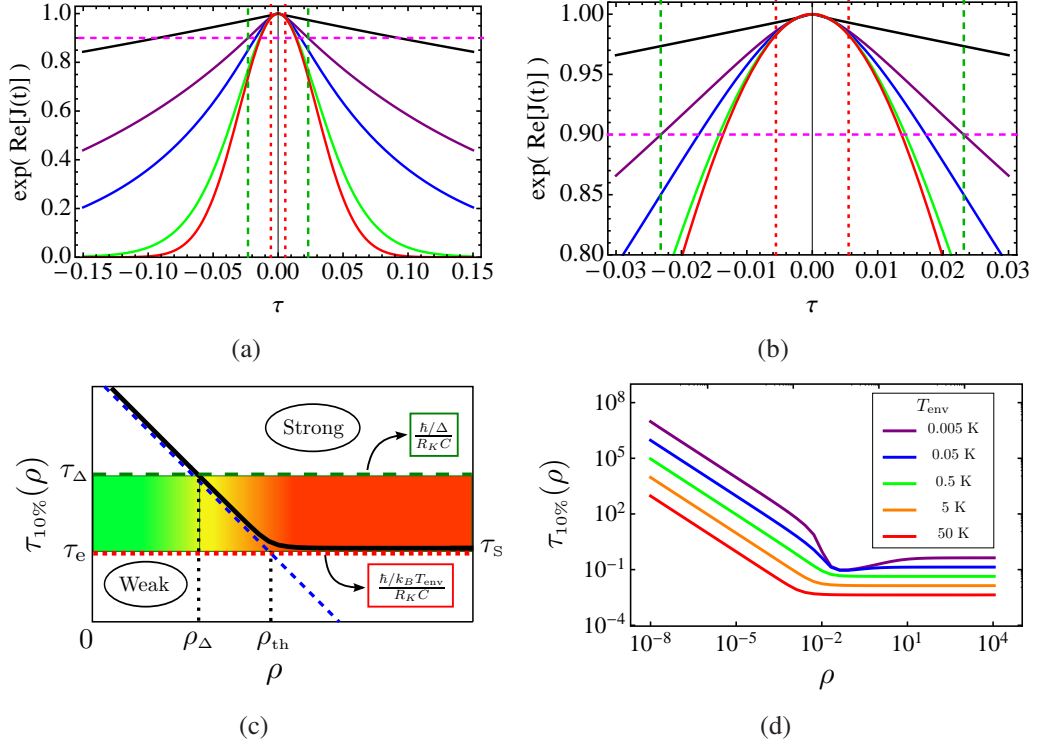


Figure 1.5: (a) Plot of  $\exp\{\Re[J(\tau, \rho)]\}$  versus the dimensionless time  $\tau = t/R_K C$  for different values of the dimensionless resistance  $\rho = R/R_K$ : 0.001 (black), 0.005, (purple), 0.01 (blue), 0.05 (green),  $\infty$  (red). Each curve is obtained using  $T_{env} = 5$  K, and  $C = 10$  fF. Also shown are the thresholds  $\pm\tau_e = \pm\hbar/k_B T_{env} R_K C$  (red dashed line) and  $\pm\tau_\Delta = \pm\hbar/\Delta R_K C$  (dark green dashed line). The latter time refers to Aluminum with  $\Delta \simeq 200$   $\mu$ eV. The horizontal magenta dashed line indicates  $\exp\{\Re[J(\tau, \rho)]\} = 0.9$ . (b) Close view of the plot in panel (a). (c) - (d) Plot of the separatrix  $\tau_{10\%}(\rho)$  as a function of  $\rho = R/R_K$ , defined as the solution of the equation  $\exp\{\Re[J(\tau_{10\%}, \rho)]\} = 0.9$  with  $C$  fixed. Both plots are in double logarithmic scale. (c) For a fixed value of  $T_{env}$ ,  $\tau_{10\%}(\rho)$  separates the weak and strong coupling regions (black thick line). The colored strip indicates the time interval bound by  $\tau_\Delta$  (dark green dashed line) and  $\tau_e$  (red dashed line). The intersection between  $\tau_\Delta$  and the separatrix  $\tau_{10\%}(\rho)$  defines the resistance  $\rho_\Delta$ . The asymptotic expression for  $\tau_{10\%}(\rho)$  valid for  $\rho \rightarrow 0$  and proportional to  $1/\rho$  is also shown (blue dashed line). Its intersection with the line corresponding to  $\tau_S \sim \sqrt{\hbar/k_B T_{env} R_K C}$  defines the threshold resistance  $\rho_{th}$ . On the logarithmic scale used here,  $\tau_S$  almost coincides with  $\tau_e$ . (d) As the temperature of the environment,  $T_{env}$ , is decreased, the curve  $\tau_{10\%}(\rho)$  moves up, thereby increasing the weak coupling region.

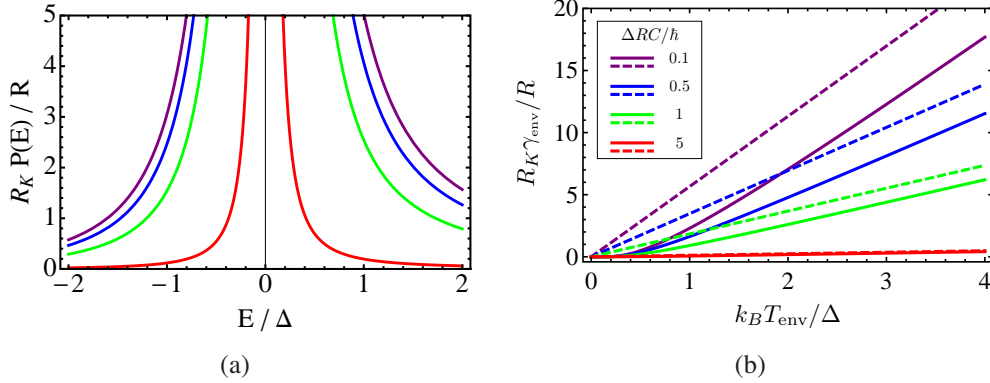


Figure 1.6: (a) Plot of the rescaled function  $R_K P(E)/R$ , Eq. (1.10), versus the energy  $E/\Delta$  for different values of the ratio  $\Delta RC/\hbar$ . (b) Plot of the rescaled parameter  $R_K \gamma_{\text{env}}/R$  as a function of  $k_B T_{\text{env}}/\Delta$  for different values of the ratio  $\Delta RC/\hbar$ . Solid lines are obtained by a numerical integration of Eq. (1.11) using Eq. (1.12). Dashed lines refer to the asymptotic  $\gamma_{\text{env}}$  given by Eq. (1.13).

is

$$\Re[Z_{\text{tot}}(\omega)] = \frac{R}{1 + (\omega RC)^2}. \quad (1.12)$$

Numerical integration of Eq. (1.11) using Eq. (1.12) is straightforward. Results for  $R_K \gamma_{\text{env}}/R$  as a function of  $k_B T_{\text{env}}/\Delta$  are shown in Fig. 1.6(b) for various values of the parameter  $\Delta RC/\hbar$ . We see that  $\gamma_{\text{env}}$  increases monotonically with temperature. Also shown is the asymptotic linear temperature dependence of  $\gamma_{\text{env}}$  reached for temperatures  $k_B T_{\text{env}} \gg \Delta$ ,

$$\gamma_{\text{env}} \simeq 2\pi \frac{R}{R_K} \frac{k_B T_{\text{env}}}{\Delta} \left[ 1 - \frac{\Delta RC/\hbar}{\sqrt{1 + (\Delta RC/\hbar)^2}} \right]. \quad (1.13)$$

This high-temperature expression is correct up to a constant shift  $\approx \Delta/k_B$  along the temperature axis (see Fig. 1.6(b)). From Fig. 1.6(b) we see that as the parameter  $\Delta RC/\hbar$  is increased, the slope characterizing the limiting dependence decreases: photon-assisted inelastic tunneling is effectively reduced by increasing the junction capacitance. Note that in the limit  $\Delta RC/\hbar \ll 1$  the result (1.13) tends to  $\gamma_{\text{env}}^{\text{D}} = 2\pi(R/R_K)(k_B T_{\text{env}}/\Delta)$ . This formula has been already obtained in Ref. [16] using  $P(E)$  theory under similar conditions, but for any bias voltage, using a high-temperature expansion for the environment, see also Ref. [22]. Consequently, the subgap parameter  $\gamma_{\text{env}}^{\text{D}}$  coincides with the Dynes parameter  $\gamma_{\text{Dynes}}$ . In other words, within this limiting case, the thermal energy  $k_B T_{\text{env}}$  determines the NIS junction's  $I$ - $V$  characteristic even around the superconducting gap,  $e|V| \sim \Delta$ , as illustrated in Ref. [16].

### 1.1.4 Subgap leakage current: strong coupling

We do not aim to present a general analysis in the strong coupling limit. In the particular case where  $\Re[Z_{\text{tot}}(\omega)]$  is strongly peaked around  $\omega = 0$ , the probability density  $P(E)$  can be calculated explicitly [1] and results for the parameter  $\gamma_{\text{env}}$  obtained. Let us illustrate this by considering a purely resistive environment. When the resistance is big,  $R \gg R_K \Delta / k_B T_{\text{env}}$  (see Sec.1.1.2), the impedance (1.12) becomes

$$\Re[Z_{\text{tot}}(\omega)] \simeq \left( \frac{\pi}{C} \right) \delta(\omega). \quad (1.14)$$

As a result, the function  $P(E)$  is given by

$$P(E) \simeq \frac{1}{\sqrt{4\pi k_B T_{\text{env}} E_C}} \exp \left[ -\frac{(E - E_C)^2}{4k_B T_{\text{env}} E_C} \right]. \quad (1.15)$$

Here we defined the charging energy  $E_C = e^2/2C$ . Inserting the function (1.15) in equation (1.7), we find

$$\gamma_{\text{env}} = \frac{1}{\sqrt{\pi E_C k_B T_{\text{env}}}} \int_{\Delta}^{+\infty} dE N_S(E) \exp \left[ -\frac{(E + E_C)^2}{4E_C k_B T_{\text{env}}} \right]. \quad (1.16)$$

Note that this result depends on  $R$  implicitly only, through the requirement  $R \gg R_K \Delta / k_B T_{\text{env}}$ . Direct numerical integration of (1.16) yields  $\gamma_{\text{env}}$  as a function of  $k_B T_{\text{env}} / \Delta$  and  $E_C / \Delta$ , as shown in Figs. 1.7(a) and 1.7(b). Some remarks are in order at this point. First of all, for  $E_C \ll \Delta$ , the integral in Eq. (1.16) can be evaluated approximately,  $\gamma_{\text{env}} \simeq e^{-\Delta^2 / k_B T_{\text{env}} E_C}$ . As in the weak coupling regime, large values of the capacitance lead to a reduction of the parameter  $\gamma_{\text{env}}$ . Upon increasing the ratio  $E_C / \Delta$ ,  $\gamma_{\text{env}}$  will first increase, then it decreases again when  $E_C / \Delta > 1$ , which is a manifestation of the Coulomb blockade. As a function of temperature,  $\gamma_{\text{env}}$  increases monotonically, similarly to the weak coupling limit. However, rather than reaching an asymptotic linear dependence,  $\gamma_{\text{env}}$  saturates at  $\gamma_{\text{env}} = 1$  for temperatures  $k_B T_{\text{env}} E_C \gg \Delta^2$ : the noise is so strong that features of the order of the gap  $\Delta$  are washed out.

## 1.2 NIS junction coupled to a high-temperature environment by means of a transmission line

In the previous section we have studied the subgap leakage current in a NIS junction which is directly coupled to the external environment  $Z(\omega)$ . We have

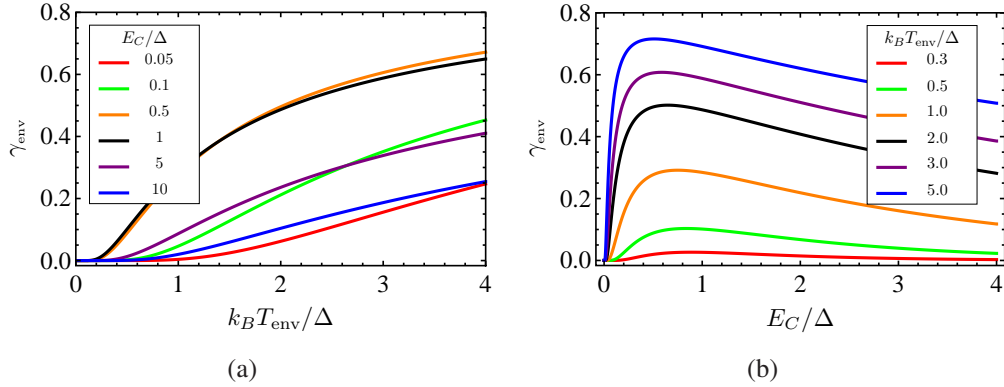


Figure 1.7: (a) Plot of the parameter  $\gamma_{env}$  as a function of  $k_B T_{env}/\Delta$  obtained considering the numerical integration of Eq. (1.16). Each curve refers to a certain fixed value of the ratio  $E_C/\Delta$  (see legend). (b) Numerical plot of the same quantity, Eq. (1.16), as a function of  $E_C/\Delta$  for different values of the ratio  $k_B T_{env}/\Delta$ , as indicated.

seen that a reduction of the subgap leakage current is possible when the capacitance of the junction,  $C$ , is increased and/or the resistance of the environment,  $R$ , is decreased. Unfortunately, in real experiments  $R$ , and in particular  $C$ , cannot be chosen arbitrarily and one needs other means to achieve the accuracy requirements for the aforementioned NIS junction's applications. We therefore consider the circuit of Fig. 1.3(b) where the junction is indirectly coupled to the external noisy impedance  $Z(\omega)$  via a low-temperature, lossy transmission line acting as a frequency-dependent filter.

### 1.2.1 Voltage fluctuations in the presence of a transmission line

In order to find the correlation function  $J(t)$  in the presence of the transmission line, we follow the method developed in Ref. [23] to solve the intermediate problem of the propagation of the noise generated by the high-temperature environment with impedance  $Z(\omega)$  through the line towards the junction, as shown in Fig. 1.8. The line has a length  $\ell$  and is described by the parameters  $R_0$ ,  $C_0$  and  $L_0$ , the resistance, the capacitance and the inductance per unit length respectively. We ignore the thermal noise produced by the impedance  $Z_J(\omega)$  and by the line, assuming both components at zero temperature. The high-temperature element produces current noise  $\delta I$  which in turn induces voltage noise  $\delta V$ .

To understand how the potential drop  $\delta V_J$  across  $Z_J(\omega)$  is connected to  $\delta V = Z(\omega) \delta I$ , we start considering the potential  $V(x)$  and the current  $I(x)$  at a given point  $x$  along the transmission line. They satisfy the two partial differential

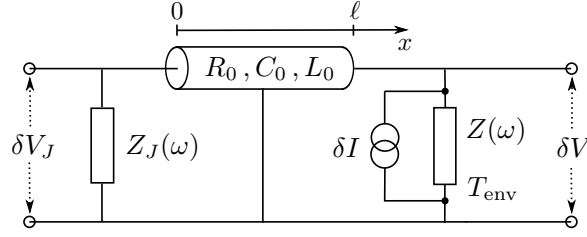


Figure 1.8: Sketch of the circuit discussed in Sec. 1.2.1.

equations,

$$\frac{\partial V(x)}{\partial x} = -I(x) [R_0 - i\omega L_0] \quad , \quad \frac{\partial I(x)}{\partial x} = i\omega C_0 V(x) .$$

Combining them one obtains the wave equation

$$\frac{\partial^2 V(x)}{\partial x^2} = -K^2(\omega) V(x) , \quad (1.17)$$

where  $K^2(\omega) = \omega^2 L_0 C_0 + i\omega R_0 C_0$  is the wave vector squared of the signal which propagates along the line. A general solution of Eq. (1.17) is given by

$$V(x) = A e^{iK(\omega)x} + B e^{-iK(\omega)x} . \quad (1.18)$$

Consequently the current along the line is

$$I(x) = \frac{1}{Z_\infty(\omega)} [A e^{iK(\omega)x} - B e^{-iK(\omega)x}] , \quad (1.19)$$

with  $Z_\infty(\omega) = i(R_0 - i\omega L_0)/K(\omega)$ . The parameters  $A$  and  $B$  can be determined by means of the boundary conditions

$$\begin{aligned} V(\ell) &= Z(\omega) [I(\ell) + \delta I] = Z(\omega) I(\ell) + \delta V \\ V(0) &= -Z_J(\omega) I(0) , \end{aligned}$$

assuming that the current flows in the counter-clockwise direction in the circuit of Fig. 1.8. After some algebra, one obtains

$$\begin{aligned} A &= -\lambda_2(\omega) B \\ B &= \left( \frac{Z_\infty(\omega) \delta V}{Z_\infty(\omega) + Z(\omega)} \right) \frac{1}{e^{-iK(\omega)\ell} - \lambda_1(\omega) \lambda_2(\omega) e^{iK(\omega)\ell}} , \end{aligned}$$

where

$$\lambda_1(\omega) = \frac{Z_\infty(\omega) - Z(\omega)}{Z_\infty(\omega) + Z(\omega)} \quad \lambda_2(\omega) = \frac{Z_\infty(\omega) - Z_J(\omega)}{Z_\infty(\omega) + Z_J(\omega)}$$

are the reflection coefficients. As a result, the potential drop  $\delta V_J = V(0) = A + B$  across the impedance  $Z_J(\omega)$  depends on the noise  $\delta V$  according to the relation

$$\delta V_J = T(\omega) \delta V . \quad (1.20)$$

In this last equation we introduced  $T(\omega)$ , the transmission function

$$T(\omega) = \frac{2 Z_\infty(\omega) Z_J(\omega)}{\left[ Z_\infty(\omega) + Z(\omega) \right] \left[ Z_\infty(\omega) + Z_J(\omega) \right]} \frac{1}{e^{-iK(\omega)\ell} - \lambda_1(\omega) \lambda_2(\omega) e^{iK(\omega)\ell}} . \quad (1.21)$$

Assuming that the potential  $\delta V$  satisfies the quantum fluctuation-dissipation theorem,

$$\left\langle \delta V(t) \delta V(0) \right\rangle_\omega = 2\hbar\omega \frac{\Re[Z(\omega)]}{1 - e^{-\beta_{\text{env}}\hbar\omega}} ,$$

the spectral density function of the potential (1.20) is

$$\left\langle \delta V_J(t) \delta V_J(0) \right\rangle_\omega = |T(\omega)|^2 2\hbar\omega \frac{\Re[Z(\omega)]}{1 - e^{-\beta_{\text{env}}\hbar\omega}} . \quad (1.22)$$

This expression describes the propagation of the noise from  $Z(\omega)$  to the noiseless impedance  $Z_J(\omega)$  through the noiseless transmission line. The voltage-voltage correlation function (1.22) is in agreement with the general formula given in Ref. [23].

## 1.2.2 Correlation function for the transmission line circuit

We use Eq. (1.22) to calculate the modified correlation function  $J_T(t)$  which appears in Eq. (1.3). According to Ref. [1],  $J(t)$  is defined as the correlation function

$$J(t) \equiv \left\langle \varphi_J(t) \varphi_J(0) - \varphi_J(0) \varphi_J(t) \right\rangle , \quad (1.23)$$

where the phase  $\varphi_J(t)$  is the time integral of the potential  $\delta V_J(t)$  across the NIS junction,

$$\varphi_J(t) \equiv \frac{e}{\hbar} \int_{-\infty}^t \delta V_J(\tau) d\tau .$$

In other words,

$$\left\langle \varphi_J(t) \varphi_J(0) \right\rangle_\omega = \left( \frac{e}{\hbar} \right)^2 \frac{1}{\omega^2} \left\langle \delta V_J(t) \delta V_J(0) \right\rangle_\omega . \quad (1.24)$$

Using the fluctuation-dissipation relation (1.22) in (1.24), we rewrite Eq. (1.23) as a function of  $T(\omega)$ ,  $Z(\omega)$  and  $T_{\text{env}}$ . Taking the impedance  $Z_J(\omega)$  to be the one of

a capacitance  $C$ , the modified function  $J_T(t)$  reads

$$J_T(t) = 2 \int_0^{+\infty} \frac{d\omega}{\omega} |T_C(\omega)|^2 \frac{\Re[Z(\omega)]}{R_K} \times \left\{ \coth\left(\frac{1}{2}\beta_{\text{env}}\hbar\omega\right) [\cos(\omega t) - 1] - i \sin(\omega t) \right\}. \quad (1.25)$$

Here  $T_C(\omega)$  is the function  $T(\omega)$ , Eq. (1.21), with  $Z_J(\omega) = Z_C(\omega) = -1/i\omega C$ . Since the transmission line is considered noiseless, its temperature  $T_{\text{line}}$  should be low,  $T_{\text{line}} \ll \Delta/k_B$ . In what follows we set  $T_{\text{line}} = 0$ .

### 1.2.3 The transmission function

In order to understand the effect of the insertion of the transmission line in the circuit of Fig. 1.3(a), a discussion about the general behavior of  $T_C(\omega)$  is necessary. In general, the modulus squared of the transmission function (1.21) is characterized by a series of resonance peaks, whose properties depend on  $\ell$ ,  $R_0$ ,  $C_0$ , and  $L_0$  as well as on the external impedance  $Z(\omega)$ . To have an idea of the behavior of  $|T_C(\omega)|^2$ , let us consider the case of a purely resistive environment,  $Z(\omega) = R$ .

Figure 1.9 illustrates the behavior of  $|T_C(\omega)|^2$  as a function of  $\omega RC$  for different values of the dimensionless parameters  $z_0 = \sqrt{L_0/C_0}/R$ ,  $c_0 = \ell C_0/C$  and  $r_0 = \ell R_0/R$ . Also shown is the Lorentzian result

$$|T_C(\omega)|^2 = 1/[1 + (\omega RC)^2] \quad (1.26)$$

found for  $\ell = 0$ , *i.e.*, in the absence of the transmission line. In other words, Eq. (1.26) describes the spectrum of the transmitted signal through a lumped RC low-pass filter. In order for the line to be an efficient filter, we require  $|T_C(\omega)|^2$  to be below this Lorentzian curve in the relevant frequency ranges. We see that both the position and the width of the resonance peaks are proportional to  $\pi/2c_0z_0$ : the longer is the transmission line, the denser around zero and the sharper are the peaks. Their height decreases rapidly as the dimensionless frequency  $\omega RC$  is increased. This can be seen in particular when the line has no losses,  $r_0 = 0$ , see Figs. 1.9(a) – 1.9(d). Although the Lorentzian curve is approached for lossless lines when  $c_0$  or  $z_0$  is reduced, we observe no real reduction below it.

A significant reduction of the height of the peaks is possible if the line which connects the NIS junction and the environment is lossy,  $r_0 \neq 0$ . Indeed, we see from Figs. 1.9(e) and 1.9(f) that the bigger is  $r_0$  the smaller are the local maxima of  $|T_C(\omega)|^2$ . Moreover, the transmission function is even much smaller than  $1/[1 +$

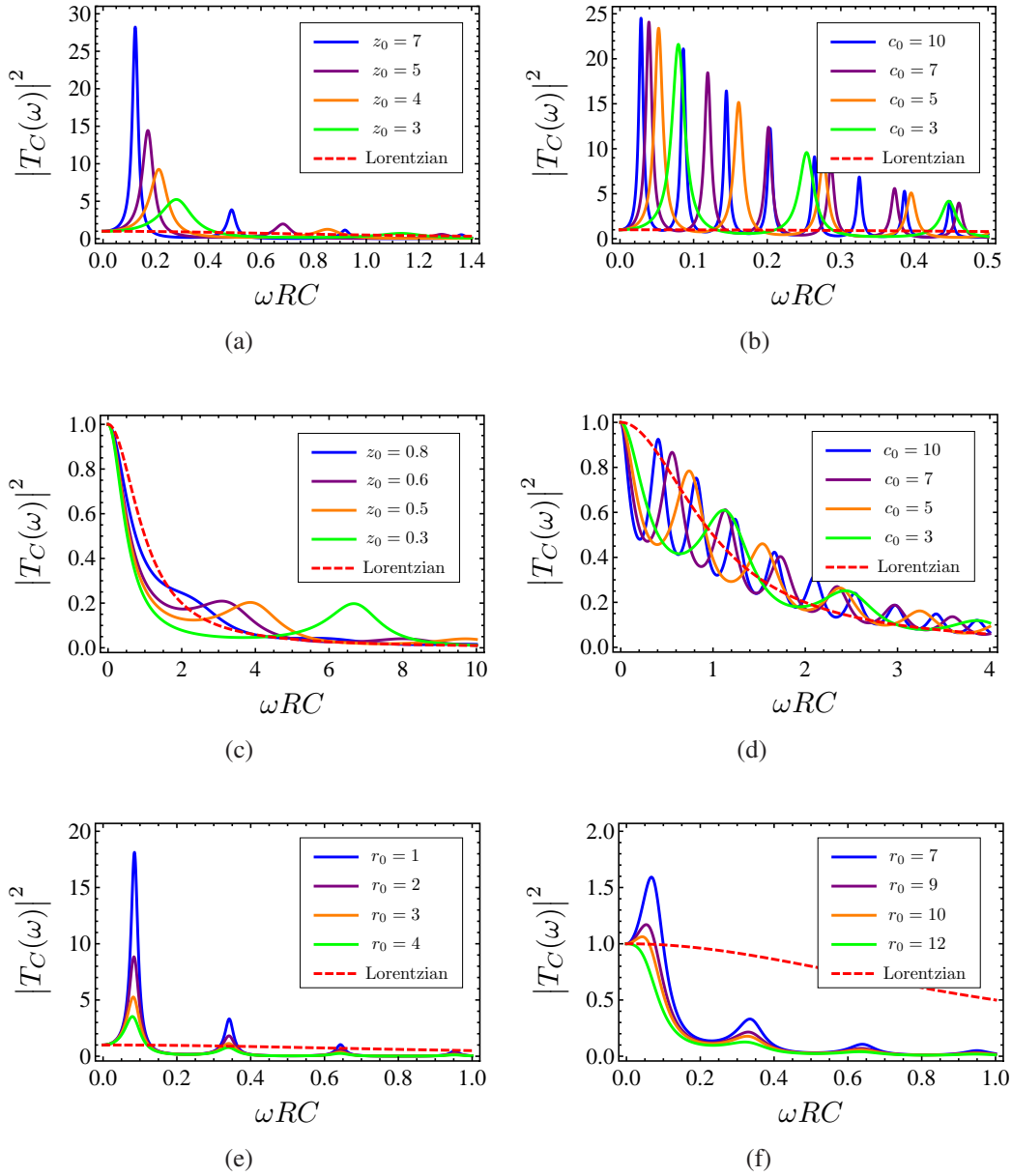


Figure 1.9: Plots of the transmission function  $|T_C(\omega)|^2$  as a function of the dimensionless variable  $\omega RC$ . Each panel corresponds to a different set of the parameters  $z_0$ ,  $c_0$ , and  $r_0$ : (a)  $r_0 = 0$ ,  $c_0 = 1$ ,  $z_0 = (7, 5, 4, 3)$ ; (b)  $r_0 = 0$ ,  $z_0 = 5$ ,  $c_0 = (10, 7, 5, 3)$ ; (c)  $r_0 = 0$ ,  $c_0 = 1$ ,  $z_0 = (0.8, 0.6, 0.5, 0.3)$ ; (d)  $r_0 = 0$ ,  $z_0 = 0.7$ ,  $c_0 = (10, 7, 5, 3)$ ; (e)  $z_0 = 10$ ,  $c_0 = 1$ ,  $r_0 = (1, 2, 3, 4)$ ; (f)  $z_0 = 10$ ,  $c_0 = 1$ ,  $r_0 = (7, 9, 10, 12)$ .

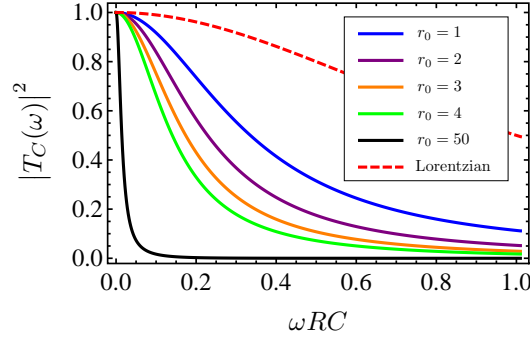


Figure 1.10: Plot of the transmission function  $|T_C(\omega)|^2$  as a function of the dimensionless variable  $\omega RC$  for different values of the parameter  $r_0$ . The other parameters are:  $c_0 = 1$ ,  $z_0 = 0.7$ . Also shown is the Lorentzian corresponding to the function  $|T_C(\omega)|^2$  in the limit  $\ell \rightarrow 0$ , given by Eq. (1.26).

$(\omega RC)^2]$  when the condition  $r_0 \gg z_0$  is satisfied, as is seen in Figs. 1.9(f) and 1.10. Therefore, within this particular limit, the insertion of a resistive transmission line may be convenient.

## 1.2.4 Subgap leakage current: weak coupling

We expect that the single- and multi-photon regimes, weak and strong coupling respectively, are strongly related to the resistance per unit length,  $R_0$ . Let us analyze the situation proceeding as in Sec.1.1.2. We consider the function  $\tau_{10\%}(\rho)$  for a purely resistive environment. In Fig. 1.11 we plot  $\tau_{10\%}(\rho)$  as a function of the dimensionless resistance  $\rho$  for different values of  $R_0$ . We see that the lossier the transmission line is, the more the weak coupling region spreads out. The resistance  $\rho_\Delta$ , given by the intersection between  $\tau_{10\%}(\rho)$  and the line corresponding to the dimensionless time  $\tau_\Delta = \hbar/\Delta R_K C$ , significantly shifts towards higher values of  $\rho$  as  $R_0$  is increased; the lossy line indeed protects the junction from the high-temperature external environment. Hereafter, we will therefore focus on a highly resistive transmission line and only the weak coupling regime will be treated.

With the help of Eq. (1.25), the function  $P(E)$  for the circuit of Fig. 1.3(b) can be obtained in the weak coupling regime. Proceeding as in Sec. 1.1.3, we find

$$P(E) \simeq 2 \left| T_C(E/\hbar) \right|^2 \frac{\Re[Z(E/\hbar)]}{R_K} \left( \frac{1+n(E)}{E} \right). \quad (1.27)$$

Evaluating the relation (1.27) for negative energies and inserting the result into

Eq. (1.7), the parameter  $\gamma_{\text{env}}$  can be written as

$$\gamma_{\text{env}} = 4 \int_{\Delta}^{+\infty} dE N_S(E) \left| T_C(E/\hbar) \right|^2 \frac{\Re[Z(E/\hbar)]}{R_K} \frac{n(E)}{E}. \quad (1.28)$$

We next specialize to the case of large resistance per unit length,  $R_0$ . In order to obtain a limiting expression for  $|T_C(\omega)|^2$  for  $R_0 \rightarrow \infty$ , let us assume that the inductive properties of the line are negligible compared to  $R_0$ . Since the relevant frequency scale is given by  $\Delta/\hbar$ , this means that the condition  $R_0 \gg L_0\Delta/\hbar$  should hold. Within this  $RC$  limit, we find that the wave vector  $K(\omega)$  of the signal propagating through the transmission line has an imaginary part equal to  $\sqrt{\omega R_0 C_0}/2$ . As a result, the amplitude of the noise is exponentially attenuated along the line (see Eqs. (1.18) and (1.19)) being proportional to  $\exp[-\ell\sqrt{2\omega R_0 C_0}]$ . We see that the bigger  $\ell$  and  $R_0$  are, the smaller is the voltage noise which reaches the junction. In particular, an exponential suppression of the propagating signal is achieved when the inequality  $\ell\sqrt{2\Delta R_0 C_0/\hbar} \gg 1$  is valid as well. This additional condition allows us to write the equation<sup>3</sup>

$$\begin{aligned} \left| e^{-iK(\omega)\ell} - \lambda_1(\omega)\lambda_2(\omega) e^{iK(\omega)\ell} \right|^2 &= e^{\ell\sqrt{2\omega R_0 C_0}} \left\{ 1 + |\lambda_1\lambda_2|^2 e^{-2\ell\sqrt{2\omega R_0 C_0}} \right. \\ &\quad \left. - 2\Re[\lambda_1\lambda_2 e^{i\ell\sqrt{2\omega R_0 C_0}}] e^{-\ell\sqrt{2\omega R_0 C_0}} \right\} \\ &\simeq 4 e^{\ell\sqrt{2\omega R_0 C_0}}. \end{aligned} \quad (1.29)$$

Then the modulus squared of the transmission function  $T_C(\omega)$  becomes

$$\left| T_C(\omega) \right|^2 \simeq \left| \frac{Z_\infty(\omega) Z_C(\omega) e^{-\ell\sqrt{2\omega R_0 C_0}/2}}{[Z_\infty(\omega) + Z(\omega)][Z_\infty(\omega) + Z_C(\omega)]} \right|^2 \quad (1.30)$$

where  $Z_\infty(\omega) \simeq (1+i)\sqrt{R_0/2\omega C_0}$  for a line in the  $RC$  limit. Combining the two conditions used so far, we find that the approximated function (1.30) holds when the resistance of the transmission line,  $\ell R_0$ , is much bigger than its characteristic impedance  $Z_\infty = \sqrt{L_0/C_0}$ .

Increasing the resistance per unit length,  $R_0$ , one also expects that interference effects become negligible. Indeed, when  $R_0$  is very big, the amplitude of the signal across the junction is much smaller than its starting value and its reflected counterpart vanishes rapidly before reaching the noise source again. In terms of our description of the transmission line given in Sec. 1.2.1, this happens when the reflection coefficients  $\lambda_1(\omega)$  and  $\lambda_2(\omega)$  tend to 1. In fact, in this

<sup>3</sup>approximating the expression inside the braces with the factor 4 guarantees that  $T_C(0) = 1$ .

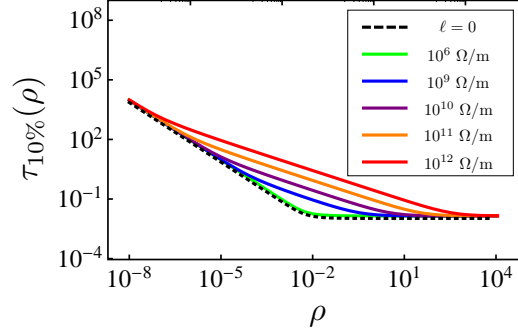


Figure 1.11: Plot of the dimensionless time  $\tau_{10\%}(\rho)$  as a function of the dimensionless resistance  $\rho = R/R_K$  for different values of the resistance per unit length,  $R_0$ , of the transmission line (see legend). Also shown is the curve  $\tau_{10\%}(\rho)$ , valid for the circuit of Fig. 1.3(a) (black dashed line). The value of the other parameters are:  $\Delta \simeq 200 \mu\text{eV}$  (energy gap of Aluminum),  $T_{\text{env}} = 5 \text{ K}$ ,  $C = 10 \text{ fF}$ ,  $C_0 = 6 \epsilon_0$ ,  $L_0 = \mu_0$ ,  $\ell = 10 \mu\text{m}$ .

limit, the potential drop (1.18) tends to 0 across the junction and to  $\delta V$  across the impedance  $Z(\omega)$ . For a purely resistive environment, this regime is reached when  $R_0$  is such that the two inequalities  $R^2 \ll \hbar R_0 / 2C_0 \Delta$  and  $\Delta R_0 C^2 / \hbar C_0 \gg 2$  hold, in other words, when the resistance of the environment,  $R$ , is much smaller than  $R_0 C / 2C_0$ . Equation (1.30) then reduces to the asymptotic expression

$$\begin{aligned} |T_C(\omega)|^2 &= e^{-\ell\sqrt{2\omega R_0 C_0}} \left[ 1 + \left( 2 + \frac{RC_0}{R_0 C} \right) (\omega RC) + \left( 1 + \frac{R_0}{\omega C_0 R^2} \right) (\omega RC)^2 \right. \\ &\quad \left. + \left( \frac{1}{R} + \frac{2C_0}{R_0 C} \right) (\omega RC)^2 \sqrt{\frac{R_0}{2\omega C_0}} + \left( \frac{1}{R} + \frac{C_0}{R_0 C} \right) (\omega RC) \sqrt{\frac{R_0}{2\omega C_0}} \right]^{-1} \\ &\simeq \frac{e^{-\ell\sqrt{2\omega R_0 C_0}}}{1 + \omega R_0 C^2 / C_0}. \end{aligned} \quad (1.31)$$

Unlike the lumped RC low-pass filter described by the  $1/\omega$ -decaying Eq. (1.26), in this case we see that the amplitude of the transmitted frequencies relevant for the photon-assisted tunneling is exponentially suppressed as the length,  $\ell$ , and the resistance per unit length,  $R_0$ , of the line are increased. By means of Eq. (1.31), the integral in Eq. (1.28) can be evaluated approximately with the result<sup>4</sup>

$$\gamma_{\text{env}} \simeq 4 \frac{R}{R_K} \frac{1}{e^{\Delta/k_B T_{\text{env}}} - 1} \sqrt{\frac{\pi}{\ell \sqrt{2\Delta R_0 C_0 / \hbar}}} \frac{e^{-\ell\sqrt{2\Delta R_0 C_0 / \hbar}}}{1 + \Delta R_0 C^2 / \hbar C_0}. \quad (1.32)$$

<sup>4</sup>when  $\ell$  and  $R_0$  are large,  $\ell \sqrt{2\Delta R_0 C_0 / \hbar} \gg 1$ , the main contribution to the integral Eq. (1.28) is obtained for  $E \simeq \Delta$ . Then the following approximations hold:  $\sqrt{E^2 - \Delta^2} \approx \sqrt{2\Delta} \sqrt{E - \Delta}$ ;  $\exp[E/k_B T_{\text{env}}] \approx \exp[\Delta/k_B T_{\text{env}}]$ ;  $\sqrt{E/\Delta} \approx 1/2 + E/2\Delta$ .

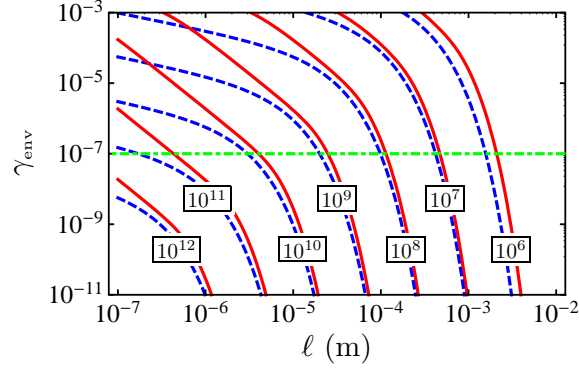


Figure 1.12: Plot of the parameter  $\gamma_{\text{env}}$ , Eq. (1.28), as a function of the length of the transmission line  $\ell$ . The red solid line is obtained by means of the numerical integration of Eq. (1.28) for a purely resistive environment. The blue dashed line is the plot of the asymptotic parameter given by the Eq. (1.32). These two curves are plotted for different values of the resistance per unit length  $R_0$  ( $\Omega/\text{m}$ ) (as indicated in the graph). All the plots are obtained considering the gap parameter of the aluminum,  $\Delta \simeq 200 \mu\text{eV}$ . The other parameters are:  $T_{\text{env}} = 5 \text{ K}$ ,  $C = 10 \text{ fF}$ ,  $R = 10 \Omega$ ,  $C_0 = 6 \varepsilon_0$ ,  $L_0 = \mu_0$ .

We notice that also the asymptotic parameter  $\gamma_{\text{env}}$  decreases exponentially in terms of  $\ell$  and  $R_0$ ; the dependence on the junction capacitance  $C$  is rather weak. The insertion of a highly resistive and noiseless transmission line between the NIS junction and the high-temperature environment indeed helps to suppress the sub-gap leakage current. The plot of Fig. 1.12 shows the exponential decay for a set of values of  $R_0$  and  $\ell$  that can be used in real experiments. Particularly interesting is the region where  $10^8 \Omega/\text{m} \lesssim R_0 \lesssim 10^{10} \Omega/\text{m}$  and  $10 \mu\text{m} \lesssim \ell \lesssim 10^2 \mu\text{m}$ . A transmission line with these values of  $R_0$  and  $\ell$  allows one to go far below  $\gamma_{\text{env}} \simeq \gamma_{\text{Dynes}}^{\text{sub}} \sim 10^{-7}$ , *i.e.*, a value of  $\gamma_{\text{env}}$  which guarantees the achievement of the accuracy requirements for the superconducting gap-based technological applications of the NIS junction [10].

### 1.3 Multi-particle tunneling

Our analysis focuses on the single-particle subgap current through the NIS junction. We ignore the contribution due to higher order processes in tunneling, such as Andreev reflection [13–15]. Hence, in order to establish the validity of our single-particle tunneling assumption, one has to compare the parameter  $\gamma_{\text{env}}$  characterizing the leakage current with the dimensionless Andreev subgap conductance  $g_A = G_A R_T$ . In ballistic junctions, second-order perturbation theory yields

the standard two-particle subgap conductance

$$G_A \simeq R_K / [R_T^2 (k_F^2 S)], \quad (1.33)$$

where  $k_F^2 S$  is the number of conduction channels in the tunnel barrier. Two-electron tunneling can be ignored as long as  $\gamma_{\text{env}} > R_K / R_T k_F^2 S$ . Typical estimates [15] yield  $R_K / R_T k_F^2 S \sim 10^{-7}$ .

On the other hand, in the diffusive case the electrons reflected by the barrier are backscattered by the impurities randomly situated close to the barrier in the normal metal. Interference between the electrons in a region characterized by the coherence length  $\xi_N = \sqrt{\hbar D / \max\{eV, k_B T_{\text{jun}}\}}$ , where  $D$  is the diffusion coefficient, affects the two-particle tunneling probability [24, 25]. As a result,  $G_A$  is given by

$$G_A \simeq R_N / R_T^2 \quad (1.34)$$

where  $R_N$  is the resistance of the diffusive normal metal over a length  $\xi_N$ . General estimates are hard to give in this situation, since the result is strongly geometry-dependent; the condition  $\gamma_{\text{env}} > R_N / R_T$  will be more stringent than the one for the ballistic case, especially under subgap conditions where  $\xi_N$  and hence  $R_N$  can be large.

Should Andreev reflection become dominant, one can always suppress it efficiently using the Coulomb blockade feature [15] that suppresses two-particle tunneling more strongly than single-particle tunneling.

## 1.4 Conclusions

In conclusion, we studied the single-particle tunneling current through a voltage-biased NIS junction. Due to the presence of the superconducting energy gap  $\Delta$  in the BCS density of states, when the junction is kept at the temperature  $T_{\text{jun}} \ll \Delta / k_B$  no current is expected to flow within the subgap region  $-\Delta < eV < \Delta$ . Actually, even if the higher order tunneling processes are suppressed, a small subgap current is still measured experimentally. This leakage current limits the accuracy in applications involving NIS junctions. The origin of the leakage current is the exchange of energy exceeding the gap  $\Delta$  between the junction and the external high-temperature environment in which it is embedded. We studied this mechanism analytically and numerically. In particular, we found that a low-temperature and lossy transmission line inserted between the junction and the environment reduces exponentially the subgap leakage current acting as a frequency-dependent filter. This indirect configuration helps to achieve the required suppression of noise.

# Effect of Photon-Assisted Andreev Reflection in the Accuracy of a SINIS Turnstile

## Introduction

The experimental realization of a quantum electric current standard is one of the scientific and technological challenges of the present time. This is a key goal in metrology because it would lead to a modern definition of Ampere as well as to the most accurate comparison of the fundamental constants  $R_K = h/e^2$  and  $K_J = 2e/h$  [26]. Among the devices proposed until now [27–32], the hybrid SINIS single-electron transistor (SET) depicted in Fig. 2.1 is one of the most interesting candidates [33]. Such a device is formed of a normal-metal (N) island joined to two superconducting (S) electrodes via two tunnel junctions with capacitances  $C_S$  for the source (S) and  $C_D$  for the drain (D). The entire structure is biased with a constant voltage  $V_D - V_S = V$ . The amount of electric charge localized on the island is controlled using a gate potential  $V_g(t)$ , capacitively coupled to N by means of a gate with capacitance  $C_g$ . Typically, the charging energy of the island  $E_C = e^2/2C_\Sigma$ , with  $C_\Sigma = C_S + C_D + C_g$ , governs the tunneling processes in the SET, i.e., the system works in the Coulomb blockade regime. Additional energy filtering is provided by the two outer superconductors which protect the device against unwanted tunneling events. In this context, if the single-electron tunneling is the dominant process, a periodic  $V_g(t)$  signal with frequency  $f$  generates an electric current  $I$  through the SET which is equal to  $ef$ . In other words, the SET is a frequency-to-current converter. However, high-order tunneling events occur in addition to the single-particle ones. They limit the conversion accuracy of this electronic turnstile thereby acting as error sources. The main contribution to the total error is usually provided by elastic and inelastic cotunneling [34, 35] as well as Andreev reflection and Cooper-pair cotunneling [36, 37]. From the theoretic-

cal point of view, it has been shown that all these processes may be eliminated efficiently thereby reaching the metrological requirements [36]. Nevertheless, in real experiments the achievement of the accuracy needed for the completion of the so-called quantum metrological triangle remains a difficult task. In particular, a residual Andreev tunneling current affects the I-V characteristic of the SET turnstile although the increase of the charging energy  $E_C$ , with respect to the gap parameter  $\Delta$  of the superconductors leads to a decrease of Andreev reflection probability [37]. Such a two-electron current noise may be due to the effect of the high-temperature electromagnetic environment the SINIS device is coupled with. The energy provided by such an external thermal bath to the SET via the exchange of photons can promote tunneling of particles through the single junction [16, 38]. In this chapter, we show that, indeed, the environment-assisted Andreev reflection limits the turnstile accuracy, unless it is properly taken care of.

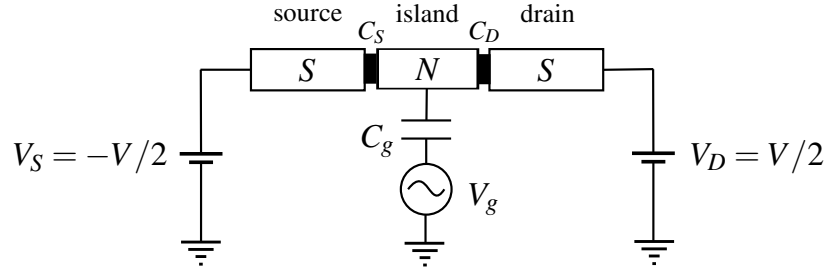


Figure 2.1: Hybrid SINIS single-electron transistor (SET). The black parts stand for the insulating barriers of the tunnel junctions.

## 2.1 Electronic transport in a SINIS turnstile

In the Coulomb blockade regime, the electronic transport in the SINIS device of Fig. 2.1 is determined by the charging energy  $E_C$ . For a symmetric device,  $C_S = C_D = C$ , assuming that initially the excess electric charge localized on the island is  $-ne$ , with  $n$  an integer, the energy cost to add ( $+N$ , in) or remove ( $-N$ , out)  $N$  extra-electrons to or from the central normal-metal electrode is given by

$$\begin{aligned} E_D^{\text{in/out}}(n, N) &\equiv E_{\text{island}}^D(n \pm N) - E_{\text{island}}^D(n) = \\ &= E_C N^2 \pm \frac{1}{2} e V N \pm 2 E_C (n - n_g) N, \end{aligned} \quad (2.1)$$

if the tunneling process occurs through the drain (D), and

$$\begin{aligned} E_S^{\text{in/out}}(n, N) &\equiv E_{\text{island}}^S(n \pm N) - E_{\text{island}}^S(n) = \\ &= E_C N^2 \mp \frac{1}{2} e V N \pm 2 E_C (n - n_g) N, \end{aligned} \quad (2.2)$$

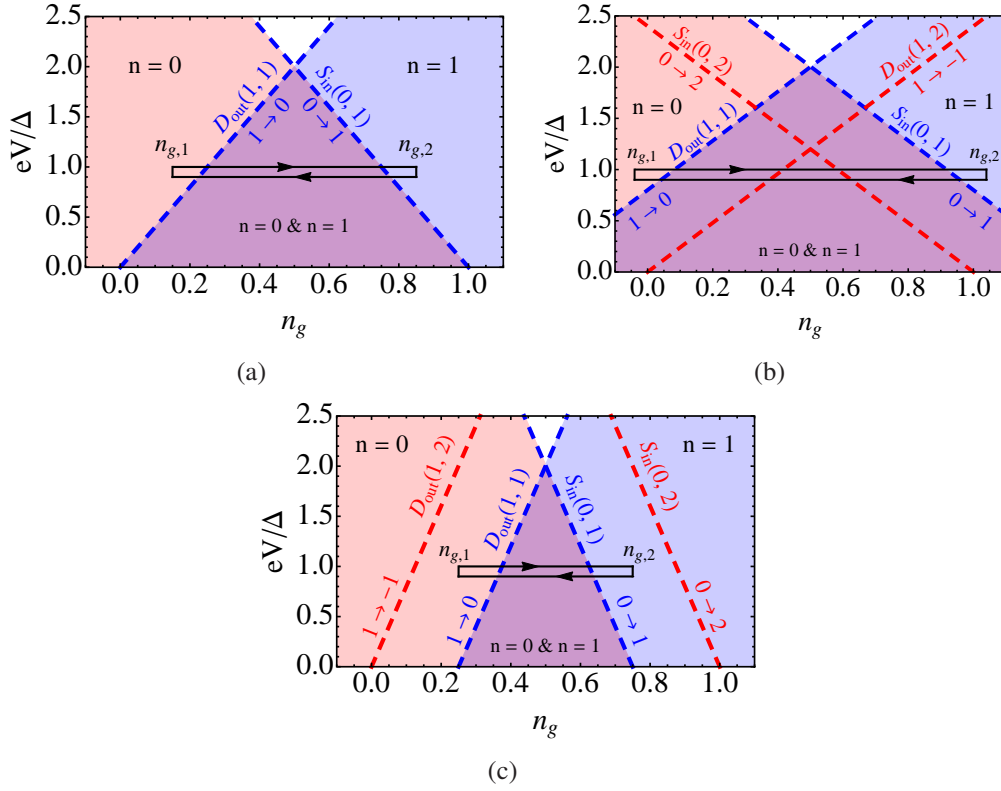


Figure 2.2: Close view of the overlapping region between the Coulomb diamonds for  $n = 0$  and  $n = 1$  obtained using (a)  $E_C/\Delta = 1$ , (b)  $E_C/\Delta = 0.6$ , and (c)  $E_C/\Delta = 2$ . Also shown are the single- (dashed blue lines) and two-particle (dashed red lines) thresholds and the optimal loop (solid black lines) at  $eV \simeq \Delta$  from  $n_g = n_{g,1}$  to  $n_g = n_{g,2}$ .

when the insulating barrier of the source (S) is overcome (see Appendix A). In Eqs. (2.1), and (2.2), the total energy of the island  $E_{\text{island}}^i(n \pm N)$ , with  $i = S, D$ , is the difference between the electrostatic energy due to the Coulomb interactions involving also the induced charge, and the work done by all the voltage sources to increase or decrease  $n$  with the tunneling of  $N$  particles through one of the insulating layers;  $n_g = C_g V_g / e$  is the gate-induced charge [1, 39].

### 2.1.1 Single-electron tunneling

Due to the energy gap in the BCS density of states of a superconductor, single-electron tunneling events ( $N = 1$ ) are energetically allowed above the gap, i.e., when the changes in energy Eqs. (2.1), and (2.2) are smaller than  $-\Delta$ . On the contrary, above  $-\Delta$  the excess charge  $-ne$  of the island remains fixed to its initial

value. Per each  $n$ , the threshold conditions  $E_D^{\text{in/out}}(n, 1) = -\Delta$  and  $E_S^{\text{in/out}}(n, 1) = -\Delta$  give rise to four crossing lines in the plot of the total bias voltage  $V$  as a function of the gate-induced charge  $n_g$ . The four intersection points between these lines are the edges of the so-called Coulomb diamond which is a stability region for the system. This means that no single-electron tunneling process can occur for the values of  $V$  and  $n_g$  within its area. Unlike the case of a fully normal SET, NININ, the Coulomb diamonds for a SINIS device corresponding to different  $n$  overlap (see Appendix A). Specifically, when  $E_C \sim \Delta$ , the stability region for a given  $n$  shares two distinct portions of the  $V$  vs  $n_g$  plane with the  $n + 1$  and  $n - 1$  diamonds, i.e., in each overlapping area at most two different values of  $n$  are stable. This feature is at the basis of the generation of a controlled and synchronized single-electron current through the hybrid single-island structure of Fig. 2.1. In this regard, let us consider, for instance, the plot of Fig. 2.2(a) where a close view of the Coulomb diamonds corresponding to  $n = 0$  and  $n = 1$  and their shared part are shown. In principle, to have a cycle corresponding to a single-particle transfer from the source to the drain,  $n_g$  has to move along a closed path in the  $V$  vs  $n_g$  plane which connects the diamonds where  $n = 0$  and  $n = 1$  are stable. Thanks to the presence of the overlapping region, this kind of connection can be realized avoiding the part of the plane where both  $n = 0$  and  $n = 1$  are unstable. As a result, each single-electron tunneling event to/from the central island can be controlled by means of the gate potential  $V_g$ . During each cycle of  $n_g$  along the working loop, the bias voltage  $V$  is usually kept fixed close to  $\Delta/e$ . For this optimal value, the superconducting energy gap  $\Delta$  guarantees an efficient suppression of thermally-activated tunneling events and quasi-particle excitations as well as elastic and inelastic cotunneling processes [33, 36]. A typical loop used in real experiments with these features is shown in Fig. 2.2(a). Starting from  $n_g = n_{g,1}$ , the number of excess electrons localized on island, whose initial value is  $n = 0$ , remains constant until the threshold  $S_{\text{in}}(0, 1)$ , defined by the equation  $E_S^{\text{in}}(0, 1) = -\Delta$ , is crossed. At that point one electron can enter in the central electrode via the source junction and  $n$  passes from 0 to 1. Once  $n_g = n_{g,2}$  is reached, the closed path is covered backward. The extra electron on the island can tunnel out through the drain only after overcoming the threshold  $D_{\text{out}}(1, 1)$ , given by the equation  $E_D^{\text{out}}(1, 1) = -\Delta$ . When  $n_g$  is again equal to  $n_{g,1}$ , the island is back in its initial state and a new cycle can start. Since per each cycle exactly one electron is transferred from the source to the drain, driving  $n_g$  from  $n_{g,1}$  to  $n_{g,2}$  and back to  $n_{g,1}$  with a signal with frequency  $f$  allows to generate the single-electron current  $I = ef$ .

### 2.1.2 Andreev reflection and higher-order processes

In addition to single-electron tunneling events, the current flowing through a SINIS transistor is, in general, also affected by the Andreev reflection, i.e., the transfer of two-electrons per unit of time inside or outside the island [13, 40]. This second-order tunneling process is insensitive to the energy barrier provided by the superconducting gap. This means that the rate of the transitions  $n \rightarrow n \pm 2$  can be relevant although the device is working at the optimal bias,  $eV \simeq \Delta$ . As a result, the Coulomb diamonds for the Andreev reflection events are obtained just imposing that the energies Eqs. (2.1) and (2.2) for  $N = 2$  are smaller than zero (see Appendix A). However, as shown in Figs. 2.2(b) and 2.2(c), the energy  $\Delta$ , together with the charging energy  $E_C$ , plays an important role in the determination of the two-electron tunneling probability. If the ratio  $E_C/\Delta$  is smaller than 1, the Andreev diamonds are contained within the single-particle stability regions. In this case, we see from Fig. 2.2(b) that the optimal loop crosses the two-particle threshold  $S_{\text{in}}(0, 2)$ , given by the equation  $E_S^{\text{in}}(0, 2) = 0$ , before the single-electron line  $S_{\text{in}}(0, 1)$ , while going from  $n_{g,1}$  to  $n_{g,2}$ . When  $n_g$  is decreased back to  $n_{g,1}$ , the closed path overcomes  $D_{\text{out}}(1, 1)$  after  $D_{\text{out}}(1, 2)$ , the line corresponding to  $E_D^{\text{out}}(1, 2) = 0$ . It follows that, in this regime, the control of single-electron tunneling is compromised by the Andreev transitions  $0 \rightarrow 2$  and  $1 \rightarrow -1$ . On the other hand, when  $E_C/\Delta > 1$ , the single-particle diamonds are smaller than the ones for Andreev reflection. Now, the two-particle thresholds can be avoided, as shown in Fig. 2.2(c), thereby suppressing the probability to increase/decrease the charge of the island by two electrons per each tunneling event (see Appendix A for more details).

However, higher-order processes, such as the cotunneling of one electron and one Cooper-pair [36], can occur while  $n_g$  covers the loop of Fig. 2.2(c). They can limit the single-electron transfer accuracy even if  $E_C/\Delta > 1$ . In particular, the more the system stays in the overlapping region where more than one charge state is stable, the bigger the effect of unwanted transitions would be. To decrease the influence of the higher-order error events, the signal  $n_g(t)$  which is usually used to go from  $n_{g,1}$  to  $n_{g,2}$  and back to  $n_{g,1}$  is a square-wave. This choice guarantees that the time spent in between  $n_{g,1}$  and  $n_{g,2}$  is minimized. On the other hand, the period  $\tau = 1/f$  of  $n_g(t)$  has to be long enough in order for the single-particle tunneling processes to take place. If the number  $n$  changes by one electron with the rate  $\Gamma_{1e}$ , then the tunneling error or probability that the charge of the island remains the same is  $\varepsilon \sim \exp(-\Gamma_{1e}/2f)$ . In particular, the requirement  $\varepsilon \lesssim \varepsilon_{\text{metr}} = 10^{-8}$  has to be satisfied for the definition of the quantum current standard. This means that the operation frequency has to be  $f \simeq 20$  MHz in order to have the metrological current  $I = e\Gamma_{1e} \simeq 100$  pA [36].

## 2.2 Environment-assisted Andreev reflection

### 2.2.1 The effect of the electromagnetic environment on the electronic transport

As discussed in the previous section, the tunneling processes involving more than one electron may be reduced biasing the SINIS turnstile at the optimal value  $eV \simeq \Delta$ , considering  $E_C/\Delta > 1$  and using for  $n_g(t)$  a square-wave-like signal which oscillates with frequency  $f$  between the two induced gate charges  $n_{g,1}$  and  $n_{g,2}$  of Fig. 2.2(c). Under these conditions, one expects to measure the current  $I = ef$  with a relatively high accuracy. In principle, it should be possible even going below the relative error  $\epsilon_{\text{metr}}$  required by the metrological applications. However, in real experiments, the achievement of the accuracy needed for the definition of the quantum current standard still remains a difficult task.

The coupling of the hybrid turnstile with its surrounding high-temperature electromagnetic environment may be a detrimental source of error [16]. Indeed, as discussed in Chapter 1, the absorption/emission of energy from/to such a thermal bath allows the tunneling of electrons, even when the overcoming of the insulating barrier results to be energetically forbidden for a well isolated SET. Nevertheless, the environment-assisted tunneling of quasi-particles can be efficiently suppressed using, for instance, an on chip capacitively coupled ground plane [16] and/or by means of a highly-resistive transmission line [38]. The main contribution to the leakage current observed in the I-V characteristic is typically due to the Andreev reflection. Although large charging energies,  $E_C > \Delta$ , should reduce the probability for this two-particle process to occur, the tunneling of Cooper-pairs still can have a strong influence on the current flowing through the transistor [9, 37]. The enhancement of the Andreev tunneling events due to the coupling of the system with the external bath may account for this behavior. To understand under which conditions the environment-assisted Andreev reflection can be relevant, we consider the circuit of Fig. 2.3 where we introduce the effective impedances  $Z_1(\omega)$ ,  $Z_2(\omega)$  and  $Z_g(\omega)$  to model the thermal bath. We assume also that the two junctions in the system have the same tunnel resistance  $R_T$ .

### 2.2.2 Single-photon-assisted two-electron tunneling rate

In order to find the tunneling rate of the Andreev reflection process under the effect of the electromagnetic environment, we start by considering the tunneling Hamiltonian

$$\hat{H}_T = e^{i\hat{\phi}_{\text{env}}} \sum_{\mathbf{k}, \mathbf{p}, \sigma} t_{\mathbf{k}, \mathbf{p}} \left( u_{\mathbf{p}} \hat{\gamma}_{\mathbf{p}, \sigma}^\dagger + v_{\mathbf{p}} \hat{\gamma}_{-\mathbf{p}, -\sigma} \right) \hat{a}_{\mathbf{k}, \sigma} + \text{h.c.}, \quad (2.3)$$

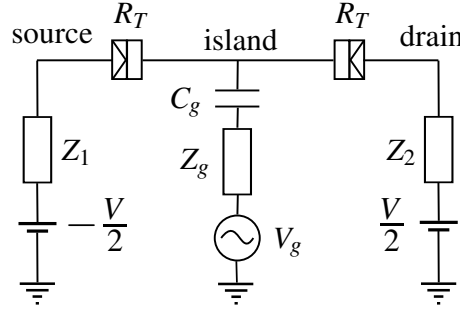


Figure 2.3: Circuit representation of the hybrid S-I-N-I-S single-electron transistor (SET). The two NIS junctions constituting the device have the same capacitance  $C$  and tunnel resistance  $R_T$  and are connected to the source  $V_S = -V/2$  and drain  $V_D = V/2$  voltages via the impedances  $Z_1(\omega)$  and  $Z_2(\omega)$  respectively. The normal metal island is controlled by means of the gate voltage  $V_g$  via the capacitance  $C_g$ . The gate impedance  $Z_g(\omega)$  together with  $Z_1(\omega)$  and  $Z_2(\omega)$  represent the electromagnetic environment at temperature  $T_{\text{env}}$ .

which accounts for the transfer of two electrons between the normal-metal island and one of the superconducting electrodes of the SINIS SET of Fig. 2.3. Equation (2.3) is written in terms of the creation  $\hat{\gamma}_{\mathbf{p},\sigma}^\dagger$  ( $\hat{a}_{\mathbf{k},\sigma}^\dagger$ ) and annihilation  $\hat{\gamma}_{\mathbf{p},\sigma}$  ( $\hat{a}_{\mathbf{k},\sigma}$ ) operators of quasiparticles (electrons) in S (N) with wave vector  $\mathbf{p}$  ( $\mathbf{k}$ ) and spin  $\sigma = \uparrow, \downarrow$ . The tunnel matrix elements  $t_{\mathbf{k},\mathbf{p}}$ , in general, depend on  $\mathbf{p}$  and  $\mathbf{k}$ . The BCS coherence factors  $u_{\mathbf{p}}$  and  $v_{\mathbf{p}}$  are spin-independent and satisfy the relations

$$u_{\mathbf{p}}^2 = 1 - v_{\mathbf{p}}^2 = \frac{1}{2} \left( 1 + \frac{\xi_{\mathbf{p}}}{\varepsilon_{\mathbf{p}}} \right) \quad , \quad u_{\mathbf{p}} v_{\mathbf{p}} = \frac{\Delta}{(\varepsilon_{\mathbf{p}}^2 - \Delta^2)^{1/2}} \quad , \quad (2.4)$$

where  $\xi_{\mathbf{p}}$  is the energy of an electron in S with momentum  $\mathbf{p}$  measured with respect to the Fermi level, and  $\varepsilon_{\mathbf{p}} = (\xi_{\mathbf{p}}^2 + \Delta^2)^{1/2}$  is the quasiparticle energy. The translation operator  $e^{i\hat{\phi}_{\text{env}}}$  in Eq. (2.3) accounts for the change of the charge of the electrodes due to the environment-assisted tunneling of one electron. Considering the environment as an infinite ensemble of quantum harmonic oscillators with temperature  $T_{\text{env}}$  (Caldeira-Leggett model [41–43]), the fluctuating phase  $\hat{\phi}_{\text{env}}$  can be written as

$$\hat{\phi}_{\text{env}} = \sum_{\lambda} \hat{\phi}_{\lambda} = \sum_{\lambda} \rho_{\lambda} \left( \hat{c}_{\lambda}^\dagger + \hat{c}_{\lambda} \right) \quad (2.5)$$

where the phase  $\hat{\phi}_{\lambda}$  represents the position operator of the harmonic oscillator  $\lambda$  with mass  $C_{\lambda}$  and characteristic frequency  $\omega_{\lambda} = 1/\sqrt{L_{\lambda}C_{\lambda}}$ . The coupling term is  $\rho_{\lambda} = (e/\hbar)\sqrt{\hbar/2C_{\lambda}\omega_{\lambda}}$ , and the operators  $\hat{c}_{\lambda}^\dagger$  and  $\hat{c}_{\lambda}$  create and annihilate one photon with energy  $\hbar\omega_{\lambda}$  (see Appendix B). Hereafter, we assume that the coupling of the SINIS with the environment is weak, meaning that at most a single

photon is involved in the exchange of energy between the system and the thermal bath [38]. In other words, we consider the limit where  $\rho_\lambda \ll 1$  and the series expansion of the charge translation operator Eq. (2.5) in  $\hat{H}_T$  can be truncated at the first order, i.e.,  $e^{i\hat{\phi}_{\text{env}}} \simeq 1 + i\hat{\phi}_{\text{env}}$ . The validity of this assumption will be discussed in the following.

Let us focus on the Andreev process  $1 \rightarrow -1$ , characterized by the transfer of two electrons from the normal metal island to the superconducting drain electrode as a Cooper pair. According to perturbation theory in  $\hat{H}_T$ , the total probability amplitude to have such a second-order event in the system of Fig. 2.3 is given by

$$A_{\mathbf{k}_1, \mathbf{k}_2}^\lambda = \sum_{m_\lambda} \frac{\langle f_\lambda | \hat{H}_T | m_\lambda \rangle \langle m_\lambda | \hat{H}_T | i_\lambda \rangle}{\zeta_{m_\lambda} - \zeta_{i_\lambda} + i\eta}, \quad (2.6)$$

for fixed values of the environmental index  $\lambda$ , and of the initial wave vectors  $\mathbf{k}_1$  and  $\mathbf{k}_2$ . Here the initial state is

$$|i_\lambda\rangle = |\mathbf{k}_1 \uparrow, \mathbf{k}_2 \downarrow\rangle_N \otimes |n_{\text{pairs}}, \mathbf{p}\rangle_S \otimes |n_\lambda + 1\rangle_{\text{env}}, \quad (2.7)$$

with two electrons in N with opposite spin and momenta  $\mathbf{k}_1$  and  $\mathbf{k}_2$ ,  $n_{\text{pairs}}$  Cooper pairs in S and no quasiparticle excitations, and  $n_\lambda + 1$  photons with energy  $\hbar\omega_\lambda$  in the environment. On the other hand, the final state is

$$|f_\lambda\rangle = |\overline{\mathbf{k}_1 \uparrow}, \overline{\mathbf{k}_2 \downarrow}\rangle_N \otimes |n_{\text{pairs}} + 1, \mathbf{p}\rangle_S \otimes |n_\lambda\rangle_{\text{env}}, \quad (2.8)$$

with an additional Cooper pair in S, two less electrons in N and one less photon in the Caldeira-Leggett bath. The transition from the state (2.7) to the state (2.8) is determined by all the possible intermediate virtual states  $|m_\lambda\rangle$  such that a quasiparticle with momentum  $\mathbf{p}$  is created in S after the annihilation of one of the two electrons in N. As illustrated in Fig. (2.4), only one of the two tunneling electrons can absorb the energy of the only available photon, in the weak coupling limit. As a result, for a fixed wave vector  $\mathbf{p}$  of the virtual quasiparticle in S, only the four intermediate states

$$\begin{aligned} |1_\lambda\rangle &= |\mathbf{k}_1 \uparrow, \overline{\mathbf{k}_2 \downarrow}\rangle_N \otimes |n_{\text{pairs}}, \mathbf{p}\rangle_S \otimes |n_\lambda + 1\rangle_{\text{env}}, \\ |2_\lambda\rangle &= |\mathbf{k}_1 \uparrow, \overline{\mathbf{k}_2 \downarrow}\rangle_N \otimes |n_{\text{pairs}}, \mathbf{p}\rangle_S \otimes |n_\lambda\rangle_{\text{env}}, \\ |3_\lambda\rangle &= |\overline{\mathbf{k}_1 \uparrow}, \mathbf{k}_2 \downarrow\rangle_N \otimes |n_{\text{pairs}}, \mathbf{p}\rangle_S \otimes |n_\lambda + 1\rangle_{\text{env}}, \\ |4_\lambda\rangle &= |\overline{\mathbf{k}_1 \uparrow}, \mathbf{k}_2 \downarrow\rangle_N \otimes |n_{\text{pairs}}, \mathbf{p}\rangle_S \otimes |n_\lambda\rangle_{\text{env}}, \end{aligned} \quad (2.9)$$

can give a non-zero contribution to  $A_{\mathbf{k}_1, \mathbf{k}_2}^\lambda$ . The difference between the energies  $\zeta_{m_\lambda}$  of these virtual states and the energy  $\zeta_{i_\lambda} - i\eta$  of the initial state  $|i_\lambda\rangle$  determine the amplitude Eq. (2.6). The imaginary part  $\eta = \hbar\Gamma_{1 \rightarrow 0}/2$  accounts for the

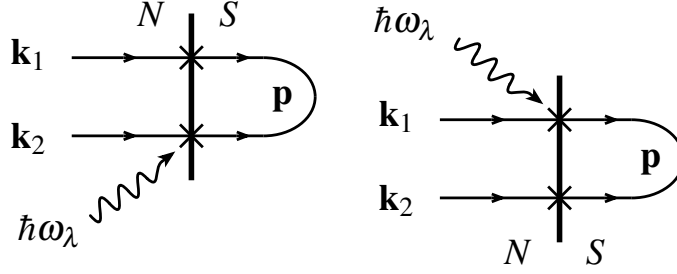


Figure 2.4: Feynman diagrams of the two possible single-photon absorption processes giving rise to the environment-assisted Andreev reflection.

lifetime broadening of  $|i_\lambda\rangle$  due to the competing single-electron tunneling processes occurring with rate  $\Gamma_{1\rightarrow 0}$ . According to perturbation theory in the tunneling Hamiltonian  $\hat{H}_T$ , the first-order rate, describing one electron going out of the island through the drain, can be written as

$$\Gamma_{1\rightarrow 0}^{\text{Dynes}} = \frac{1}{2\pi} \frac{\Delta R_K}{\hbar R_T} \int_0^{E_D^{\text{out}}(1,1)} \frac{N_S^{\text{Dynes}}(E/\Delta)}{\Delta} dE \quad (2.10)$$

in terms of the Dynes density of states of a superconductor [17],

$$N_S^{\text{Dynes}}(E/\Delta) = \left| \Re \left[ \frac{E/\Delta + i\gamma_{\text{Dynes}}}{\sqrt{(E/\Delta + i\gamma_{\text{Dynes}})^2 - 1}} \right] \right|, \quad (2.11)$$

which depends on the phenomenological Dynes parameter  $\gamma_{\text{Dynes}}$  (see Chapter 1). In Eq. (2.10),  $E_D^{\text{out}}(1,1) = 2E_C(n_g - 1/2) - eV/2$  is the energy cost that has to be paid by the voltage sources in order for the transition  $1 \rightarrow 0$  to occur [see Eq. (2.1)];  $R_K = h/e^2$  is the resistance quantum. The Dynes rate Eq. (2.10) is valid in the zero-temperature limit,  $k_B T_{\text{SINIS}} \ll \Delta$ , and takes into account the most relevant single-electron error sources, such as the environment.

Using Eqs. (2.7), (2.8), and (2.9), the amplitude Eq. (2.6) reads

$$A_{\mathbf{k}_1, \mathbf{k}_2}^\lambda = i t_0^2 \sqrt{f_{\mathbf{k}_1}} \sqrt{f_{\mathbf{k}_2}} \rho_\lambda \sqrt{n_\lambda} \sum_{\mathbf{p}} (u_{\mathbf{p}} v_{\mathbf{p}}) S_{\mathbf{p}, \lambda}, \quad (2.12)$$

for a low-temperature hybrid single-electron transistor,  $k_B T_{\text{SINIS}} \ll \Delta$ , and assuming constant tunneling matrix elements,  $t_{\mathbf{k}, \mathbf{p}} = t_{\mathbf{k}, \mathbf{p}}^* = t_0$  (point tunnel junction). In Eq. (2.12), we introduced the Fermi-Dirac distribution function  $f_{\mathbf{k}} = [\exp(\xi_{\mathbf{k}}/k_B T_{\text{SINIS}}) + 1]^{-1}$  for the normal metal electrons and the sum of the intermediate-state denominators

$$S_{\mathbf{p}, \lambda} \equiv \frac{1}{\varepsilon_{\mathbf{p}}^c - \xi_{\mathbf{k}_1} + i\eta} + \frac{1}{\varepsilon_{\mathbf{p}}^c - \xi_{\mathbf{k}_2} - \hbar\omega_\lambda + i\eta} + \frac{1}{\varepsilon_{\mathbf{p}}^c - \xi_{\mathbf{k}_2} + i\eta} + \frac{1}{\varepsilon_{\mathbf{p}}^c - \xi_{\mathbf{k}_1} - \hbar\omega_\lambda + i\eta}. \quad (2.13)$$

Here  $\varepsilon_{\mathbf{p}}^c \equiv \varepsilon_{\mathbf{p}} + E_D^{\text{out}}(1, 1)$  is the virtual state energy and  $\xi_{\mathbf{k}}$  is the energy of an electron in N with momentum  $\mathbf{k}$  measured with respect to the Fermi level. Summing over all the possible initial states and considering the spin degeneracy, one obtains the total rate

$$\Gamma_{\text{AR}}^{\text{env}} = \frac{4\pi}{\hbar} \sum_{\mathbf{k}_1, \mathbf{k}_2} \sum_{\lambda} \left| A_{\mathbf{k}_1, \mathbf{k}_2}^{\lambda} \right|^2 \delta(\xi_{\mathbf{k}_1, \mathbf{k}_2}^c + \hbar\omega_{\lambda}), \quad (2.14)$$

where  $\xi_{\mathbf{k}_1, \mathbf{k}_2}^c \equiv \xi_{\mathbf{k}_1} + \xi_{\mathbf{k}_2} - E_D^{\text{out}}(1, 2)$  is determined by the energy cost  $E_D^{\text{out}}(1, 2) = 4E_{Cn_g} - eV$  needed for the second-order transition  $1 \rightarrow -1$  to occur [see Eq. (2.1)]. The environment-assisted Andreev rate Eq. (2.14) is written in terms of the probability

$$\left| A_{\mathbf{k}_1, \mathbf{k}_2}^{\lambda} \right|^2 = t_0^4 f_{\mathbf{k}_1} f_{\mathbf{k}_2} \rho_{\lambda}^2 n_{\lambda} \sum_{\mathbf{p}, \mathbf{p}'} (u_{\mathbf{p}} v_{\mathbf{p}}) (u_{\mathbf{p}'} v_{\mathbf{p}'}) S_{\mathbf{p}, \lambda} S_{\mathbf{p}', \lambda}^*.$$

Approximating the sums over  $\mathbf{k}_1$ ,  $\mathbf{k}_2$ ,  $\mathbf{p}$  and  $\mathbf{p}'$  by the corresponding integrals, assuming that  $n_{\lambda}$  is given by the Bose-Einstein distribution,  $n_{BE}(\omega_{\lambda}) = [\exp(\hbar\omega_{\lambda}/k_B T_{\text{env}}) - 1]^{-1}$ , and using the properties of the Dirac delta function, Eq. (2.14) can be written as

$$\begin{aligned} \Gamma_{\text{AR}}^{\text{env}} &\simeq \frac{1}{2\hbar} \frac{1}{(2\pi)^3} \left( \frac{R_K}{R_T} \right)^2 \int_{-\infty}^{+\infty} d\xi_{\mathbf{k}_1} d\xi_{\mathbf{k}_2} \int_{-\infty}^{+\infty} d\xi_{\mathbf{p}} d\xi_{\mathbf{p}'} \\ &\times f_{\mathbf{k}_1} f_{\mathbf{k}_2} (u_{\mathbf{p}} v_{\mathbf{p}}) (u_{\mathbf{p}'} v_{\mathbf{p}'}) n_{BE}(-\xi_{\mathbf{k}_1, \mathbf{k}_2}^c) (-\xi_{\mathbf{k}_1, \mathbf{k}_2}^c)^{-1} \\ &\times \left( S_{\mathbf{p}} S_{\mathbf{p}'}^* \right) \sum_{\lambda} \rho_{\lambda}^2 \omega_{\lambda} \delta(\xi_{\mathbf{k}_1, \mathbf{k}_2}^c + \hbar\omega_{\lambda}). \end{aligned} \quad (2.15)$$

Here  $S_{\mathbf{p}}$  and  $S_{\mathbf{p}'}^*$  are  $S_{\mathbf{p}, \lambda}$  and  $S_{\mathbf{p}', \lambda}^*$  evaluated for  $\hbar\omega_{\lambda} = -\xi_{\mathbf{k}_1, \mathbf{k}_2}^c$ . As shown in the Appendix B, the sum over  $\lambda$  in Eq. (2.15) can be related to the effective total impedance of the electromagnetic environment  $Z_{\text{tot}}(\omega)$ , resulting from the connection in parallel of  $C_{\Sigma}$  and  $Z(\omega) = Z_1(\omega) + Z_2(\omega) + Z_g(\omega)$ , by means of the fluctuation dissipation theorem. It follows that Eq. (B.8) allows to recast  $\Gamma_{\text{AR}}^{\text{env}}$  in the form

$$\begin{aligned} \Gamma_{\text{AR}}^{\text{env}} &\simeq \frac{1}{(2\pi)^3} \frac{\Delta^2}{\hbar R_K \mathcal{N}} \left( \frac{R_K}{R_T} \right)^2 \int_{-\infty}^0 d\xi_{\mathbf{k}_1} d\xi_{\mathbf{k}_2} \int_{\Delta}^{+\infty} d\varepsilon_{\mathbf{p}} d\varepsilon_{\mathbf{p}'} \\ &\times \left( \sqrt{\varepsilon_{\mathbf{p}}^2 - \Delta^2} \sqrt{\varepsilon_{\mathbf{p}'}^2 - \Delta^2} \right)^{-1} (-\xi_{\mathbf{k}_1, \mathbf{k}_2}^c)^{-1} \left( S_{\mathbf{p}} S_{\mathbf{p}'}^* \right) \\ &\times n_{BE}(-\xi_{\mathbf{k}_1, \mathbf{k}_2}^c) \Re [Z_{\text{tot}}(\xi_{\mathbf{k}_1, \mathbf{k}_2}^c/\hbar)]. \end{aligned} \quad (2.16)$$

In this last expression, we used the BCS relation for  $u_{\mathbf{p}} v_{\mathbf{p}}$  given in Eq. (2.4) and the quasiparticle energies  $\varepsilon_{\mathbf{p}}$  and  $\varepsilon_{\mathbf{p}'}$  as integration variables. We also introduced the number of conducting channels  $\mathcal{N}$  of the junctions. The environment-assisted Andreev rate Eq. (2.16) is valid in the single-photon regime,  $\rho_{\lambda} \ll 1$ . For a purely

resistive environment,  $Z(\omega) = R$ , this condition corresponds to  $(R/R_K)(k_B T_{\text{env}}/\Delta) \ll 1$  (see Chapter 1).

Assuming that the system is working at the optimal point,  $eV = \Delta$ , and the charging energy is large,  $E_C > \Delta$ , Eq. (2.16) becomes

$$\begin{aligned} \Gamma_{\text{AR}}^{\text{env}} &\approx \gamma_{\text{env}}^{\text{D}} \frac{\Delta^2}{(2\pi)^4} \frac{\Delta}{\hbar \mathcal{N}} \left( \frac{R_K}{R_T} \right)^2 \int_{-\infty}^0 d\xi_{\mathbf{k}_1} d\xi_{\mathbf{k}_2} \int_{\Delta}^{+\infty} d\varepsilon_{\mathbf{p}} d\varepsilon_{\mathbf{p}'} \\ &\times \left( \sqrt{\varepsilon_{\mathbf{p}}^2 - \Delta^2} \sqrt{\varepsilon_{\mathbf{p}'}^2 - \Delta^2} \right)^{-1} (\xi_{\mathbf{k}_1, \mathbf{k}_2}^c)^{-2} (S_{\mathbf{p}} S_{\mathbf{p}'}^*). \end{aligned} \quad (2.17)$$

in the high-temperature limit,  $k_B T_{\text{env}} \gg E_D^{\text{out}}(1, 2) = 4E_C n_g - \Delta$  with  $(1/4) \lesssim n_g \lesssim (3/4)$ , and for

$$\Re[Z_{\text{tot}}(\omega)] = \frac{R}{1 + (\omega R C_{\Sigma})^2}. \quad (2.18)$$

The last equation is  $\approx R$  under the conditions we are considering. In Eq. (2.17), we introduced the high-temperature Dynes parameter  $\gamma_{\text{env}}^{\text{D}} = 2\pi(R/R_K)(k_B T_{\text{env}}/\Delta)$  [16, 38], which is the only term of  $\Gamma_{\text{AR}}^{\text{env}}$  which depends on the parameters characterizing the environment,  $R$  and  $T_{\text{env}}$ .

### 2.2.3 Results

Using Eq. (2.18), the numerical integration of Eq. (2.16) is relatively straightforward. Figure 2.5(a) shows the photon-assisted Andreev rate, Eq. (2.16), as a function of the gate-induced charge  $n_g$ , for a single-electron transistor biased at the optimal voltage,  $eV = \Delta$ , and with charging energy  $E_C > \Delta$ . Each curve is obtained for different values of the temperature of the environment  $T_{\text{env}}$ . The other parameters are fixed to the values of sample S3 of Ref. [37], as indicated in the figure. We see that the probability to have the tunneling of a Cooper-pair can be different from zero also away from the two-particle tunneling threshold, unlike the case without environment. In particular, the exchange of energy with the thermal bath in which the SET is embedded can make the Andreev reflection relevant even around the single-particle threshold. As a result, although the boundary of the Coulomb diamond corresponding to the transition  $1 \rightarrow -1$  is avoided by means of the loop of Fig. 2.2(c), a Cooper pair can tunnel through the barrier of the drain, while  $n_g$  goes back to  $n_{g,1}$ , before crossing the  $1 \rightarrow 0$  line. The decrease of  $T_{\text{env}}$  leads to smaller values of  $\Gamma_{\text{AR}}^{\text{env}}$  [see Fig. 2.5(a)], as well as the use of an electromagnetic environment with a smaller resistance  $R$  [see Fig. 2.5(b)]. Whereas, in the latter case, the whole Andreev rate curve is shifted down proportionally to the ratio between initial and final resistances, the modulus of the first derivative of Eq. (2.16) for  $n_g > \Delta/4E_C$  increases proportionally to  $T_{\text{env}}$ .

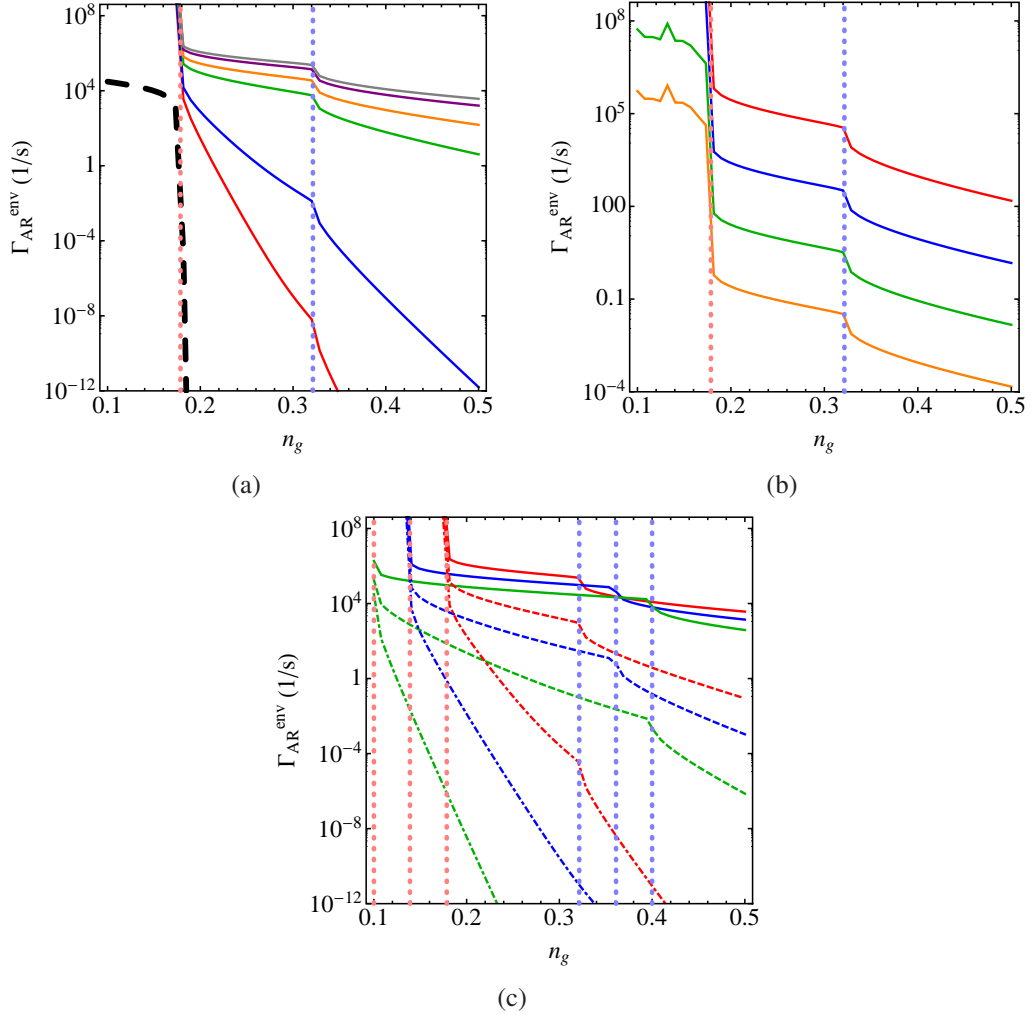


Figure 2.5: Photon-assisted Andreev rates, given by the numerical evaluation of Eq. (2.16), as a function of the gate-induced charge  $n_g$  with  $\Delta = 210 \mu\text{eV}$  (Aluminum),  $R_T = 430 \text{ k}\Omega$ ,  $\mathcal{N} = 100$ , and  $\gamma_{\text{Dynes}} = 10^{-5}$ . In panel (a), for each rate  $R = 1100 \Omega$  and  $E_C/\Delta = 1.4$ ; the values of  $T_{\text{env}}$  are: 70 mK (red), 140 mK (blue), 780 mK (green), 1.5 K (orange), 3 K (purple), 4.2 K (gray); the dashed black line is the Andreev rate valid in the absence of environment (see Ref. [36]). In panel (b), for each curve  $T_{\text{env}} = 1.5 \text{ K}$  and  $E_C/\Delta = 1.4$ ; the resistances  $R$  are: 1100  $\Omega$  (red), 10  $\Omega$  (blue), 0.1  $\Omega$  (green), 0.001  $\Omega$  (orange). In panel (c), for fixed  $R = 1100 \Omega$ , the curves with the same color are obtained using the same charging energy,  $E_C/\Delta$ : 1.4 (red lines), 1.8 (blue lines), 2.5 (green lines); the values of  $T_{\text{env}}$  are: 4.2 K (solid curves), 500 mK (dashed curves), and 100 mK (dot-dashed curves). In all the three panels, also shown are the single- and two-particle thresholds,  $1/2 - \Delta/4E_C$  (light blue vertical dotted lines), and  $\Delta/4E_C$  (light red vertical dotted lines) respectively.

The dependence of the photon-assisted Andreev rate, Eq. (2.16), on the charging energy  $E_C$  is shown in Fig. 2.5(c). The increase of the ratio  $E_C/\Delta > 1$  allows to reduce the effect of the two-particle tunneling on the total electric current sustained by the SINIS turnstile. In particular, the lower is the effective temperature of the environment with respect to the critical temperature of the superconductor, the larger is the reduction of  $\Gamma_{\text{AR}}^{\text{env}}$  upon increasing  $E_C/\Delta$ . Notice that the main effect of the change of the charging energy  $E_C$  is the shifting of the environment-assisted Andreev rate along the induced-gate charge axis by the difference between the initial and final inverse ratios  $\Delta/4E_C$ .

Assuming that the number of electrons of the metallic island of the circuit of Fig. 2.3 decreases because of the tunneling of quasi-particles and Cooper pairs only, the total rate can be written as

$$\Gamma_{\text{tot}} \simeq \Gamma_{1 \rightarrow 0}^{\text{Dynes}} + 2\Gamma_{\text{AR}}^{\text{env}}.$$

As a result, the error  $\varepsilon_{\text{acc}} \equiv 2\Gamma_{\text{AR}}^{\text{env}}/\Gamma_{1 \rightarrow 0}^{\text{Dynes}}$  determines how much the environment-assisted Andreev reflection affects the charge transport in the SINIS transistor. In particular, the condition  $\varepsilon_{\text{acc}} < 10^{-8}$  is required for the metrological applications [26]. Figure (2.6) shows the ratio  $\varepsilon_{\text{acc}}$  obtained from a numerical evaluation of Eqs. (2.16) and (2.10), as a function of  $n_g$ . We see that  $\varepsilon_{\text{acc}}$  is a non-monotonic function of  $n_g$ . Starting from the two-particle threshold occurring for  $n_g = \Delta/4E_C$ , this error first decreases exponentially as  $n_g$  is increased. Then, close to the single-particle threshold, it rises up again reaching a local maximum value around  $n_g = 1/2 - \Delta/4E_C$ . For larger  $n_g$  it tends exponentially to zero. Because of this kind of behavior,  $\varepsilon_{\text{acc}}$  can be smaller or of the order of  $10^{-8}$  when  $\Delta/4E_C < n_g < 1/2 - \Delta/4E_C$ , and, at the same time, much larger than the value required by metrology around the single-particle threshold. Consequently, the time spent by the signal used to drive  $n_g$  around  $n_g = 1/2 - \Delta/4E_C$  has to be as small as possible in order to minimize the environment-assisted Andreev reflection.

From the experimental point of view, the determination, with a relatively high accuracy, of the values of the effective parameters of the environment,  $R$  and  $T_{\text{env}}$ , is a tough challenge. The use of the Dynes parameter  $\gamma_{\text{Dynes}}$ , which in general depends also on  $R$  and  $T_{\text{env}}$ , is preferred because it can be determined from the measured current-voltage characteristic of the SINIS turnstile. In this regard, the high-temperature two-particle tunneling rate Eq. (2.17) allows to study the photon-assisted Andreev reflection in terms of  $\gamma_{\text{Dynes}}$  only. In Fig. 2.6(d), we plot the error  $\varepsilon_{\text{acc}}$  obtained using Eq. (2.17) as a function of  $n_g$ . We see that the Dynes parameter, which typically ranges from  $10^{-4}$  to  $10^{-7}$ , strongly affects  $\Gamma_{\text{AR}}^{\text{env}}$  in the range  $\Delta/4E_C < n_g < 1/2 - \Delta/4E_C$ . On the contrary,  $\gamma_{\text{Dynes}}$  plays a minor role in the reduction of  $\varepsilon_{\text{acc}}$  when  $n_g$  is close to the single-particle threshold.

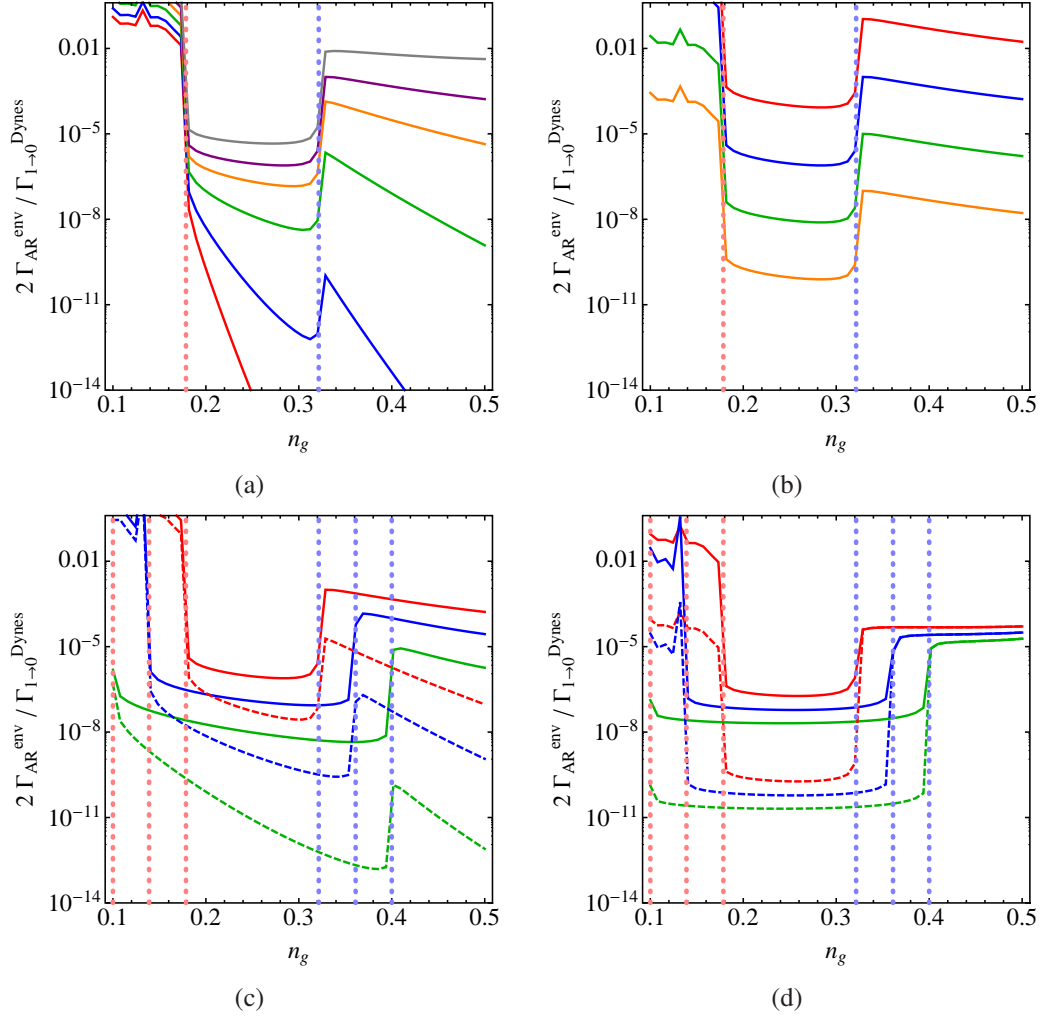


Figure 2.6: Plot of the ratio  $\varepsilon_{acc}$  as a function of the gate-induced charge  $n_g$  with  $\Delta = 210 \mu\text{eV}$  (Aluminum),  $R_T = 430 \text{ k}\Omega$ , and  $\mathcal{N} = 100$ . In panel (a), for each rate  $\gamma_{Dynes} = 10^{-5}$ ,  $R = 10 \Omega$  and  $E_C/\Delta = 1.4$ ; the values of  $T_{env}$  are: 70 mK (red), 140 mK (blue), 350 mK (green), 780 mK (orange), 1.5 K (purple), 4.2 K (gray). In panel (b), for each curve  $\gamma_{Dynes} = 10^{-5}$ ,  $T_{env} = 1.5$  K and  $E_C/\Delta = 1.4$ ; the resistances  $R$  are: 1100  $\Omega$  (red), 10  $\Omega$  (blue), 0.1  $\Omega$  (green), 0.001  $\Omega$  (orange). In panel (c), for fixed  $\gamma_{Dynes} = 10^{-5}$  and  $R = 10 \Omega$ , the curves with the same color are obtained using the same charging energy,  $E_C/\Delta$ : 1.4 (red lines), 1.8 (blue lines), 2.5 (green lines); the values of  $T_{env}$  are: 1.5 K (solid curves), and 500 mK (dashed curves). In panel (d), the Dynes parameter  $\gamma_{Dynes}$  is equal to  $10^{-4}$  (solid lines) and  $10^{-7}$  (dashed lines). The curves with the same color are obtained using the same charging energy,  $E_C/\Delta$ : 1.4 (red lines), 1.8 (blue lines), 2.5 (green lines). In all the four panels, the single- and two-particle thresholds,  $1/2 - \Delta/4E_C$  (light blue vertical dotted lines), and  $\Delta/4E_C$  (light red vertical dotted lines) respectively are also shown.

## 2.3 Conclusions

In this chapter, we studied the environment-assisted Cooper pair tunneling in a SINIS turnstile working in the Coulomb blockade regime. Specifically, we derived the Andreev reflection rate when only a photon of the thermal bath is involved in the process. We found that the single-photon absorption enhances the two-electron tunneling from N to S. In particular, the probability per unit of time to have Andreev events is different from zero even for values of the induced gate charge  $n_g$  close to the single-particle threshold  $1/2 - \Delta/4E_C$ . As a result, the single-electron current, which is expected to be the dominant one in the device when  $n_g$  follows the loop shown in Fig. 2.2(c), is also affected by the tunneling of Cooper pairs due to the environment. The influence of this source of error on the total current can be reduced by decreasing the effective resistance  $R$  and temperature  $T_{\text{env}}$  of the environment or, equivalently, the Dynes parameter  $\gamma_{\text{Dynes}}$ . The achievement of the metrological accuracy is also possible with the increasing of the charging energy  $E_C$  with respect to the superconducting energy gap  $\Delta$ .

However, the effect of the photon-assisted Andreev reflection can be relevant close to the single-particle threshold, although the error at the extreme points of the loop of Fig. 2.2(c) is below the value required by metrology. This means that the time spent by  $n_g(t)$  around  $1/2 - \Delta/4E_C$  while covering the optimal loop has to be as small as possible. As discussed in Ref. [36], the use of a square-wave signal to drive the gate voltage  $V_g(t)$  seems a promising solution for this problem.

On the basis of the results presented in Chapter 1, further reduction of the Andreev rate is expected when a zero-temperature and highly-resistive transmission line is inserted between the environment and the SINIS turnstile. Additional work is required in this direction.



# Design of an Efficient Superconducting Junctions-Based Cascade Electron Refrigerator

## Introduction

Electronic heat transport at the mesoscopic scale has been in the spotlight during the last few years [4]. In particular, efforts have been made to develop different types of solid-state electronic refrigerators based on superconducting tunnel junctions [44]. Unlike Peltier coolers which are typically used to decrease the temperature  $T$  of a certain object from room temperature,  $T \sim 300$  K, down to  $T \sim 170$  K [45], superconducting refrigerators can efficiently work in the cryogenic or subkelvin region,  $T < 1$  K [7]. On the other hand, thanks to their mesoscopic size, these superconducting devices allow to realize the cooling directly on the chip, thereby giving the possibility to avoid the use of relatively macroscopic and costly coolers like the traditional adiabatic-demagnetization and dilution refrigerators. As a result, they are suitable, for instance, to cool down the thin-film sensors of the calorimeters and bolometers used for astronomical observations, which typically require temperatures  $\sim 100$  mK and are embedded in space satellites, see Fig. 3.1(a).

Among the proposed devices since the first observation of the electronic cooling in the normal metal-insulator-superconductor (NIS) tunnel junction [7], the SINIS and  $S_2IS_1IS_2$  double-junction structures have been widely used for cooling microscopic as well as macroscopic objects, see Fig. 3.1 [8, 46–48]. Applying a voltage bias across these two devices, the hot electrons/quasiparticles can be extracted from the normal metal N or the small-gap superconductor  $S_1$  and injected into the outer superconductor S or the large-gap superconductor  $S_2$  respectively. Consequently, the electronic temperatures of N and  $S_1$  can become smaller than the bath temperature  $T_{\text{bath}}$  at which S and  $S_2$  are kept. In both cases, the energy

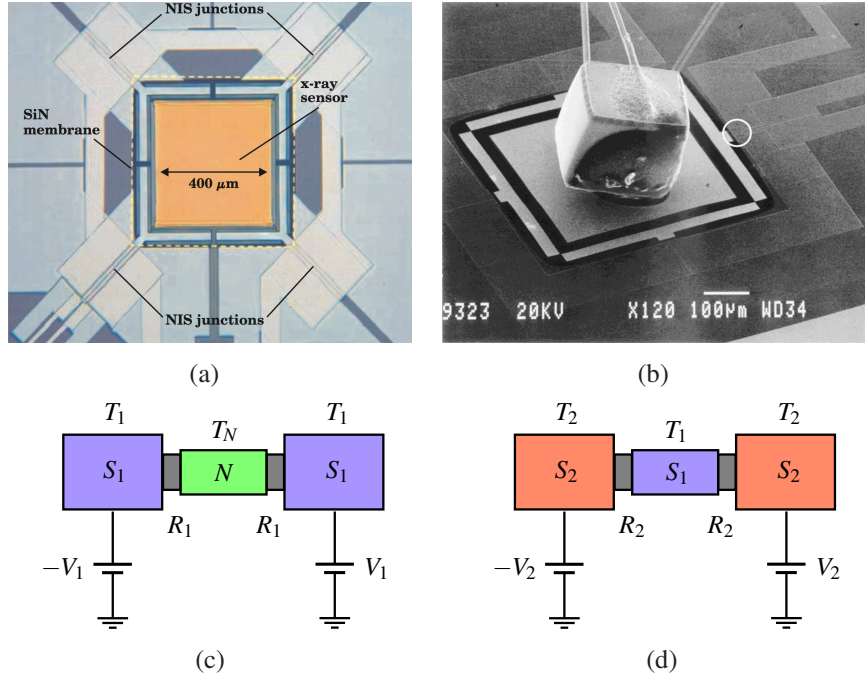


Figure 3.1: (a) Micrograph of a typical x-ray bolometer constituted by a squared thin bilayer of molybdenum and copper (sensor) supported by a silicon nitride membrane. Four “Y”-shaped fingers connects the membrane to four NIS refrigerators [49]. (b) Scanning electron microscope picture of a silicon nitride membrane cooled by four pairs of NIS refrigerators. One of them is indicated with a circle. A “cube” of neutron transmutation doped germanium is glued on top of the membrane and refrigerated [46]. (c) - (d) Sketch of a S<sub>1</sub>INIS<sub>1</sub> (c) and a S<sub>2</sub>IS<sub>1</sub>IS<sub>2</sub> (d) double junction refrigerators. The indicated quantities are the voltage biases ( $V_1$  and  $V_2$ ), the temperatures of the electrodes and of the central islands ( $T_1$ ,  $T_2$  and  $T_N$ ), and the tunnel resistances of the junctions ( $R_1$  and  $R_2$ ).

gap in the BCS density of states of the outer involved superconducting metals can make the cooling powers or heat currents  $\dot{Q}_{N1}$  and  $\dot{Q}_{12}$  of N and S<sub>1</sub> positive functions in a certain voltage range [4,8]. In other words, S and S<sub>2</sub> act as energy filters, allowing the efficient evacuation of the most energetic electrons from N and S<sub>1</sub>.

For a SINIS refrigerator, by exploiting aluminum (Al) as superconducting material (S) with critical temperature  $T_c \approx 1$  K and copper (Cu) as normal metal (N), the cooling of the electrons in N down to the temperature  $T_N \approx 100$  mK can be routinely achieved starting from  $T_{S,N} = T_{\text{bath}} = 300$  mK [8,44]. The decrease of the electronic temperature of a superconductor by quasiparticle tunneling in a S<sub>2</sub>IS<sub>1</sub>IS<sub>2</sub> configuration has also been demonstrated using aluminum (S<sub>2</sub>) and titanium (S<sub>1</sub>) [50]. In that case, a titanium strip with  $T_c \approx 510$  mK was cooled from

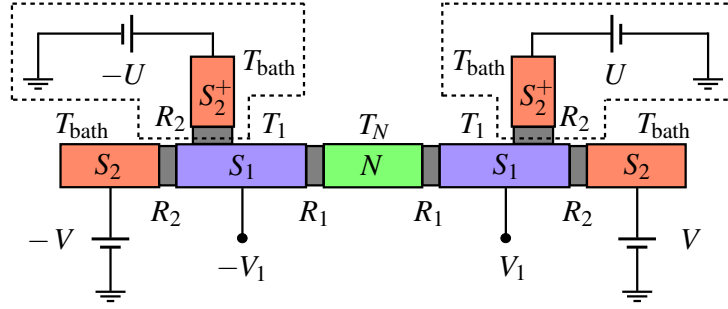


Figure 3.2: Sketch of the  $S_2IS_1INIS_1IS_2$  cascade cooler discussed in this chapter. The optional elements contained into the two dashed boxes enable to reach precisely the optimum bias in both the  $NIS_1$  and the  $S_2IS_1$  junctions.

$T_{\text{bath}} \approx 520$  mK to  $T_1 \approx 320$  mK. In order to operate over a wider temperature range, the use of alternative superconducting materials and/or architectures is required. For instance, a  $S_2IS_1IS_2$  nanorefrigerator based on vanadium (V) as outer superconductor with a critical temperature of about 4 K was used to efficiently cool down electrons in an Al island from 1 K to about 0.4 K [48]. On the basis of these experimental results, one may expect that a certain combination of the SINIS and  $S_2IS_1IS_2$  coolers should be capable to reach a temperature  $\sim 100$  mK when the initial one is 1 K.

In this chapter, we theoretically and numerically discuss the feasibility and performances of a multistage superconducting refrigerator, hereafter called *cascade cooler*, resulting from a sort of merging of the SINIS and  $S_2IS_1IS_2$  devices, arranged in a symmetric configuration, see Fig. 3.2. By using suitable materials and values of the involved parameters, we show that it is possible to cool down a normal metal island with improved performances with respect to more conventional SINIS refrigerators.

### 3.1 Superconducting electron refrigerators

We first discuss the behavior of the single  $NIS_1$  and  $S_2IS_1$  junctions constituting the cascade cooler of Fig. 3.2. Specifically, we focus on the cooling capabilities of the  $S_1INIS_1$  and  $S_2IS_1IS_2$  double-junction refrigerators sketched in Figs. 3.1(c) and 3.1(d).

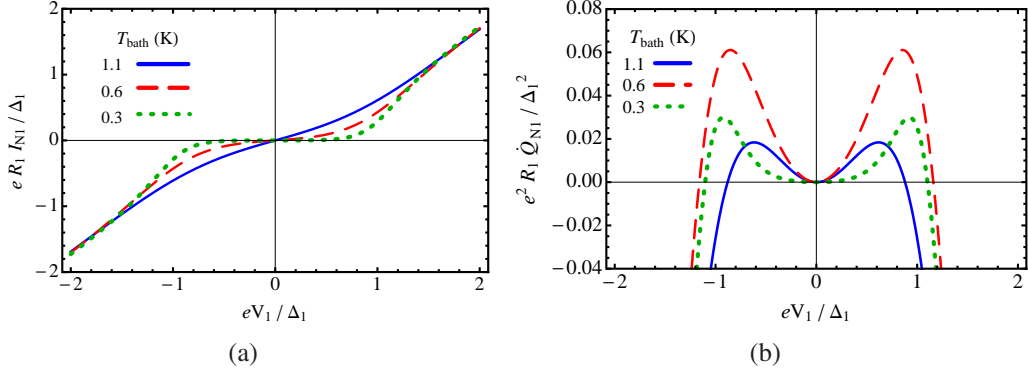


Figure 3.3: Dimensionless charge current  $eR_1 I_{N1}/\Delta_1$  (a) and cooling power  $e^2 R_1 \dot{Q}_{N1}/\Delta_1^2$  (b) of a NIS<sub>1</sub> junction, with resistance  $R_1$ , as a function of the dimensionless applied bias voltage  $eV_1/\Delta_1$ . The curves in (a) and (b) are obtained by the direct numerical integration of Eqs. (3.1) and (3.2) respectively using the following bath temperatures: 0.3 K (green dotted), 0.6 K (red dashed), and 1.1 K (blue solid). For both panels (a) and (b) the superconductor S<sub>1</sub> is aluminum with energy gap  $\Delta_1 = 200 \mu\text{eV}$ , and the Dynes parameter is  $\gamma_1 = 10^{-6}$ .

### 3.1.1 (SI)NIS cooler

The charge current  $I_{N1}$  and the heat current  $\dot{Q}_{N1}$  flowing from N to S<sub>1</sub> through a NIS<sub>1</sub> junction, biased with the voltage  $V_1$ , are given by [4]

$$I_{N1} = \frac{1}{eR_1} \int_{-\infty}^{+\infty} dE N_1(E - eV_1) [f_1(E - eV_1) - f_N(E)], \quad (3.1)$$

$$\dot{Q}_{N1} = \frac{1}{e^2 R_1} \int_{-\infty}^{+\infty} dE E N_1(E - eV_1) [f_N(E) - f_1(E - eV_1)]. \quad (3.2)$$

Here  $f_N = f_N(E, T_N)$ , and  $f_1 = f_1(E, T_1)$  are the quasiparticle energy distribution functions in N, and S<sub>1</sub> at temperatures  $T_N$  and  $T_1$  respectively. By assuming that the inelastic electron-electron interaction drives each individual part of the junction into a quasi-equilibrium regime, both  $f_N$  and  $f_1$  can be considered equal to the corresponding Fermi-Dirac distributions,  $f_{N,1} = [\exp(E/k_B T_{N,1}) + 1]^{-1}$ . The charge and heat currents  $I_{N1}$  and  $\dot{Q}_{N1}$  are also determined by the energy dependence of the function  $N_1(E)$ , i.e., the dimensionless density of states (DOS) of S<sub>1</sub>. For a realistic description of the NIS<sub>1</sub> junction,  $N_1(E)$  is given by the Bardeen-Cooper-Schrieffer (BCS) DOS smeared by the Dynes parameter  $\gamma_1$  [51],

$$N_1(E, T_1) = \left| \Re \left[ \frac{E + i \gamma_1 \Delta_1(T_1)}{\sqrt{[E + i \gamma_1 \Delta_1(T_1)]^2 - \Delta_1(T_1)^2}} \right] \right|, \quad (3.3)$$

where the energy gap  $\Delta_1$  of  $S_1$  is a function of  $T_1$ . A non-zero  $\gamma_1$  for  $S_1$  induces heating in N because of the available quasiparticle states inside the energy gap. In other words, the broadening of the BCS DOS given by the Dynes parameter limits the energy filtering provided by the energy gap of an ideal BCS superconductor. As a result, the cooling vanishes at an electron temperature  $T_N \simeq 2.5 T_c \gamma_1^{2/3}$ . In practice,  $\gamma_1$  ranges typically from  $10^{-2}$  to  $10^{-7}$  [16].

Figure 3.3 shows the voltage bias dependence of the charge and heat currents in a NIS<sub>1</sub> junction given by Eqs.(3.1) and (3.2). For subgap bias,  $|V_1| < \Delta_1/e$ , we see that the heat current  $\dot{Q}_{N1}$  is positive, meaning heat removal from N into  $S_1$ . At low temperatures,  $k_B T_{N,1} \ll \Delta_1$ , the maximum cooling power occurs when  $e|V_1| \simeq \Delta_1 - 0.66 k_B T_N$  [44, 52]. At this optimum value, the corresponding charge current reads

$$I_{N1,opt} \approx 0.48 \frac{\sqrt{k_B T_N \Delta_1}}{e R_1}. \quad (3.4)$$

As every tunneling event removes an energy of about  $k_B T_N$ , the related heat current  $\dot{Q}_{N1,opt}$  is about  $(I_{N1,opt}/e)k_B T_N$ . In general,  $\dot{Q}_{N1,opt}$  is a non-monotonic function of the bath temperature, and reaches its maximum value when  $T_{\text{bath}} \simeq 0.44 T_c$  [4]. On the other hand, when  $e|V_1| > \Delta_1$ , Eq. (3.2) becomes negative and the electrode N is heated with a power  $-\dot{Q}_{N1}$  close to  $IV_1/2$ . On the contrary, for any value of the bias voltage  $V_1$ , the superconductor  $S_1$  receives the heat  $-\dot{Q}_{1N} = IV_1 + \dot{Q}_{N1} > 0$ , with

$$\dot{Q}_{1N} = \frac{1}{e^2 R_1} \int_{-\infty}^{+\infty} dE (E - eV_1) N_1(E - eV_1) [f_1(E - eV_1) - f_N(E)],$$

which is lost in the bath.

From Fig. 3.3(b), we also see that the cooling power Eq. (3.2) is an even function of the applied bias voltage  $V_1$ . This means that both positive and negative values of  $V_1$  allow to remove, in the same way, the most energetic electrons which lie above the Fermi level. Such a symmetry of  $\dot{Q}_{N1}$  is a peculiar feature of the NIS<sub>1</sub> junction, and can be exploited in the symmetric S<sub>1</sub>INIS<sub>1</sub> device. Indeed, in the double-junction structure of Fig. 3.1(c), the heat can go out of the normal metal island through both junctions thereby increasing the cooling power, whereas the charge current can flow only in a well defined direction for a given  $V_1$ . As a result, the SINIS configuration is more efficient than a single NIS junction [8].

At the thermal equilibrium, the heat balance for the central island in the S<sub>1</sub>INIS<sub>1</sub> cooler is

$$2\dot{Q}_{N1} + P_{\text{e-ph}}^N = 0. \quad (3.5)$$

Here the factor 2 accounts for the fact that the heat is removed simultaneously through both junctions, see Fig. 3.1(c). In writing Eq. (3.5), we also take into

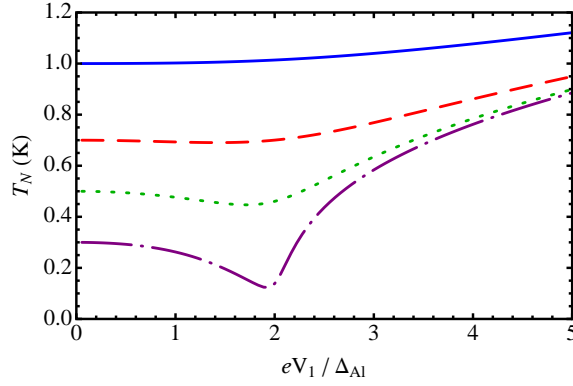


Figure 3.4: Calculated temperature  $T_N$  of the normal metal island for an Al-Cu SINIS refrigerator (see Fig. 3.1(c)) as a function of the dimensionless bias voltage  $eV_1/\Delta_{\text{Al}}$  for different values of the bath temperature  $T_{\text{bath}}$ : 1.0 K (solid blue), 0.7 K (dashed red), 0.5 K (dotted green), 0.3 K (dot-dashed purple). The values of the other parameters are [8]:  $\Delta_{\text{Al}} = 180 \mu\text{eV}$ ,  $R_1 = 1 \text{ k}\Omega$ ,  $\Sigma_{\text{Cu}} = 4 \times 10^9 \text{ Wm}^{-3}\text{K}^{-5}$ ,  $\Omega_{\text{Cu}} = 5.25 \times 10^{-2} \mu\text{m}^3$ , and  $\gamma_1 = 10^{-5}$ .

account the exchange of energy between the electrons and the phonons in N by introducing the power [53]

$$P_{\text{e-ph}}^{\text{N}} = \Sigma_{\text{N}} \Omega_{\text{N}} \left( T_{\text{N}}^5 - T_{\text{bath}}^5 \right), \quad (3.6)$$

where  $\Sigma_{\text{N}}$  and  $\Omega_{\text{N}}$  are the material-dependent electron-phonon coupling constant and the volume of the normal metal respectively. The energy rate Eq. (3.6) starts to be relevant as soon as  $T_{\text{N}} \neq T_{\text{bath}}$ . In particular, when  $T_{\text{N}} < T_{\text{bath}}$ ,<sup>1</sup>  $P_{\text{e-ph}}^{\text{N}}$  is negative, meaning that the phonons transfer energy to the electrons, thereby increasing their temperature  $T_{\text{N}}$  and reducing the cooling efficiency of the  $\text{S}_1\text{INIS}_1$  structure. In other words, the interplay between  $2\dot{Q}_{\text{N1}}$  and  $P_{\text{e-ph}}^{\text{N}}$  determines the smallest  $T_{\text{N}}$  that can be achieved. Keeping fixed the value of the parameters  $T_1 = T_{\text{bath}}$ ,  $\Delta_1$ ,  $\gamma_1$ ,  $R_1$ ,  $\Sigma_{\text{N}}$ ,  $\Omega_{\text{N}}$  and  $V_1$ , the integral equation (3.5) can be solved numerically and the temperature of the normal metal  $T_{\text{N}}$  obtained. Figure 3.4 shows the trend of the calculated  $T_{\text{N}}$  as a function of the bias voltage  $V_1$  for a  $\text{S}_1\text{INIS}_1$  refrigerator based on Al ( $\text{S}_1$ ) and Cu (N). Starting from  $V_1 = 0$ , we see that the temperature of the central island drops as  $V_1$  is increased, eventually reaching the minimum value  $T_{\text{N},\text{min}}$  when  $eV_1 \approx 2\Delta_{\text{Al}}$ .<sup>2</sup> The smallest temperature which can be achieved depends on  $T_{\text{bath}}$ . For instance, choosing the parameters of the system as in the experiment reported in Ref. [8], when  $T_{\text{bath}} = 1 \text{ K}$ , no cooling occurs, see Fig 3.4. On the contrary, the copper island reaches the temperature 123 mK while keeping

<sup>1</sup>this condition is typically satisfied when cooling occurs.

<sup>2</sup>the factor 2 is related to the presence of two junctions in the SINIS structure.

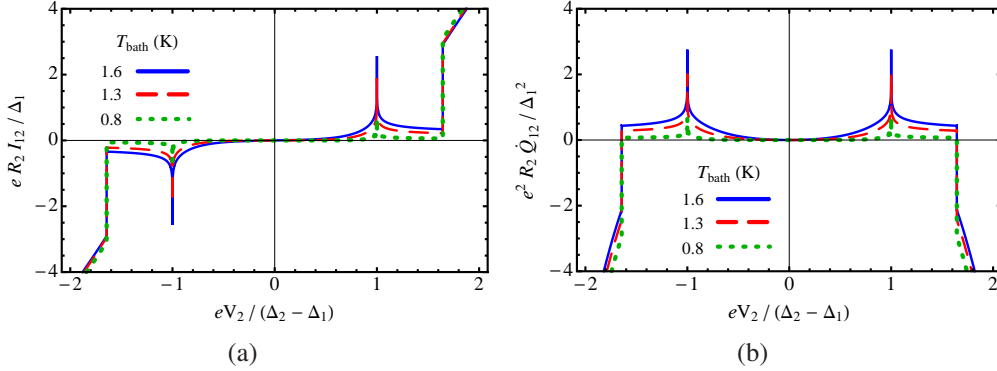


Figure 3.5: Dimensionless charge current  $eR_2I_{12}/\Delta_1$  (a) and cooling power  $e^2R_{1,2}\dot{Q}_{N1,12}/\Delta_1^2$  (b) of a  $S_1IS_2$  tunnel junction, with resistance  $R_2$ , as a function of the dimensionless applied bias voltage  $eV_2/(\Delta_2 - \Delta_1)$ . The curves in (a) and (b) are obtained by the direct numerical integration of Eq. (3.7) and (3.8) respectively using the following bath temperatures: 0.8 K (green dotted), 1.3 K (red dashed), and 1.6 K (blue solid). For both panels (a) and (b) the superconductor  $S_1$  is aluminum, with energy gap  $\Delta_1 \simeq 200 \mu\text{eV}$ , and the superconductor  $S_2$  is vanadium with energy gap  $\Delta_2 \simeq 821 \mu\text{eV}$ , i.e.,  $\Delta_2/\Delta_1$  is 4.105. The Dynes parameters are  $\gamma_{1,2} = 10^{-6}$ .

the aluminum electrodes at the bath temperature  $T_{\text{bath}} = 300 \text{ mK}$ . Biasing the  $S_1INIS_1$  cooler with a voltage higher than  $2\Delta_{\text{Al}}$ , the normal metal N heats and eventually overcomes  $T_{\text{bath}}$ .

### 3.1.2 (SI)SIS cooler

In a  $S_1IS_2$  junction biased with a voltage  $V_2$ , the charge current  $I_{12}$  and heat current  $\dot{Q}_{12}$  flowing from  $S_1$  to  $S_2$  can be written as [50, 54, 55]

$$I_{12} = \frac{1}{eR_2} \int_{-\infty}^{+\infty} dE N_1(E) N_2(E - eV_2) [f_2(E - eV_2) - f_1(E)], \quad (3.7)$$

$$\dot{Q}_{12} = \frac{1}{e^2R_2} \int_{-\infty}^{+\infty} dE E N_1(E) N_2(E - eV_2) [f_1(E) - f_2(E - eV_2)]. \quad (3.8)$$

Similarly to Eqs. (3.1) and (3.2), in the quasi-equilibrium regime,  $f_1 = f_1(E, T_1)$  and  $f_2 = f_2(E, T_2)$  are the Fermi-Dirac distribution functions of the electrons in  $S_1$  and  $S_2$  at temperatures  $T_1$  and  $T_2$  respectively. On the other hand, the DOSs  $N_1(E)$  and  $N_2(E)$  are given by Eq. (3.3) with energy gaps  $\Delta_{1,2}$  and Dynes parameters  $\gamma_{1,2}$  respectively. In Fig. 3.5, we show the trend of Eqs. (3.7) and (3.8) as a function of the applied bias voltage  $V_2$ . We note the sharp maximum occurring at the difference between the energy gaps,  $e|V_2| = \Delta_2 - \Delta_1$ . This peak shows up only

at non-zero temperatures and corresponds to electrons occupying states above the gap  $\Delta_1$  in  $S_1$  which tunnel to the empty states above the gap  $\Delta_2$  in  $S_2$ . Besides the dependence on temperature, the height of the peak is strongly affected by the Dynes parameters  $\gamma_{1,2}$  as well. Indeed, the DOSs  $N_{1,2}(E)$  in Eqs. (3.7) and (3.8) are  $\approx (2\sqrt{\gamma_{1,2}})^{-1}$  for energies  $E$  close to the superconducting gaps  $\Delta_{1,2}$ . In particular, we have calculated the charge current to be

$$I_{12,opt} \approx \frac{-\sqrt{\Delta_1\Delta_2}}{eR_2} e^{-\Delta_1/k_B T_1} \ln(\sqrt{\gamma_1} + \sqrt{\gamma_2}), \quad (3.9)$$

when  $e|V_2| = \Delta_2 - \Delta_1$  and under the condition  $\Delta_2/\Delta_1 > T_{\text{bath}}/T_1 > 1$ . The details of the derivation of Eq. (3.9) are in Appendix C. It is worth emphasizing that  $I_{12,opt}$  depends logarithmically on  $\gamma_1$  and  $\gamma_2$ . Compared to Eq. (3.4) which is valid for the NIS<sub>1</sub> case, the charge current Eq. (3.9) is smaller by a factor  $\sim \exp(-\Delta_1/k_B T_1)$ .<sup>3</sup> The related heat current is about  $\Delta_1(I_{12,opt}/e)$  (see Appendix C), meaning that every tunneling event removes a heat  $\Delta_1$  from  $S_1$ . This is the maximum amount of heat  $\dot{Q}_{12}$  that can be extracted from  $S_1$ .

In addition to the optimal value  $e|V_2| = \Delta_2 - \Delta_1$ , the heat current Eq. (3.8) is a positive function whenever  $e|V_2| < \Delta_2 + \Delta_1$  and negative otherwise, see Fig. 3.5(b). On the contrary, the energy current from  $S_2$  to  $S_1$ ,

$$\dot{Q}_{21} = \frac{1}{e^2 R_2} \int_{-\infty}^{+\infty} dE (E - eV_2) N_1(E) N_2(E - eV_2) [f_2(E - eV_2) - f_1(E)],$$

is always less than zero, i.e., the superconducting electrode  $S_2$  can not be cooled.

As for the NIS<sub>1</sub> case,  $\dot{Q}_{12}$  is a symmetric function of the bias voltage with respect to the vertical axes [see Fig. 3.5(b)]. Then the cooling power of  $S_1$  can be increased by means of the  $S_2$ IS<sub>1</sub>IS<sub>2</sub> double junction configuration depicted in Fig. 3.1(d). When this system reaches the thermal equilibrium, the heat balance for the inner superconductor  $S_1$  can be written as

$$2\dot{Q}_{12} + P_{\text{qp-ph}}^S = 0. \quad (3.10)$$

In this case, the quasi-particles in  $S_1$  exchange energy with the phonons of the

<sup>3</sup>note that the order of magnitude of Eq. (3.9) is determined by  $\exp(-\Delta_1/k_B T_1)$ . The latter can be much smaller than the logarithmic factor  $|\ln(\sqrt{\gamma_1} + \sqrt{\gamma_2})|$  if the parameters  $\gamma_{1,2}$ ,  $\Delta_1$  and  $T_1$  are equal to the values typically measured in real experiments. Indeed,  $|\ln(\sqrt{\gamma_1} + \sqrt{\gamma_2})|$  remains bound to  $\sim 1$  for  $10^{-7} \leq \gamma_{1,2} \leq 10^{-2}$ , whereas  $\exp(-\Delta_1/k_B T_1)$  ranges from  $10^{-4}$  to  $10^{-1}$  when  $S_1$  is aluminum,  $\Delta_{\text{Al}} = 200 \mu\text{eV}$ , and its temperature  $0.3 \text{ K} \leq T_{\text{Al}} \leq 1 \text{ K}$ .

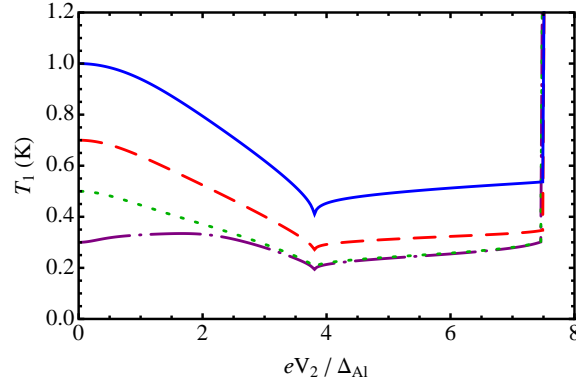


Figure 3.6: Calculated temperature  $T_1$  of the superconducting island  $S_1$  for a V-Al SISIS refrigerator (see Fig. 3.1(d)) as a function of the dimensionless bias voltage  $eV_2/\Delta_{Al}$  for different values of the bath temperature  $T_{\text{bath}}$ : 1.0 K (solid blue), 0.7 K (dashed red), 0.5 K (dotted green), 0.3 K (dot-dashed purple). The values of the other parameters are [48]:  $\Delta_{V/Al} = 580 \mu\text{eV}$ ,  $\Delta_{Al} = 200 \mu\text{eV}$ ,  $R_2 = 2 \text{ k}\Omega$ ,  $\Sigma_{Al} = 0.2 \times 10^9 \text{ Wm}^{-3}\text{K}^{-5}$ ,  $\Omega_{Al} = 1.08 \times 10^{-2} \mu\text{m}^3$ , and  $\gamma_2 = 10^{-5}$ .

lattice with the power [56]

$$\begin{aligned}
 P_{\text{qp-ph}}^S &= -\frac{\Sigma_S \Omega_S}{96 \zeta(5) k_B^5} \int_{-\infty}^{+\infty} dE E \int_{-\infty}^{+\infty} d\varepsilon \varepsilon^2 \text{sign}(\varepsilon) N_1(E) N_1(E + \varepsilon) \\
 &\times \left( 1 - \frac{\Delta_1^2(T_1)}{E(E + \varepsilon)} \right) \left\{ \coth\left(\frac{\varepsilon}{2k_B T_{\text{bath}}}\right) \left[ F_1(E) - F_1(E + \varepsilon) \right] \right. \\
 &\left. - F_1(E) F_1(E + \varepsilon) + 1 \right\}. \tag{3.11}
 \end{aligned}$$

Here  $\Sigma_S$  and  $\Omega_S$  are the material-dependent electron-phonon coupling constant and the volume of the superconductor  $S_1$  respectively. We also introduced the function  $F_1(\varepsilon) = f_1(-\varepsilon, T_1) - f_1(\varepsilon, T_1)$ . At  $T_{\text{bath}} \ll T_1 \ll \Delta/k_B$ , one obtains that the power exchanged between quasiparticles and phonons, Eq. (3.11), is reduced by a factor of  $0.98 \exp(-\Delta/k_B T_1)$  with respect to that of the normal state [56]. In other words, in a superconductor, the energy gap around the Fermi level suppresses the efficiency of the electron-phonon coupling.

Solving numerically the integral equation Eq. (3.10) for fixed values of the parameters  $T_2 = T_{\text{bath}}$ ,  $\Delta_{1,2}$ ,  $\gamma_{1,2}$ ,  $R_2$ ,  $\Sigma_S$ ,  $\Omega_S$  and  $V_2$ , one can obtain the temperature  $T_1$  of the inner superconductor  $S_1$  as a function of the applied bias voltage  $V_2$ . In Fig. (3.1.2), we plot the calculated  $T_1$  vs  $V_2$  for a  $S_2IS_1IS_2$  cooler based on V/Al ( $S_2$ ) and Al ( $S_1$ ) [48], for different bath temperatures. We see that  $T_1$  decreases upon increasing  $V_2$  and reaches its minimum value  $T_{1,\text{min}}$  when  $eV_2 \approx$

$2(\Delta_{V/Al} - \Delta_{Al})$ . Depending on  $T_{\text{bath}}$ , the smallest temperature  $T_{1,\text{min}}$  changes. In particular, considering  $T_{\text{bath}} = 1$  K, the inner superconductor can be cooled down to  $\approx 400$  mK, as it has been also verified experimentally [48].

## 3.2 Superconducting cascade electron refrigerator

### 3.2.1 System and thermal equilibrium equations

We consider now an electron cooler based on tunnel junctions arranged in a symmetric configuration, i.e.,  $S_2IS_1INIS_1IS_2$ , as displayed in Fig. 3.2. The structure includes two superconductors  $S_1$  and  $S_2$  with respective energy gaps  $\Delta_{1,2}$  so that  $\Delta_1 < \Delta_2$ .  $R_1$  and  $R_2$  denote the normal-state resistances of the individual  $S_1IN$  and  $S_2IS_1$  junctions, respectively. The present structure actually consists of a SINIS micro-cooler to which one superconducting tunnel contact has been added at each end. In the following, the cascade cooler  $S_2$  electrodes are voltage-biased at a voltage  $\pm V$ , so that the inner superconducting islands ( $S_1$ ) reach a voltage  $\pm V_1$ . Here, we also assume that inelastic electron-electron interaction drives each individual part of the system into a quasi-equilibrium regime. Therefore, the electron populations in  $N$  and  $S_1$  can be respectively described by a Fermi-Dirac energy distribution function at temperatures  $T_N$  and  $T_1$ , which can largely differ from the bath temperature  $T_{\text{bath}}$ . The outer superconductor  $S_2$  is considered at thermal equilibrium with the phonon bath so that  $T_2 = T_{\text{bath}}$ .

In the series configuration that we first consider, the charge currents flowing through all junctions are necessarily equal,

$$I_{N1} = I_{12}. \quad (3.12)$$

The thermal balance in  $N$  reads

$$2\dot{Q}_{N1} + P_{\text{e-ph}}^N = 0, \quad (3.13)$$

the factor 2 coming from the presence of two symmetric cooling NIS junctions. On the other hand, the thermal balance in each  $S_1$  reads

$$\dot{Q}_{12} + \dot{Q}_{1N} + P_{\text{qp-ph}}^S = 0, \quad (3.14)$$

where we have taken into account the heat  $-\dot{Q}_{1N} > 0$  deposited by the  $S_1IN$  junction into the superconductor 1. The behavior of the cascade cooler is governed by the above three non-linear integral equations. It depends strongly on different parameters such as the dimensionless Dynes parameters  $\gamma_{1,2}$ , the  $N$  and  $S_1$  volumes  $\mathcal{V}_{N,1}$ , the choice of the materials, the bath temperature, and the junction resistances  $R_{1,2}$ . As for the latter, it is crucial that the two cooling junctions  $NIS_1$

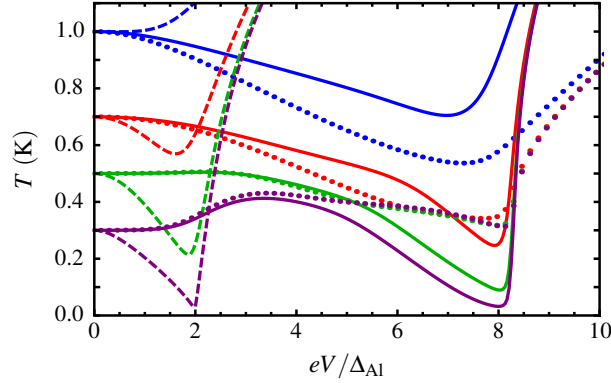


Figure 3.7: Calculated temperature of the normal metal,  $T_N$  (solid line), and of the superconductor  $S_1$ ,  $T_1$  (dotted lines), for a V-Al-Cu cascade cooler and for an Al-Cu SINIS refrigerator (dashed lines) as a function of  $eV/\Delta_{Al}$ , at a bath temperature  $T_{\text{bath}} = 1$  K (blue curves), 0.7 K (red), 0.5 K (green), and 0.3 K (purple). The parameters are  $\gamma_{1,2} = 10^{-5}$ ,  $R_1 = 500 \Omega$ ,  $R_1/R_2 = 100$ ,  $\mathcal{V}_1 = \mathcal{V}_N = 10^{-2} \mu\text{m}^3$ ,  $\Delta_{Al} = 200 \mu\text{eV}$ ,  $\Delta_V = 821 \mu\text{eV}$ ,  $\Sigma_{Al} = 0.2 \times 10^9 \text{ Wm}^{-3}\text{K}^{-5}$ , and  $\Sigma_{Cu} = 2 \times 10^9 \text{ Wm}^{-3}\text{K}^{-5}$ .

and  $S_1IS_2$  reach together their optimum cooling point at a given global bias  $V$ . A first naive assumption would be to assume that the currents at the optimum bias point are close to the Ohm's law value, so that the resistance balance would read  $(\Delta_2 - \Delta_1)/R_2 = \Delta_1/R_1$ . This is actually incorrect, as the current through the  $S_2IS_1$  junction is far from being Ohmic and depends strongly on the Dynes parameters.

In order to be more specific, let us consider as a first combination of materials vanadium, aluminum and copper. Based on its critical temperature of about 4 K, vanadium brings a good efficiency for electronic cooling from a bath temperature around 1 K [48]. An aluminum island cooled in this way can reach a temperature close to the operation range of usual aluminum-based SINIS coolers. A cascade combination of V-Al<sub>2</sub>O<sub>3</sub>-Al and Al-Al<sub>2</sub>O<sub>3</sub>-Cu junctions therefore seems promising. Figure 3.7 compares the behavior of a Al-Cu SINIS refrigerator (dashed lines) to a V-Al-Cu cascade cooler (solid lines) with usual parameters values, a common tunnel resistance  $R_1 = 500 \Omega$  and a resistance ratio  $R_1/R_2 = 100$ , close to the optimum (see below). From Fig. 2, the electronic cooling of the N island (full lines) is more efficient in the cascade system, which performs well up to 0.7 K, whereas the SINIS refrigerator (dashed lines) is little efficient. At a bath temperature of 1 K, the SIN stage is inefficient, while the SIS stage operates well. The capability of the cascade refrigeration scheme is illustrated by the large quasiparticle cooling obtained in  $S_1$  at every bath temperature below 1 K (dotted lines).

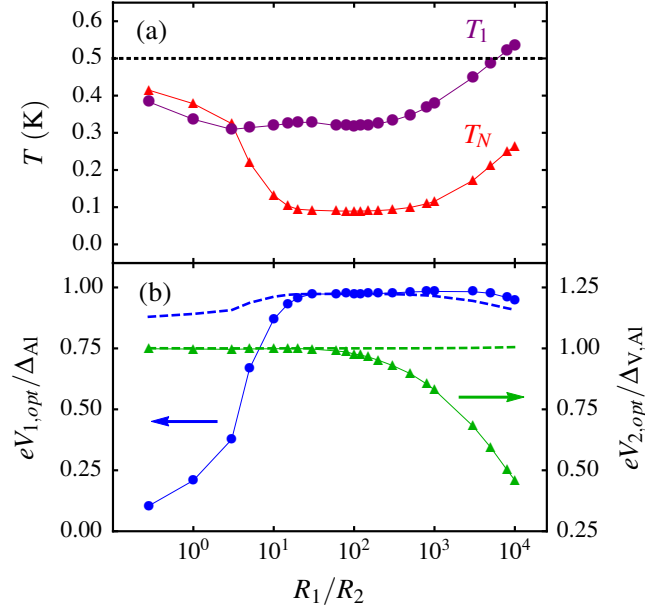


Figure 3.8: (a) Calculated minimum temperature of the normal metal  $T_{N,min}$  (red triangles) and the related temperature of low-gap superconductor  $T_1$  (purple disks) of a V-Al-Cu cascade cooler at its optimum bias point as a function of the ratio  $R_1/R_2$  for a bath temperature  $T_{\text{bath}} = 0.5$  K. (b) Related dimensionless voltage drops  $eV_{1,opt}/\Delta_{Al}$  (blue; left axis) and  $eV_{2,opt}/\Delta_{V,Al} = eV_{2,opt}/(\Delta_V - \Delta_{Al})$  (green; right axis) across the  $S_1IN$  and  $S_2IS_1$  junctions, respectively, as a function of  $R_1/R_2$ . The bath temperature considered here is 0.5 K. The other parameters are identical to the ones of Fig. 3.7. Also shown are the predictions  $eV_{1,opt} = \Delta_1(T_1) - 0.66 k_B T_N$  (dashed blue line) and  $eV_{2,opt} = \Delta_2(T_{\text{bath}}) - \Delta_1(T_1)$  (dashed green line).

### 3.2.2 The role of the tunnel resistance ratio

Still in the case of a V-Al-Cu device, Figure 3.8 displays the minimum achieved electronic temperature in N ( $T_N$ ) [panel (a)] and the voltage drops  $V_{1,opt}$  and  $V_{2,opt}$  [panel (b)] across the two  $S_1IN$  and  $S_2IS_1$  junctions at the minimum temperature  $T_N$  versus the junctions' resistance ratio  $R_1/R_2$ . A bath temperature  $T_{\text{bath}}$  of 0.5 K and a fixed resistance  $R_1$  of 500  $\Omega$  is considered here. At large  $R_1/R_2$  value, the  $S_1IN$  junctions dominate and the optimum cooling is obtained at a voltage drop  $V_1$  close to the expected value  $(\Delta_1 - 0.66 k_B T_N)/e$ . At small  $R_1/R_2$  value, it is the  $S_2IS_1$  junctions that dominate, and the optimum cooling is obtained at  $V_2$  close to the expectation  $(\Delta_2 - \Delta_1)/e$ . Overall, the best performance is obtained in the region where the two kinds of junctions can operate close to the optimum. Here, the parameters are  $\gamma_{1,2} = 10^{-5}$  and  $10^{-4}$  and  $\mathcal{V}_N = 10^{-2} \mu\text{m}^3$ . We have used

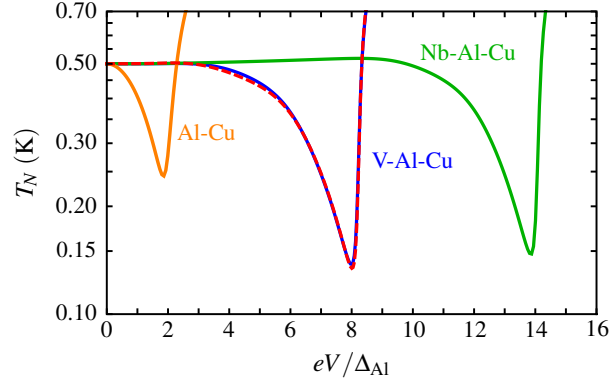


Figure 3.9: Calculated normal metal temperature  $T_N$  in a cascade cooler for  $T_{\text{bath}} = 0.5$  K as a function of the dimensionless bias voltage  $eV/\Delta_{\text{Al}}$ , in different cases: Al-Cu one-stage cooler (orange), V-Al-Cu (dotted red) with identical volumes for N and  $S_1$ , V-Al-Cu (blue) and Nb-Al-Cu (green) with volumes adapted to the resistances' ratio so that  $\mathcal{V}_1/\mathcal{V}_N = R_1/2R_2$ . The ratio  $R_1/R_2$  is set at the optimal value in every case: 100 (V-Al-Cu), 30 (Nb-Al-Cu), 80 (V-Al-Cu, adapted volumes' ratio) respectively. We use  $\Delta_{\text{Nb}} = 1407 \mu\text{eV}$ ,  $R_1 = 1 \text{ k}\Omega$ . The other parameters are identical to Fig. 3.7, including  $\mathcal{V}_N = 10^{-2} \mu\text{m}^3$ .

the well-accepted material-specific values  $\Sigma_{\text{Al}} = 0.2 \times 10^9 \text{ Wm}^{-3} \text{ K}^{-5}$  and  $\Sigma_{\text{Cu}} = 2 \times 10^9 \text{ Wm}^{-3} \text{ K}^{-5}$ . In this case, we achieve a good and somewhat constant performance for a resistance ratio between 10 and 200. This order of magnitude is consistent with the factor  $\exp(\Delta_1/k_B T_1)$  between the currents  $I_{N1,\text{opt}}$  and  $I_{12,\text{opt}}$  at an identical junction resistance  $R_{1,2}$ . The relatively large span of this region stems from the existence of the singularity in the electric current as a function of the bias voltage. This rectifies any imbalance that might occur in the structure, similarly to what happens for an asymmetric pair of NIS junctions in series [57]. At higher bath temperature, the window for optimal resistance ratio gets narrower, and is slightly shifted towards lower values.

Let us now discuss practical issues in a cascade cooler's design. As stated above, the performance of the cascade cooler configuration strongly depends on the value of the ratio  $R_1/R_2$ . Due to the smaller value of the current  $I_{12}$  through a  $S_1IS_2$  junction compared to the current  $I_{N1}$  through a  $S_1IN$  junction of comparable normal-state conductance, the resistance  $R_2$  has to be made significantly smaller than  $R_1$  in order to get an efficient cascade cooler. Optimal values of the  $R_1/R_2$  ratio for bath temperatures and material configurations of experimental interest therefore lie in the range  $\sim 15 - 150$ , while depending strongly on subtle parameters like the Dynes parameters of  $S_{1,2}$ . From the fabrication point of view, it might be difficult to tune the  $R_1/R_2$  ratio at its optimum with a good degree of

precision. This leads to the practical necessity of tuning the voltage  $V_1$  independently from the the main bias voltage  $V$ . One possible solution to this problem is to tunnel-couple to each  $S_1$  electrode an additional superconductor  $S'_2$ , as shown in Fig. 3.2. Biasing with a second positive (negative) voltage  $U$  these two tuning junctions would enable to add (subtract) some current in the  $S_1IS_2$  junctions compared to the  $S_1IN$  ones. The  $S_1INIS_1$  current can then be tuned from zero to the double of its value at zero bias  $U$ . The latter limitation comes from the fact that the voltage  $U$  needs to be always sub-gap in order to prevent any extra heating of the  $S_1$  electrode.

### 3.2.3 Different materials and volume ratios

For practical sample fabrication issues, one would preferably use the same tunnel barrier characteristics (in particular transparency) for the two tunnel barriers between  $S_1$  on one side, and  $N$  or  $S_2$  on the other side. Sticking to a particular value of the tunnel resistance ratio, and using similar thicknesses for  $N$  and  $S_1$ , thus leads to a volume ratio  $\mathcal{V}_1/\mathcal{V}_N$  between the superconductor  $S_1$  and the normal metal  $N$  approximately equal to half the inverse of the resistance ratio  $R_1/R_2$ . Furthermore, the values of the two superconductors' gaps can also be varied, for instance replacing vanadium with niobium (Nb). Figure 3.9 shows the results for the electron temperature  $T_N$  obtained with the two materials' choices V-Al-Cu, and Nb-Al-Cu, at  $T_{\text{bath}} = 0.5$  K, relating or not the volumes' ratio to the resistances' ratio. The optimal resistance ratios were adjusted in every case to, respectively, 30 for Nb-Al-Cu, 80 for V-Al-Cu when the volume ratio is adapted to the resistance ratio, and 100 for V-Al-Cu with identical volumes  $\mathcal{V}_1$  and  $\mathcal{V}_N$ . Imposing a larger volume  $\mathcal{V}_1$  affects only slightly the performance of the whole device, with a minimum electronic temperature rising from 134 to 138 mK for the V-Al-Cu material combination. This value increases to 147 mK when V is replaced by Nb. A larger gap value does not necessarily provide an improved cooling, because it also reduces the available heat current in the  $S_1IS_2$  junction.

### 3.2.4 Quasiparticle thermalization

Another crucial issue for the present cascade electronic cooler resides in a proper quasiparticle thermalization in the intermediate superconductor  $S_1$ . It is well known that superconducting-based electronic refrigerators generally suffer from poor evacuation of highly-energetic quasiparticles in the superconducting electrodes [58]. To this end, quasiparticle traps of various kinds have been envisaged in order to allow their evacuation into nearby-connected normal metal layers [59, 60]. In the present design, the outer superconductor  $S_2$  actually plays this role, with an increased efficiency thanks to its singularity in the density of states.

An incomplete quasiparticle energy relaxation in the superconductor  $S_1$  should actually not hinder the cooling in the low-gap superconductor  $S_1$  compared to the present quasi-equilibrium calculations. The cascade cooler appears as rather immune against poor electronic equilibration in  $S_1$ . Finally, the outer superconducting electrodes  $S_2$  can be efficiently thermalized through quasiparticles traps, just as it is done in the case of conventional superconducting refrigerators [4].

### 3.3 Conclusions

In conclusion, we have discussed a kind of electronic cooler based on hybrid superconducting tunnel junction, i.e., the  $S_2IS_1INIS_1IS_2$  cascade cooler. The cascade geometry allows to cool a first superconducting stage, which is used as a local thermal bath in a second stage. The correct operation of the device strongly depends on the matching between the resistances of the the two kinds of tunnel junctions. The resulting constraint can be easily implemented in a practical device, using of a set of two additional tunnel junctions. Decoupling of local phonon population from the thermal bath [61] in a suspended metal geometry [62] would improve performances compared to the situation considered here.



# Quantum Phase-Slip Junction Under Microwave Irradiation

## Introduction

The Josephson junction (JJ) is one of the most used superconducting devices in low-temperature condensed matter experiments. A single JJ is the building block of various sensors and electronic components [39, 63–66] and plays an important role in quantum computation and information [67–70]. On a more fundamental level, JJs with small capacitance have become paradigmatic systems for studying decoherence and dissipation of a quantum particle coupled to the external world and for analyzing the transition from quantum to classical states [41–43, 71–77].

Many of the JJ applications are based on the Josephson effect: a Cooper-pair tunneling current  $I_J$  can flow through a JJ in the absence of an applied bias voltage. The amplitude of this supercurrent is a non-linear function of the phase difference  $\varphi$  between the two superconductors of the junction,  $I_J = I_c \sin(\varphi)$ . The critical current  $I_c$  is the maximum Cooper pair current that can be carried by the junction. A voltage drop  $V_J = (\hbar/2e)d\varphi/dt$  appears across the junction when  $\varphi$  changes as a function of time. The classical dynamics of  $\varphi$  is ruled by the equations of motion for a fictitious particle moving in a tilted washboard potential. In particular, a phase-locking effect can occur when the JJ is irradiated with microwaves of frequency  $\omega_{\text{mw}}$  [78]. Then the so-called Shapiro steps of constant voltage  $V_{J,m} = m(\hbar/2e)\omega_{\text{mw}}$ , with  $m$  integer, appear in the current-voltage characteristic in addition to the zero-voltage supercurrent state [79, 80]. These steps are related only to the fundamental constants of physics (the Planck constant  $\hbar$  and the electron charge  $e$ ) and are used in metrology to define the quantum voltage standard [26, 81–83]. The necessary metrological accuracy is reached at low temperatures and using junctions with large Josephson energy  $E_J = \Phi_0 I_c / (2\pi) \sim 100$  meV ( $\Phi_0 = h/(2e)$  is the superconducting flux quantum) and small charging energy  $E_C = e^2/2C \sim 10$  neV, where the capacitance of the junction  $C$  plays the role of

the inertial mass in the dynamics of the phase. Moreover, the JJ is typically embedded in a circuit whose resistance  $R \lesssim R_Q$ , with  $R_Q = h/(4e^2) = 6.45 \text{ k}\Omega$  the superconducting resistance quantum. Under these conditions, thermal and quantum fluctuations of the phase  $\varphi$  are suppressed efficiently [78, 84].

The Josephson junction has an exact dual counterpart, the so-called quantum phase-slip junction (QPSJ) [85–93]. Physical realizations of QPSJ that have been discussed in the literature are a single Josephson junction with a finite capacitance [85–88, 93] or a linear chain of such Josephson junctions [93–97], and a narrow superconducting nanowire [98–104]. With respect to an ordinary JJ, the role of the phase and the charge in a QPSJ is interchanged. Specifically, Cooper-pair tunneling is replaced by its dual process, i.e., the slippage by  $2\pi$  of the phase difference between two well-defined superconducting regions of the device. As a consequence, the relations governing the behavior of a QPSJ are exactly dual to the usual Josephson relations. The voltage  $V_J = V_c \sin(\pi q/e)$  across the QPSJ is a non-linear function of the charge variable  $q$ , where the critical value  $V_c$  is the maximum voltage that the junction can sustain. The Cooper-pair current  $I_J = dq/dt$  is different from zero only for time-dependent  $q$ . As a consequence, under microwave irradiation, a QPSJ should sustain a set of current steps, i.e., the dual Shapiro steps  $I_{J,m} = me\omega_{\text{mw}}/\pi$ .

However, experimental evidence for the existence of dual steps has been elusive so far. Indeed, the dual Josephson relations pertain to a QPSJ with a relatively well defined charge  $q$ , achieved when phase-slips are produced at an appreciable rate, a condition which is not easily compatible with the existence of a well-defined underlying superconducting state. Actual realizations of a QPSJ are typically operated in a regime where  $V_c$  is not large, so that charge fluctuations are important, and may well mask the dual Shapiro steps.

In this chapter, we study the role of both thermal and quantum fluctuations of charge on the properties of the dual Shapiro steps. We present the results of a combined analytical and numerical analysis of a QPSJ irradiated with microwaves and embedded in a resistive ( $R$ ) and inductive ( $L$ ) electromagnetic environment. We will see, in particular, that an important role is played by the inductance  $L$ , the quantity dual to the capacitance  $C$  of a usual Josephson junction. By duality, we expect that the fluctuations of the charge  $q$  are governed by the ratio  $U_0/E_L$  of the characteristic phase-slip energy  $U_0 = 2eV_c/(2\pi)$ , dual to the Josephson coupling energy  $E_J$ , and the inductive energy  $E_L = \Phi_0^2/(2L)$ , dual to the charging energy  $E_C$  of a Josephson junction [91]. The larger  $L$ , the smaller  $E_L$  and the larger the ratio  $U_0/E_L$ , thus favoring a well-defined charge state of the QPSJ. Recent experiments on nanowires [101, 104] and chains of Josephson junctions [97] typically achieve  $U_0/E_L$  ratios that are of the order of  $10^{-2} \div 10^{-1}$ . We will analyze the microwave response of a QPSJ in this regime in detail and study in particular the resolution and accuracy of the dual Shapiro steps.

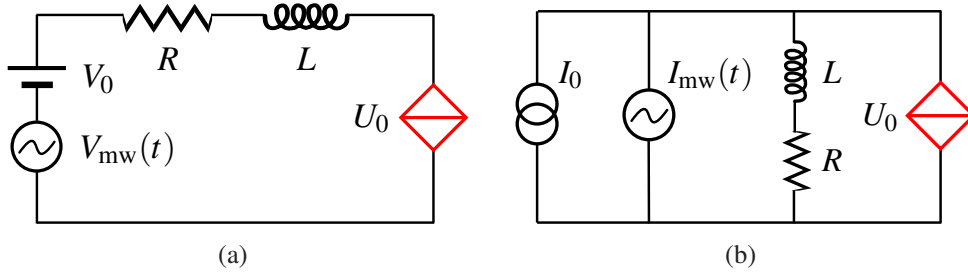


Figure 4.1: (a) Circuit of a voltage-biased QPSJ with phase-slip energy  $U_0 = eV_c/\pi$  in series with a resistance  $R$  and an inductance  $L$ . The voltage source has a DC component  $V_0$  and an AC one  $V_{mw}(t)$ . (b) Circuit of a current-biased QPSJ embedded in a resistive ( $R$ ) and inductive ( $L$ ) electromagnetic environment. The total bias current is the sum of a DC component  $I_0$  and an AC one  $I_{mw}(t)$ . This circuit is related to the voltage-biased one in (a) by the Thévenin-Norton theorem setting  $I_0 = V_0/R$  and  $|I_{mw}| = |V_{mw}|/\sqrt{R^2 + L^2\omega_{mw}^2}$  (see Appendix D).

## 4.1 Qualitative discussion of the main results

The observation of the dual Shapiro steps is expected in the current-voltage characteristic ( $I_J$ - $V_J$ ) of a voltage-biased QPS junction in series with an inductance  $L$  and an impedance  $Z(\omega)$  [91], which hereafter we assume to be frequency independent, i.e.,  $Z(\omega) = R$  [see Fig. 4.1(a)]. However, in this chapter, we will focus on the equivalent current-biased circuit shown in Fig. 4.1(b) where a QPSJ is connected in parallel to a resistive ( $R$ ) and an inductive ( $L$ ) electromagnetic environment and is driven by both a DC current source,  $I_0$ , and an AC one  $I_{mw}(t) = I_{mw} \cos \omega_{mw}t$  with amplitude  $I_{mw}$  and microwave frequency  $\omega_{mw}$ . The equivalence between the two circuits in Fig. 4.1 is provided by the Thévenin-Norton theorem, as shown in Appendix D. The results for the  $I_J$ - $V_J$  curve of the QPSJ of Fig. 4.1(b) that will be discussed in the following are independent of the specific choice of the external bias.

Let us first discuss the case when the environment is absent,  $R \rightarrow \infty$ , in the circuit of Fig. 4.1(b).<sup>1</sup> Then the dual Josephson relations describing the current-biased QPSJ can be straightforwardly integrated. Indeed, from the relation  $dq/dt = I_J = I_0 + I_{mw}(t)$ , we obtain  $q(t) = q_0 + I_0t + (I_{mw}/\omega_{mw}) \sin \omega_{mw}t$ , where  $q_0$  is the charge on the QPSJ at time  $t = 0$ . Substituting this result into the second relation,

<sup>1</sup>considering this limit in the voltage-biased circuit shown in Fig.4.1(a) leads to an effective current-biased QPSJ.

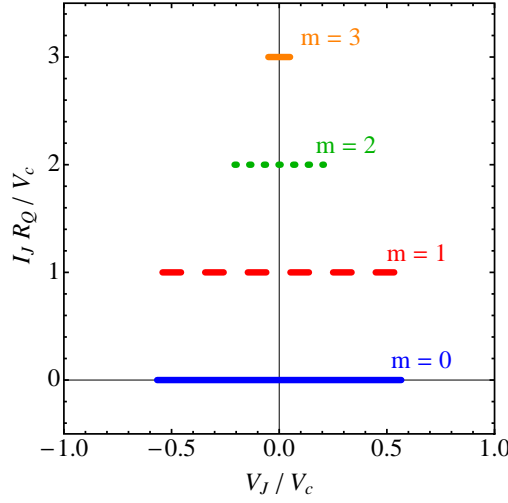


Figure 4.2: Dual Shapiro steps corresponding to  $m = 0, 1, 2,$  and  $3$  for a QPSJ in the absence of environment. The other parameters are:  $\alpha = 1.4$  and  $\hbar\omega_{\text{mw}}/2\pi U_0 = 1$ .

$V_J = V_c \sin(\pi q/e)$ , we find

$$V_J^{(\text{mw})}(\omega_B) = V_c \sum_{m=-\infty}^{+\infty} J_m(\alpha) \sin(\chi_0 + \omega_B t + m\omega_{\text{mw}} t), \quad (4.1)$$

where  $J_m$  is a Bessel function of the first kind. We defined the parameters  $\alpha = \pi I_{\text{mw}}/(e\omega_{\text{mw}})$  and  $\omega_B = \pi I_0/e$  as well as the dimensionless charge  $\chi_0 = \pi q_0/e$ . From this result we see that whenever  $\omega_B = m\omega_{\text{mw}}$ , the QPSJ will sustain a charge-dependent DC voltage  $V_{J,m} = V_c J_m(\alpha) \sin \chi_0$ . In other words, whenever the DC bias current  $I_0$  equals  $me\omega_{\text{mw}}/\pi$ , phase-locking occurs, which leads to the appearance of a dual Shapiro step, located at  $I_{J,m} = me\omega_{\text{mw}}/\pi$  in the DC current-voltage characteristic of the QPSJ. The width of this step in voltage  $V_J$  is given by  $2V_c J_m(\alpha)$ . Note that the parameter  $\alpha$  acts as the microwave coupling strength: the effect of the microwaves disappears as  $\alpha \rightarrow 0$ . Figure 4.2 shows the dual Shapiro steps corresponding to  $m = 0, 1, 2, 3$  for moderate microwave intensity,  $\alpha = 1.4$ , and microwave frequency  $\hbar\omega_{\text{mw}}/2\pi U_0 = 1$ .

We next turn to the case when the resistance  $R$  of the environment is finite. In this case, the total current  $I_J$  will contain two additional components. The first is the current flowing through the resistive-inductive branch of the circuit; it equals  $I_{RL}(t) = \int dt' Y(t-t') V_J(t')$ , where  $V_J(t) = V_c \sin[\pi q(t)/e]$  and  $Y(t)$  is the inverse Fourier transform of the admittance

$$Y(\omega) = 1/(R - i\omega L), \quad (4.2)$$

of the branch. The second component is a fluctuating current  $\delta I(t)$  of zero average and the Fourier components of which satisfy the fluctuation-dissipation theorem

$$\langle \delta I(\omega) \delta I(\omega') \rangle = 2\pi \delta(\omega + \omega') \hbar \omega \Re[Y(\omega)] \coth\left(\frac{\hbar \omega}{2k_B T}\right), \quad (4.3)$$

where  $T$  is the temperature of the environment. As a result the charge  $q$  on the QPSJ satisfies the Langevin equation

$$dq/dt = I_0 + I_{\text{mw}}(t) - I_{\text{RL}}(t) + \delta I(t). \quad (4.4)$$

In particular, the charge acquires a fluctuating component that will affect the shape of the current-voltage characteristic.

The effect of charge fluctuations as described by Eq. (4.4) has been analyzed in detail before in the case where microwaves are absent [85, 88, 92]. When  $I_{\text{mw}} = 0$ , Eq. (4.4) reduces to the well-known Langevin problem of the quasi-charge dynamics in the overdamped regime. The DC current-voltage characteristic of such a junction has been calculated before in various limits; we briefly recall some of the results here, focusing on the experimentally relevant limit  $U_0/E_L < 1$ , see also Fig. 4.3.

Let us first neglect the fluctuating component,  $\delta I(t) = 0$ . As long as the resistance  $R$  is large but finite, so that the dimensionless conductance of the environment, defined as  $g = R_Q/R$ , is still small, the DC current-voltage characteristic of the QPSJ is a so-called Bloch nose, in the absence of microwaves. It consists of a zero-current branch at finite voltage up to  $V_c$ , which bends back to a low-voltage, finite current branch. Setting  $\delta I = 0$  and considering the limit  $gU_0/E_L \ll 1$ , Eq. (4.4) can be integrated directly [92] to yield the DC voltage

$$V_J^{(\delta I=0)} = \frac{R_Q I_0}{g} - \theta\left(\frac{R_Q I_0}{g} - V_c\right) \sqrt{\left(\frac{R_Q I_0}{g}\right)^2 - V_c^2}, \quad (4.5)$$

where  $\theta(V)$  is the Heaviside step function. The corresponding current-voltage characteristic is shown in the inset of Fig. 4.3.

However, finite charge fluctuations,  $\delta I(t) \neq 0$ , prevent the formation of a sharp feature in the I-V characteristic, even for small  $g$ : they give rise to a finite slope at low current and reduce the maximum voltage to a value lower than  $V_c$ , thus smearing the corresponding current-voltage characteristic. When the resistance  $R$  is reduced further so that  $g > 1$ , the effect of the environment is stronger. The Bloch nose is smeared into a smooth curve with a maximum voltage at finite current. For very large values of  $g$ , the current  $I_J$  at which the QPSJ sustains the largest voltage approaches the value  $\Phi_0/2L$ . This phenomenon is dual to the phenomenon of Coulomb blockade found in a Josephson junction in a highly

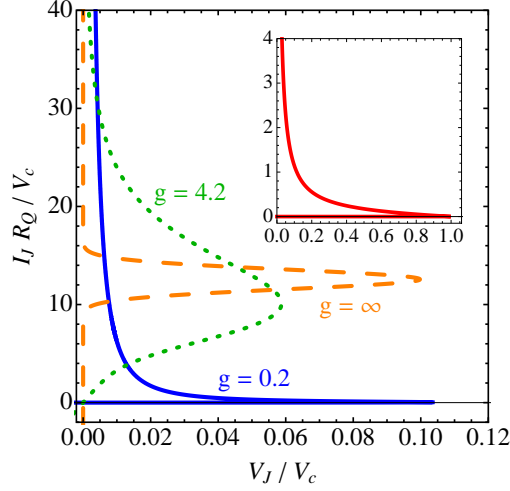


Figure 4.3: Low-temperature current-voltage characteristics,  $k_B T / U_0 = 0.25$ , of a QPSJ with  $U_0 / E_L = 0.013$ , embedded in an inductive-resistive environment in the absence of microwaves. Curves from bottom to top correspond to  $g = 0.2$ , 4.2, and  $\infty$ . The inset shows the case without fluctuations.

resistive environment, where the voltage at which the Josephson junction sustains the largest current approaches the value  $2e/2C$ .

We summarize this behavior in the main panel of Fig. 4.3 where we plotted the QPSJ's current-voltage characteristic for various values of  $g$  at low temperature,  $k_B T / U_0 = 0.25$ , and for small  $U_0 / E_L = 0.013$ . We stress that the behavior shown in Fig. 4.3 is essentially nonperturbative in the coupling strength  $g$  characterizing the environment. Indeed, it is well-known that perturbation theory in either  $g$  or  $1/g$  is plagued by divergences and describes at best only parts of the current-voltage characteristic. The complete current-voltage characteristic can only be obtained including the relevant contributions to all orders.

We are now in a position to state the main results of this chapter, where we study the combined effect of the application of microwaves and the presence of charge fluctuations induced by the resistive-inductive environment. We use an approach that is non-perturbative in both the environmental coupling strength  $g$  and the microwave coupling strength  $\alpha$ . As we will see below, this implies that analytical results can only be obtained in the limit  $U_0 / E_L < 1$ . On the other hand, this corresponds to the relevant experimental situation where QPSJs are studied with relatively low phase-slip rates and not too large inductances. In the limit  $U_0 / E_L < 1$ , we find that, at the first order in  $U_0$ , the QPSJ's current-voltage characteristic in the presence of microwaves can be straightforwardly obtained

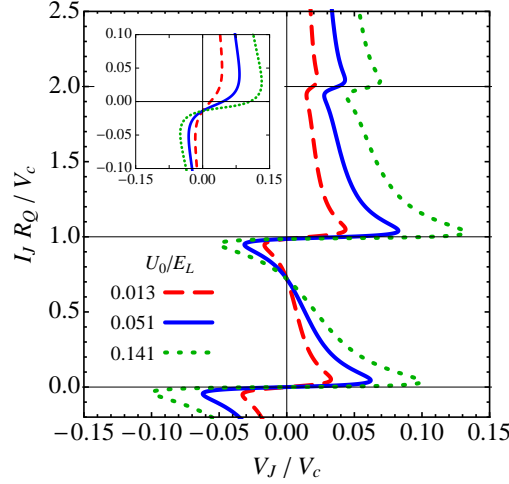


Figure 4.4:  $I_J$ - $V_J$  characteristic obtained from the numerical evaluation of Eq. (4.38) in the low-conductive regime,  $g = 0.2$ . Here,  $k_B T/U_0 = 0.25$  and  $\alpha = 1.4$ . The dimensionless frequency of the microwaves  $\hbar\omega_{\text{mw}}/2\pi U_0$  is equal to 1. The three curves are obtained using three different values of the inductance of the environment such that  $U_0/E_L = 0.013$  (red dashed line),  $U_0/E_L = 0.051$  (blue solid line),  $U_0/E_L = 0.141$  (green dotted line). The inset shows the relative deviation  $\delta I_m = \pi I_J / me\omega_{\text{mw}} - 1$  for the first Shapiro step,  $m = 1$ .

from the DC result without microwaves,

$$V_J^{(\text{mw})}(\omega_B) = \sum_{m=-\infty}^{+\infty} J_m^2(\alpha) V_J^{(\text{DC})}(\omega_B + m\omega_{\text{mw}}), \quad (4.6)$$

in agreement with a general result recently demonstrated in Ref. [105]. Here  $V_J^{(\text{DC})}$  is given by Eqs. (4.32) and (4.33). Specifically, this result implies that the current-voltage characteristic of a QPSJ with  $U_0/E_L < 1$  under microwave irradiation is obtained by replicating the known, DC characteristic of the QPSJ in the absence of microwaves at the positions of the current plateaus,  $I_{J,m} = me\omega_{\text{mw}}/\pi$ , which are expected for a QPSJ in the absence of the external electro-magnetic environment.

We focus on the case  $g < 1$ , for which dual Shapiro steps are expected. Figure 4.4 displays a typical current-voltage characteristic obtained in this situation, taking again  $g = 0.2$ ,  $k_B T/U_0 = 0.25$ , a microwave frequency  $\hbar\omega_{\text{mw}}/2\pi U_0 = 1$  and  $\alpha = 1.4$ . We see that the current-voltage characteristics are strongly modified in the simultaneous presence of microwaves and charge fluctuations induced by the environment, combining features of both Fig. 4.2 and 4.3.

Rather than being a set of discrete steps, the current-voltage characteristic is a continuous curve, connecting subsequent steps, bending back towards a zero-voltage state in between them. In other words, in the presence of microwaves,

a replica of the Bloch nose is indeed found for each dual Shapiro step. As expected, in the presence of charge fluctuations, the width of the steps is smaller than the value  $2V_c J_n(\alpha)$ , found for  $g = 0$ ; also, the dual steps are no longer strictly horizontal but acquire a small but finite linear slope. Note the role played by the inductance  $L$ , which limits the effects of the charge fluctuations. As is clearly seen in Fig. 4.4, the larger  $L$ , the larger the width of the steps and the smaller their slopes. This can be seen in particular in the inset of Fig. 4.4, which presents the relative accuracy  $\delta I_m = \pi I_J / m e \omega_{\text{mw}} - 1$  for the first Shapiro step,  $m = 1$ . The inset also shows that the accuracy of the dual step is not only limited by charge fluctuations but also by a systematic shift of the step position, down by about 0.0015 in relative accuracy. This is due to the finite overlap of the various replicas. The shift can be reduced by increasing the microwave frequency so that the replicas are more separated along the  $I_J$ -axis, thus reducing their overlap.

## 4.2 Current-biased QPSJ

### 4.2.1 QPSJ Hamiltonian

The Hamiltonian of the current-biased QPSJ in the circuit depicted in Fig. 4.1(b) is given by

$$\hat{H} = -U_0 \cos \left[ \frac{\pi}{e} (\hat{q} + \hat{Q}_{RL}) \right] - \frac{\hbar I(t)}{2e} \hat{\phi} + \hat{H}_{\text{env}} [\{\hat{Q}_\lambda\}, \{\hat{\phi}_\lambda\}], \quad (4.7)$$

(see Appendix D). Here the charge and phase operators  $\hat{q}$  and  $\hat{\phi}$  are canonically conjugate, satisfying the commutation relation  $[\hat{\phi}, \hat{q}] = 2ie$ . As a consequence,  $\hat{q}$  satisfies the equation of motion  $\dot{\hat{q}} = I(t)$  and thus corresponds to the total charge injected into the parallel combination of the QPSJ and the  $L - R$  environment. The first term in Eq. (4.7) describes the nonlinear QPSJ with phase-slip energy  $U_0$ , which carries the charge  $\hat{q} + \hat{Q}_{RL}$ , where the charge variable  $\hat{Q}_{RL} = \sum_\lambda \hat{Q}_\lambda$  accounts for the charge of the dissipative  $R$ - $L$  environment. We thus model it using an infinite ensemble of harmonic oscillators (Caldeira-Leggett model) [41, 42], described by the third term of Hamiltonian (4.7),

$$\hat{H}_{\text{env}} = \hat{H}_{\text{env}} [\{\hat{Q}_\lambda\}, \{\hat{\phi}_\lambda\}] = \sum_{\lambda=1}^{+\infty} \left[ \frac{\hat{Q}_\lambda^2}{2C_\lambda} + \frac{1}{2L_\lambda} \left( \frac{\hbar \hat{\phi}_\lambda}{2e} \right)^2 \right]. \quad (4.8)$$

The charge  $\hat{Q}_\lambda$  and the phase  $\hat{\phi}_\lambda$  represent the momentum and position, respectively, of the  $\lambda$ -oscillator with characteristic frequency  $\omega_\lambda = 1/\sqrt{L_\lambda C_\lambda}$ . According to the fluctuation-dissipation theorem,

$$\frac{1}{2} \langle [\hat{I}_{RL}(t), \hat{I}_{RL}(0)]_+ \rangle_\omega = \hbar \omega \Re[Y(\omega)] \coth \left( \frac{\hbar \omega}{2k_B T} \right),$$

where  $\hat{I}_{RL} = \hat{Q}_{RL}$  is the fluctuating current in the  $R$ - $L$  environment and  $[\dots, \dots]_+$  denotes the anticommutator. This yields the relation

$$\Re[Y(\omega)] = \pi\omega^2 \sum_{\lambda} \sqrt{\frac{C_{\lambda}}{L_{\lambda}}} \delta(\omega^2 - \omega_{\lambda}^2), \quad (4.9)$$

linking the parameters of the Caldeira-Leggett bath with the environmental admittance. Finally, the coupling between the charge operator  $\hat{q}$  and the bias current  $I(t)$  is given by the second term in (4.7).

Hamiltonian (4.7) has been used to describe QPSJs based on nanowires [91], Josephson junctions [92] and chains of Josephson junctions [93]. In Appendix D, we show how Hamiltonian (4.7) can be obtained starting from the well-known Hamiltonian of a current-biased single Josephson junction embedded in an  $R$ - $L$  environment.

## 4.2.2 Current-voltage characteristic

The DC current  $I_J$  flowing through the QPSJ element is given by the difference between the total DC current  $I_0$  and the current flowing through the  $R$ - $L$  impedance of the circuit of Fig. 4.1(b),

$$I_J = I_0 - V_J/R. \quad (4.10)$$

Here  $V_J$  is the DC component of the voltage drop across the QPSJ element. Using the Josephson relation between  $\hat{\phi}$  and  $V_J$  and the Heisenberg equation of motion for the operator  $\hat{\phi}$  generated by the Hamiltonian  $\hat{H}$ , this potential reads (see Appendix D)

$$V_J = \frac{\hbar}{2e} \left\langle \frac{d\hat{\phi}}{dt} \right\rangle_{\text{DC}} = V_c \left\langle \sin \left[ \frac{\pi}{e} (\hat{q} + \hat{Q}_{RL}) \right] \right\rangle_{\text{DC}}. \quad (4.11)$$

The symbol  $\langle \dots \rangle$  denotes the quantum statistical average for the system described by the Hamiltonian  $\hat{H}$ , Eq. (4.7).

### Dual Shapiro steps in the absence of environment

By setting  $\hat{Q}_{RL} = 0$  in Eq. (4.7), the coupling with the environment vanishes and the system corresponds to an ideal current-biased QPSJ whose Hamiltonian  $\hat{H}_0$  contains only the first two terms of  $\hat{H}$ . Introducing a complete set of discrete phase-states for the QPSJ,  $|\phi_n\rangle = 2\pi|n\rangle$  with  $n$  integer, we can express  $\hat{H}_0$  as

$$\hat{H}_0 = -\frac{U_0}{2} \sum_n (|n\rangle \langle n+1| + \text{h.c.}) - \frac{\hbar I(t)}{2e} \sum_n 2\pi n |n\rangle \langle n|. \quad (4.12)$$

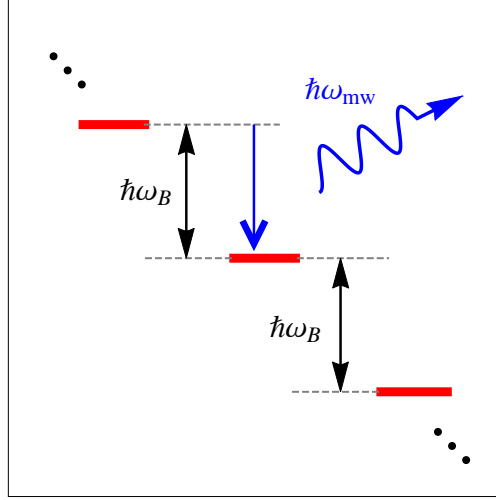


Figure 4.5: Wannier-Stark ladder. The tilt provided by the bias current  $I_0$  induces an energy separation  $\hbar\omega_B$  between adjacent phase states indicated by red horizontal bars. Phase-locking occurs when the resonant condition  $\omega_B = m\omega_{mw}$  is satisfied. For  $m = 1$ , a photon with energy  $\hbar\omega_{mw}$  is exchanged with the microwave source.

in the phase representation. When  $I_{mw} = 0$ , Eq. (4.12) corresponds to the well-known Wannier-Stark ladder problem for a particle moving in a tilted tight-binding lattice, see Fig. 4.5. The tilt  $I_0$  provides an energy difference equal to  $\hbar\omega_B$  between two adjacent phase states. The term proportional to  $U_0$  induces transitions between adjacent phase-states, i.e., phase-slip events. In the absence of microwaves or a coupling to the environment, we have only coherent Bloch oscillations and the associated energy difference  $\hbar\omega_B$  can not be accommodated by the system. Hence no finite DC component is found for the voltage  $V_J$  in this case.

Switching on the microwave field, the tilted lattice acquires an additional, oscillatory slope with amplitude  $I_{mw} \neq 0$ . For this problem, the unitary evolution operator can be evaluated exactly and it reads

$$\hat{U}(t) = e^{i\mathcal{Q}(t)\hat{n}} e^{i\frac{U_0}{2\hbar} \int_0^t dt' [\hat{K} \exp(i\mathcal{Q}(t')) + \hat{K}^\dagger \exp(-i\mathcal{Q}(t'))]}, \quad (4.13)$$

in which we set

$$\mathcal{Q}(t) = \omega_B t + \alpha \sin(\omega_{mw} t). \quad (4.14)$$

In Eq. (4.13), we also introduced the number operator  $\hat{n} = \sum_n n |n\rangle \langle n|$  and the ladder operator  $\hat{K} = \sum_n |n\rangle \langle n+1|$ . After some algebra, the expectation value of the voltage operator in Eq. (4.11) on the state  $\hat{U}(t) |q_0\rangle$ , the time evolved initial

quasi-charge state  $|q_0\rangle$ , is

$$\begin{aligned} V_J^{(\text{mw})}(t) &= V_c \sin[\chi_0 + \mathcal{Q}(t)] \\ &= V_c \sum_{m=-\infty}^{+\infty} J_m(\alpha) \sin(\chi_0 + \omega_B t + m\omega_{\text{mw}} t). \end{aligned} \quad (4.15)$$

Equation (4.15) coincides with Eq. (4.1) and describes the ideal dual Shapiro steps: a non-vanishing DC-voltage now appears each time the bias-current  $I_0 = I_J$  satisfies the condition  $I_J = me\omega_{\text{mw}}/\pi$ , as shown in Fig. 4.2. The dual Shapiro steps, labeled with the index  $m = 0, \pm 1, \dots$ , are replicas of the zero-voltage state obtained with  $m = 0$  and  $\alpha = 0$ , rescaled with the corresponding Bessel function of the first kind  $J_m(\alpha)$ . The coherent emission/absorption of microwave photons with energy  $\hbar\omega_{\text{mw}}$  is at the origin of this phenomenon, the well known phase-locking effect. The local phase states undergo a coherent quantum tunneling upon exchanging the energy  $\hbar\omega_{\text{mw}}$  with the microwave field, see Fig. 4.5.

### Perturbation theory

We next analyze the current-voltage characteristic of the QPSJ in terms of perturbation theory in microwave interaction  $\alpha$  and dissipative coupling  $g$ . We show that this approach systematically leads to divergent behaviour. For simplicity, we assume the bath to be at zero temperature.

Applying the unitary transformation  $\hat{U}_{\text{env}} = \exp[-i\hat{\phi}\hat{Q}_{\text{RL}}/2e]$  to Hamiltonian (4.7), we obtain the QPSJ Hamiltonian in the form  $\hat{H}'_s = \hat{H}_0 + \hat{H}_{\text{int}}$  in which we consider as the unperturbed Hamiltonian

$$\hat{H}_0 = -U_0 \cos\left(\frac{\pi}{e}\hat{q}\right) - \frac{\hbar I_0}{2e}\hat{\phi}, \quad (4.16)$$

and the interaction term

$$\hat{H}_{\text{int}} = -\frac{\hbar I_{\text{mw}}}{2e} \cos(\omega_{\text{mw}} t) \hat{\phi} + \hat{H}_{\text{env}} [\{\hat{Q}_\lambda\}, \{\hat{\phi}_\lambda + \hat{\phi}\}]. \quad (4.17)$$

In this canonical form, the voltage operator is given by

$$V_J = V_c \left\langle \sin\left(\frac{\pi}{e}\hat{q}\right) \right\rangle_{\text{DC}}. \quad (4.18)$$

Using the interaction picture, we expand the unitary time evolution operator in terms of  $\hat{H}_{\text{int}}$ , Eq. (4.17), to calculate  $V_J$ , Eq. (4.18). After some algebra, for vanishing microwave strength  $\alpha = 0$ , we obtain for the DC component of the voltage

$$V_J^{(\text{DC})} = \frac{gV_c^2}{2R_Q I_0}. \quad (4.19)$$

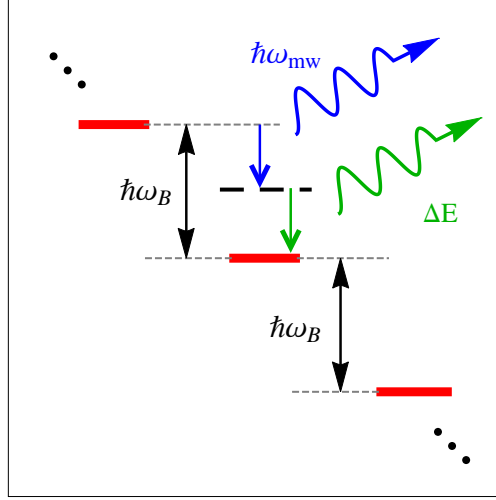


Figure 4.6: Wannier-Stark ladder in the presence of both microwave and environmental photons with energies  $\hbar\omega_{\text{mw}}$  and  $\Delta E$  respectively.

This result is indeed linear in  $g$  and corresponds to the first order expansion of the classical solution (4.5). Its validity requires  $V_J/V_c \ll 1$ , hence  $I_0 \gg gV_c/R_Q$ . We conclude that perturbation theory breaks down in the limit of vanishing DC current bias.

In the presence of microwaves,  $\alpha \neq 0$ , the result (4.19) generalizes to

$$V_J^{(\text{mw})} = \frac{gV_c^2}{2R_Q} \sum_{m=-\infty}^{+\infty} \frac{J_m^2(\alpha)}{I_0 + me\omega_{\text{mw}}/\pi}, \quad (4.20)$$

which shows that the divergent behavior found for  $I_0 \rightarrow 0$  is repeated at the positions  $I_0 \rightarrow me\omega_{\text{mw}}/\pi$  at which the dual Shapiro steps are expected.

Although the perturbative approach is divergent and is inappropriate to describe the dual Shapiro steps in the presence of dissipation, it is useful for giving a simple picture of the QPSJ's dynamics: the incoherent tunneling of the localized phase states in the Wannier-Stark ladder generally occurs via the combined emission and/or absorption of a certain number of photons with energy  $\hbar\omega_{\text{mw}}$  of the microwave source and the exchange of an amount of energy  $\Delta E$  with the thermal bath, see Fig. 4.6. One expects that the interplay between the photon-assisted and environment-assisted phase-slippage causes the smearing of the ideal dual Shapiro steps. Indeed, the sharp resonance condition  $\hbar\omega_B = \hbar\omega_{\text{mw}}$  associated to the single microwave photon emission can not be fulfilled anymore as the QPS junction can now dissipate the energy  $\hbar\omega_B$  at any bias current because the energy difference  $\Delta E = \hbar(\omega_B - \omega_{\text{mw}})$  is emitted in the environment, see Fig. 4.6.

### 4.3 Dual Shapiro's steps: non-perturbative formal approach

We now develop a theory to describe the combined effect of charge fluctuations induced by the environment on one hand and microwave irradiation on the other hand, which is non-perturbative in both  $g$  and  $\alpha$ . To determine the current-voltage characteristic of the QPSJ by means of Eq. (4.10), we need the DC component  $V_J$  of the potential across the QPSJ given by Eq. (4.11). The quantum statistical average in the r.h.s. of Eq. (4.11) can be calculated by means of the Keldysh formalism (see Appendix E for a more detailed derivation) [22, 92, 106, 107]. Introducing the so-called Keldysh closed time-contour  $C_k$  which goes from  $t = -\infty$  to  $t = t_0$  and back to  $t = -\infty$  and treating the cosine term in Eq. (4.7) as a perturbation, one can obtain an exact series expansion in terms of the QPSJ energy  $U_0$ . In this expansion, the contribution of the oscillators forming the harmonic bath decouples from the contribution of the QPSJ charge  $q$  so that one can evaluate the quantum statistical averages exactly to each order. We have generalized this solution taking into account the presence of the microwave signal. The time-dependent voltage across the QPSJ reads

$$\frac{V_J(t_0)}{V_c} = \sum_{n=0}^{+\infty} \frac{(-1)^n}{2i} \left( \frac{U_0}{\hbar} \right)^{2n+1} \sum_{\{\eta_k\}} \int_{-\infty}^{t_0} dt_1 \dots \int_{-\infty}^{t_{2n}} dt_{2n+1} F_{\text{env}} F_q, \quad (4.21)$$

where the term  $F_{\text{env}}$ ,

$$F_{\text{env}} = e^{\sum_{k=1}^{2n+1} \sum_{k'=0}^{k-1} \eta_k \eta_{k'} M(t_{k'} - t_k)} \prod_{k=1}^{2n+1} \sin \left[ \sum_{k'=0}^{k-1} \eta_{k'} A(t_{k'} - t_k) \right], \quad (4.22)$$

accounts for the environment-assisted phase-slip events and  $F_q$ ,

$$F_q = e^{i \sum_{k=0}^{2n+1} \mathcal{Q}(\eta_k t_k)} = \exp \left\{ i \sum_{k=0}^{2n+1} [\omega_B \eta_k t_k + \alpha \sin(\omega_{\text{mw}} \eta_k t_k)] \right\}, \quad (4.23)$$

is related only to the free dynamics of the charge  $q$  as given by Eq. (4.14). The dichotomic variables  $\eta_k = \pm 1$ , with  $k = 0, 1, \dots, 2n+1$ , satisfy the constraint  $\sum_{k=0}^{2n+1} \eta_k = 0$  and the sum  $\sum_{\{\eta_k\}}$  over all the possible configurations of  $\eta_k$  stands for the product of the  $2n+2$  sums  $\sum_{\eta_1=\pm} \dots \sum_{\eta_{2n+1}=\pm}$ .

The functions of time  $M(t)$  and  $A(t)$  in Eq. (4.22) describe the exchange of energy between the QPSJ and the external electromagnetic environment. They determine

$$J(t) = -M(t) - i \text{sign}(t) A(t), \quad (4.24)$$

i.e., the charge-charge correlation function

$$J(t) = \sum_{\lambda} \langle \hat{Q}_{\lambda}(t) \hat{Q}_{\lambda}(0) - \hat{Q}_{\lambda}^2(0) \rangle, \quad (4.25)$$

which quantifies the fluctuations of the tunneling phase due to the thermal bath [1, 108]. In particular,  $J(t)$  gives the coupling strength between the QPSJ and the environment. For the current-biased configuration of Fig. 4.1(b), we have

$$J(t) = 2R_Q \int_{-\infty}^{+\infty} \frac{d\omega}{\omega} \Re[Y(\omega)] \left( \frac{e^{-i\omega t} - 1}{1 - e^{-\hbar\omega\beta}} \right), \quad (4.26)$$

where  $Y(\omega)$  is the admittance (4.2) of the circuit and  $\beta = 1/k_B T$  the inverse temperature. An exact calculation yields [22, 92]

$$A(t) = \pi g \left( 1 - e^{-\omega_{\text{RL}}|t|} \right), \quad (4.27)$$

$$M(t) = 2g \frac{\pi|t|}{\hbar\beta} - A(t) \cot\left(\frac{\hbar\omega_{\text{RL}}\beta}{2}\right) + 2g \sum_{n=1}^{+\infty} \frac{1}{n} \frac{1 - e^{-v_n|t|}}{1 - (v_n/\omega_{\text{RL}})^2}. \quad (4.28)$$

Here  $v_n = 2\pi n/\hbar\beta$  is the  $n$ -th Matsubara frequency, and  $\omega_{\text{RL}} = R/L$  is the frequency scale characterizing the environment fluctuations at vanishing temperature.

The Jacobi-Anger expansion  $\exp[i\alpha \sin(x)] = \sum_{m=-\infty}^{+\infty} J_m(\alpha) \exp[imx]$  allows to cast  $F_q$  in terms of the Bessel functions of the first kind  $J_m(\alpha)$ ,

$$F_q = \sum_{m_0=-\infty}^{+\infty} J_{m_0}(\alpha) \dots \sum_{m_{2n+1}=-\infty}^{+\infty} J_{m_{2n+1}}(\alpha) \exp\left[ i \sum_{k=0}^{2n+1} (\omega_B + \omega_{\text{mw}} m_k) \eta_k t_k \right]. \quad (4.29)$$

Performing the change of variables  $\tau_k = t_{k-1} - t_k$ , each time  $t_k$  can be expressed as  $t_k = t_0 - \sum_{h=1}^k \tau_h$  with  $k \geq 1$ . Then Eq. (4.29) becomes

$$\begin{aligned} F_q &= \sum_{\{m_k\}} \left( \prod_{m_k} J_{m_k} \right) \exp\left( i \omega_{\text{mw}} t_0 \sum_{k=0}^{2n+1} \eta_k m_k \right) \\ &\times \exp\left[ -i \sum_{k=0}^{2n+1} (\omega_B + \omega_{\text{mw}} m_k) \eta_k \sum_{h=1}^k \tau_h \right] \end{aligned} \quad (4.30)$$

where we used the sum rule  $\sum_k \eta_k = 0$ . Unlike the functions  $M(t_{k'} - t_k)$  and  $A(t_{k'} - t_k)$  in Eq. (4.22) which depend only on the time difference  $t_{k'} - t_k = \sum_{h=1}^k \tau_h - \sum_{h'=1}^{k'} \tau_{h'}$ , Eq. (4.30) is a function of the time  $t_0$  at which we calculate the voltage across the QPSJ. From Eq. (4.30) we observe that the frequency spectrum of

Eq. (4.21) at the time  $t_0$  involves integer components of the single fundamental frequency  $\omega_{\text{mw}}$  applied to the dual junction. This frequency mixing is due to the QPSJ which operates as a non-linear capacitance, i.e., it is related to the cosine dependence of the QPSJ energy as a function of the charge  $q$ . Thus, in the steady state regime, we can extract the DC component by considering the time average of the general signal as  $\overline{f(t)} = (1/T_{\text{mw}}) \int_{t_i}^{t_i+T_{\text{mw}}} dt f(t)$  over a microwave period  $T_{\text{mw}} = 2\pi/\omega_{\text{mw}}$  where  $t_i$  is an arbitrary initial time. Then, the DC voltage reads

$$\frac{V_J}{V_c} = \frac{\overline{V(t_0)}}{V_c} = \dots \overline{F_q(t_0)} = \dots \frac{1}{T_{\text{mw}}} \int_{t_i}^{t_i+T_{\text{mw}}} dt_0 e^{i\omega_{\text{mw}}t_0} \sum_{k=0}^{2n+1} \eta_k m_k . \quad (4.31)$$

The latter quantity is different from zero only if the sum rule  $\sum_{k=0}^{2n+1} \eta_k m_k = 0$  is satisfied for each arbitrary configuration of the variables  $\{\eta_k\}$  at given set of the integers  $\{m_k\}$  associated to the expansion of the Bessel functions.

## 4.4 Lowest order results

A general analysis of the  $U_0$ -expansion Eq. (4.31) is only possible in limiting cases. We focus here on the experimentally most relevant limit of relatively small QPSJ energy  $U_0$ , typically encountered in Josephson junction-based QPSJs. Then Eq. (4.31) can be approximated with its first term. We discuss the range of validity of this approximation below. Considering  $n = 0$  only, the non-zero dichotomic variables are  $\eta_0 = \pm$  and  $\eta_1 = \pm$ . Since they have to satisfy the constraint  $\sum_k \eta_k = \eta_0 + \eta_1 = 0$ , it follows that the allowed configurations  $\{\eta_k\} = (\eta_0, \eta_1)$  are  $(-, +)$  and  $(+, -)$ , i.e.,  $\eta_0$  and  $\eta_1$  have opposite sign. This means that the time-average given by Eq. (4.31) is different from zero if the indices  $m_0$  and  $m_1$  of the two possible sums of Bessel functions in Eq. (4.29) are equal.

### 4.4.1 DC-current-biased QPSJ

Let us first consider the case without microwave irradiation. Setting  $\alpha = 0$  in Eq. (4.31), and retaining the term  $n = 0$  only, the voltage drop on the QPSJ as a function of  $\omega_B$  reads

$$\frac{V_J^{(\text{DC})}}{V_c}(\omega_B) \simeq \frac{\pi}{2} U_0 [P(\hbar\omega_B) - P(-\hbar\omega_B)] , \quad (4.32)$$

where we defined the function [1, 92]

$$P(\Delta E) \equiv \frac{1}{2\pi\hbar} \int_{-\infty}^{+\infty} d\tau e^{J(\tau)} e^{\frac{i}{\hbar}\Delta E\tau} . \quad (4.33)$$

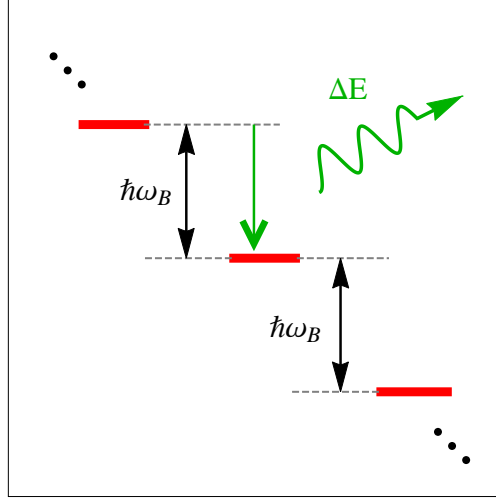


Figure 4.7: Environment-assisted transitions between adjacent states in the Wannier-Stark ladder lead to the appearance of a finite voltage across the QPSJ element.

The function  $P(\Delta E)$  represents the probability density that the QPSJ absorbs ( $\Delta E > 0$ ) or emits ( $\Delta E < 0$ ) an amount of energy  $|\Delta E|$  from or to the external environment respectively during a phase-slip event. It is dual to the well-known function  $P(E)$  used to describe charge tunnelling in the presence of an environment [1]. We see that an incoherent phase slippage by  $\Delta\varphi = 2\pi$  in the Wannier-Stark Ladder takes place only if the system exchanges the energy  $\Delta E = \hbar\omega_B = (\Delta\varphi)\hbar I_0/(2e)$  with the environment, see Fig. 4.7. As the energy spectrum of the bath is continuous, the QPSJ has a dissipative behavior for any value of the applied DC-current  $I_0$ .

The validity of Eq. (4.32) is given by the condition  $V_J^{(\text{DC})}/V_c \ll 1$ , yielding  $U_0 \max[P(\hbar\omega_B)] \ll 1$  [108]. The current-voltage characteristics displayed in Fig. 4.3 have been obtained from Eqs. (4.32) and (4.33) by direct numerical integration, using the correlation function Eq. (4.26). However, analytical results are available, for instance, in the limit of low temperature and small conductance so that  $\beta E_L/2\pi^2 g \gg 1$  and  $\beta E_L/2\pi^2 g^2 \gg 1$ . Then

$$\frac{V_J^{(\text{DC})}}{V_c}(\omega_B) \simeq u \frac{|\Gamma(g + i\beta\hbar\omega_B/2\pi)|^2}{\Gamma(2g)} \sinh(\beta\hbar\omega_B/2), \quad (4.34)$$

where  $u = (\beta U_0/4\pi)(\beta E_L e^\gamma/2\pi^2 g)^{-2g}$  with  $\gamma = 0.577\dots$  the Euler constant. Hence we find a linear conductance  $G_0$  at vanishing current  $I_J$  and voltage  $V_J$

( $\hbar\omega_B\beta/2\pi \ll 1$ ), given by

$$G_0 R_Q \approx 4(U_0\beta)^{2(g-1)} \left(\frac{E_L}{U_0}\right)^{2g} \left(\frac{1}{2\pi^2 g}\right)^{2g} \frac{\Gamma(2g)}{\Gamma^2(g)} e^{2g\gamma} - g. \quad (4.35)$$

We note that  $G_0 \sim T^{2-2g}$  and thus decreases with decreasing temperature; similarly  $G_0 \sim E_L^{2g} \sim 1/L^{2g}$  and thus decreases with increasing inductance. Moreover,  $G_0$  decreases with decreasing  $g$ .<sup>2</sup>

Increasing  $\omega_B$  till  $\omega_B^{\max} \approx 2\pi g/(\hbar\beta)$ , we reach the back-bending point corresponding to the maximum value

$$\left(\frac{V_J^{(\text{DC})}}{V_c}\right)_{\max} \approx \pi u = \frac{1}{4}(\beta U_0)^{1-2g} \left(\frac{U_0}{E_L}\right)^{2g} (2\pi^2 g)^{2g} e^{-2\gamma g}, \quad (4.36)$$

for  $g \ll 1$ . We see that the lower the temperature  $T$ , the larger is the inductance  $L$  and the smaller the conductance  $g$ , the closer  $V_{J,\max}$  is to the maximum value  $V_c$ . Beyond the back-bending point, the system enters into the Bloch oscillation branch where the bias energy  $\hbar\omega_B$  becomes dominant with respect to both quantum and thermal fluctuations and the DC-voltage  $V_J$  vanishes exponentially.

Another interesting limit is the high-conductance regime  $g \gg 1$ . In this limit, the QPSJ is strongly coupled to the external electromagnetic dissipative environment and

$$P(\Delta E) \simeq \frac{1}{\sqrt{4\pi E_L k_B T}} \exp\{-(\Delta E - E_L)^2/(4E_L k_B T)\}. \quad (4.37)$$

As a result, the Bloch nose broadens into a Gaussian with a width  $\sqrt{E_L k_B T}$  and peaked at the inductive energy  $E_L$ , as can be seen in Fig. 4.3. Lowering the temperature such that  $\beta E_L \gg 1$ ,  $P(\Delta E) \rightarrow \delta(\Delta E - E_L)$ . As a result, phase-slip events in a current-biased QPSJ can only occur if the energy  $\hbar\pi I_0/e$  exchanged with the inductive environment equals  $E_L$ . This is the phenomenon dual to the Coulomb blockade of Cooper pair tunneling in a voltage-biased Josephson junction embedded in a highly resistive environment, where the transfer of Cooper pairs is possible only if the energy  $2eV$  exchanged with the environment equals to the charging energy  $E_C$ .

---

<sup>2</sup>the conductance  $G_0$  can become negative, signalling the breakdown of the lowest order result (4.32).

#### 4.4.2 Microwave irradiated QPSJ

In the presence of the microwave source, the  $n = 0$  term in the time-averaged expansion Eq. (4.31) can be written as

$$V_J^{(\text{mw})}(\omega_B) = \sum_{m=-\infty}^{+\infty} J_m^2(\alpha) V_J^{(\text{DC})}(\omega_B + m\omega_{\text{mw}}). \quad (4.38)$$

Comparing Eq. (4.38) with Eq. (4.32), we see that, under the effect of the microwave radiation, the first-order voltage across the QPS junction is the superposition of an infinite number of zero-microwave potentials shifted by an integer multiple  $m$  of  $\omega_{\text{mw}}$ . Unlike Eq. (4.15), the weight of the  $m$ -th term in Eq. (4.38) is determined by the squared first-kind Bessel function of the  $m$ -th order,  $J_m^2(\alpha)$ . This result is in agreement with the general theorem proved in Ref. [105]. Since the sum rule  $\sum_{m=-\infty}^{+\infty} J_m^2(\alpha) = 1$  holds, the larger is  $\alpha$  the smaller is the amplitude of the voltage corresponding to  $m = 0$  and consequently the more important is the contribution of the higher-order terms. In other words, changing the amplitude  $\alpha$ , the constant total weight re-distributes among the infinite terms of Eq. (4.38).

Using Eq. (4.10) in combination with Eq. (4.38), we find that the  $I_J$ - $V_J$  characteristic of the QPSJ consists of  $(m\omega_{\text{mw}})$ -shifted and rescaled copies of the QPSJ's characteristic in the absence of microwaves, Eq. (4.32), obtained for  $I_{\text{mw}} = 0$ . These features occurring at  $I_{J,m} = me\omega_{\text{mw}}/\pi$  represent the dual or current Shapiro steps smeared by quantum and thermal fluctuations induced by the thermal bath. These results are shown in Fig. 4.4, obtained by direct numerical evaluation of Eq. (4.32) in combination with Eq. (4.38) for  $g < 1$ . The plotted smeared  $I_J$ - $V_J$  curves result from the competition and interference between the environment-assisted phase slippage and the pure photon-assisted tunneling of the phase induced by the microwave field. In order for these features to be resolved, the microwave frequency  $\omega_{\text{mw}}$  has to be much larger than  $\omega_B^{\text{max}} \approx 2\pi g/(\hbar\beta)$ , the bias current corresponding to the back-bending point  $(V_J^{(\text{DC})}/V_c)_{\text{max}}$ , see Eq. (4.36).

When  $g > 1$ , the current-voltage characteristics of the microwave-irradiated QPSJ typically look like the ones plotted in Fig. 4.8. We find that they consist of replicas of the smeared current-voltage characteristics for  $g > 1$  and  $I_{\text{mw}} = 0$ , see Fig. 4.3, centered around the positions of the ideal Shapiro steps shown in Fig. 4.2. Since the  $I_J$ - $V_J$  characteristics for  $g > 1$  are more smeared than the ones found in the low-conductive case, a higher microwave frequency  $\hbar\omega_{\text{mw}}/2\pi U_0 = 20$  has been used to resolve the various replicas and obtain Fig. 4.8. When increasing the inductance  $L$  for  $g > 1$ , the smearing effects are reduced. The inset of Fig. 4.8 shows the relative accuracy  $\delta I_m = \pi I_J/m e \omega_{\text{mw}} - 1$  of the structure found at  $m = 1$  when compared to a perfect dual Shapiro step. We see that the high conductance case does not produce single dual Shapiro steps, but rather a doublet of two steps,

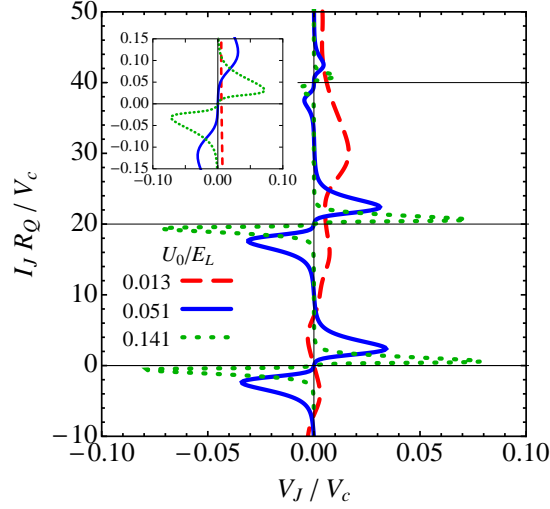


Figure 4.8:  $I_J$ - $V_J$  characteristics obtained from the numerical evaluation of Eq. (4.38) in the high-conductive regime,  $g = 4.2$ . Here  $k_B T / U_0 = 0.25$  and  $\alpha = 1.4$ . The dimensionless frequency of the microwaves  $\hbar\omega_{\text{mw}}/2\pi U_0$  is equal to 20. The three curves are obtained using three different values of the inductance such that  $U_0/E_L = 0.013$  (red dashed line),  $U_0/E_L = 0.051$  (blue solid line),  $U_0/E_L = 0.141$  (green dotted line). The inset shows the relative deviation  $\delta I_m = \pi I_J / me\omega_{\text{mw}} - 1$  of the structure found for  $m = 1$  with respect to a perfect first Shapiro step.

located symmetrically around the value  $me\omega_{\text{mw}}/\pi$ . Combining Eq. (4.38) and the asymptotic result (4.37), we expect the positions of the steps of the doublets to approach their asymptotic values  $me\omega_{\text{mw}}/\pi \pm \Phi_0/2L$  with increasing conductance  $g$ . Eventually, a single dual Shapiro step is recovered for  $L \rightarrow \infty$ .

### 4.4.3 Accuracy of the current Shapiro steps

The reduction of quantum and thermal fluctuations affecting the dual Shapiro steps is crucial for their experimental observation as well as their potential applications, such as in metrology. In this respect, it is important to analyze the accuracy of the dual steps. We focus on the relevant regime of low conductance,  $g < 1$ , where actual well-defined dual Shapiro steps are found and examine the smearing of the  $m$ -th step by considering the relative deviation  $\delta I_m = \pi I_J / me\omega_{\text{mw}} - 1$ . Based on the asymptotic results of Eqs. (4.35) and (4.36), we expect a minimal smearing when  $T$  and  $g$  are chosen as small as possible and  $L$  large.

The behavior of  $\delta I_m$  as a function of some of the relevant system parameters is studied numerically in Fig. 4.9 and Fig. 4.10 for the first dual Shapiro step,  $m =$

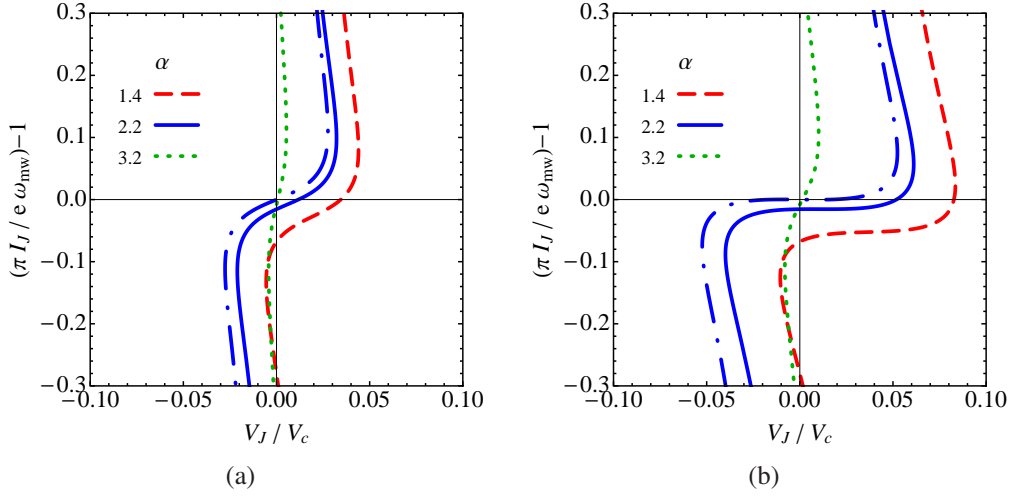


Figure 4.9: Relative deviation  $\delta I_m$  for the first Shapiro step  $m = 1$ , for  $k_B T/U_0 = 0.1$  and  $\hbar\omega_{\text{mw}}/2\pi U_0 = 0.16$ . The panel (a) corresponds to  $U_0/E_L = 0.0032$  and the panel (b) to  $U_0/E_L = 0.013$ . The lines correspond to three different microwave strengths,  $\alpha = 1.4, 2.2, 3.2$  are for, respectively, the (red) dashed, the (blue) solid and the (green) dotted line. It is also shown the (blue) dashed-dotted line for the behavior for the unperturbed Shapiro step for  $\alpha = 2.2$  (see text).

1. In these figures, the solid, dashed and dotted lines correspond to three different microwave strengths  $\alpha = 1.4, 2.2$ , and  $3.2$ . Also shown (dashed-dotted line) is the behaviour of the unperturbed dual Shapiro step for  $\alpha = 2.2$ , i.e.,  $J_1^2(2.2) \times V_J^{(\text{DC})}(\omega_B - \omega_{\text{mw}})$ , obtained by subtracting the contributions from all the other steps corresponding to  $m \neq 1$  from the signal.

One sees that two phenomena generally limit the accuracy of the steps: (i) they are smeared around the actual plateau value and (ii) their position is offset with respect to the expected one. The latter phenomenon is absent for the unperturbed step: indeed the shift of the step position is due to the finite overlap of the  $m = 1$  replica of the Bloch nose with all the other replicas  $m \neq 1$ . This suggests that increasing the microwave frequency should yield a better accuracy of the step position as it separates the replicas more, thereby reducing their overlap and, at the same time, improving their individual resolution. The result of an increasing of  $\omega_{\text{mw}}$  on the step position can be seen by comparing Fig.4.9(b) with Fig.4.10. We notice, for instance, that when  $\alpha = 2.2$  the relative offset reduced from about 0.02 in the former to about 0.0004 in the latter by increasing  $\omega_{\text{mw}}$  by a factor of 10.

It is interesting to investigate why the curve for  $\alpha = 2.2$  is less affected by the offset than the one for  $\alpha = 1.4$ , although the step size is the same for both

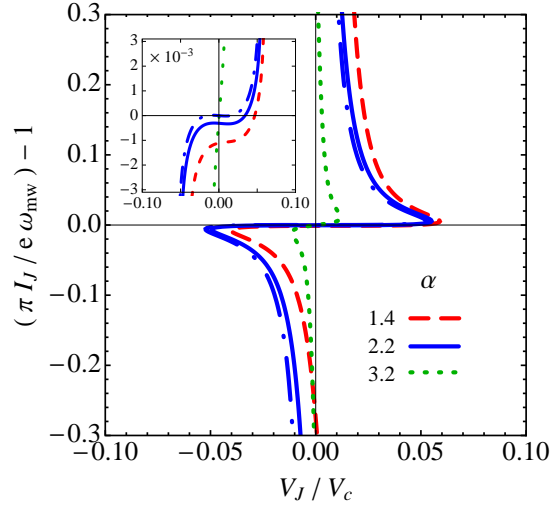


Figure 4.10: Relative deviation  $\delta I_m$  for the first Shapiro step  $m = 1$ , for  $k_B T / U_0 = 0.1$ ,  $\hbar \omega_{\text{mx}} / 2\pi U_0 = 2$  and  $U_0 / E_L = 0.013$ . The lines correspond to three different microwave strengths,  $\alpha = 1.4, 2.2, 3.2$  are for, respectively, the (red) dashed, the (blu) solid and the (green) dotted line. It is also shown the (blue) dashed-dotted line for the behaviour for the unperturbed Shapiro step for  $\alpha = 2.2$  (see text).

curves. Indeed, the value of the squared Bessel functions  $J_1^2(\alpha)$  determining the  $m = 1$  step width is almost equal for the two curves. However the value  $J_0^2(\alpha)$  is very different:  $J_0^2(2.2) \approx 0.01$  whereas  $J_0^2(1.4) \approx 0.32$ . In other words, the  $m = 0$  Shapiro step will strongly influence the step  $m = 1$  for  $\alpha = 1.4$ , leading to a large offset, whereas it influences the  $m = 1$  step much less for  $\alpha = 2.2$ . The step corresponding to  $\alpha = 3.2$  is more or less structureless, as its weight is very small,  $J_1^2(3.2) \approx 0.07$ .

As far as the smearing is concerned around the actual plateau position, a comparison between Fig. 4.9(a) and Fig. 4.9(b) shows the effect of the inductance. Increasing the inductance by a factor of 4 reduces the relative width of the step from about 0.1 in Fig. 4.9(a) to about 0.05 in Fig. 4.9(b).

#### 4.4.4 The effect of Joule heating

In this section, we discuss an important aspect related to the experiment aimed to detect dual Shapiro steps, namely the effect of Joule heating in the I-V characteristic of the QPSJ [97, 101, 103, 104].

As we have seen above, we expect to approach the ideal dual Shapiro steps of Fig. 4.2 under the condition  $g \ll 1$ . This means that the QPSJ is ideally embedded in a highly-dissipative environment. Such an environment is expected to produce

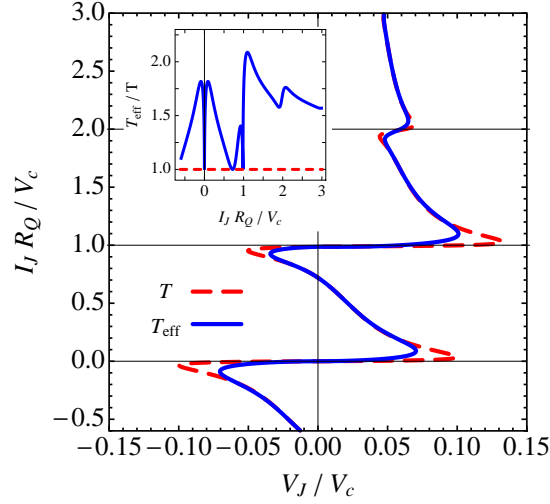


Figure 4.11: Effect of Joule heating on the dual Shapiro steps obtained from the numerical evaluation of Eq. (4.38) in the low-conductive regime,  $g = 0.2$ . For the red dashed  $I_J$ - $V_J$  curve the temperature is fixed to  $k_B T / U_0 = 0.25$ , and the inductance of the environment is such that  $U_0 / E_L = 0.141$ , as for the green dotted line in Fig. 4.4. On the other hand, the blue curve has been determined using the effective temperatures  $T_{\text{eff}}$  which are solution of Eq. 4.39 with  $k_B T_{\text{ph}} / U_0 = 0.25$ , and  $U_0 / \hbar = 4$  GHz. We set the parameters  $\Sigma = 10^9 \text{ W m}^{-3} \text{ K}^{-5}$  and  $\Omega = 10^{-19} \text{ m}^3$  in agreement with the recent experiments discussed in Ref. [103]. The inset shows the rescaled effective temperature  $T_{\text{eff}} / T$  as a function of the current through the QPSJ.

also unwanted Joule heating which in turn would enhance the smearing of the steps. Indeed, in the low-conductance limit,  $R \gg R_Q$ , quantum effects due to the external bath become small, whereas thermal ones induced by heating may become dominant. In this context, the effective electronic temperature  $T_{\text{eff}}$  of the  $R$ - $L$  series can be much larger than the phonon temperature  $T_{\text{ph}}$ . For the circuit of Fig. 4.1(b), the current flowing through the  $R$ - $L$  branch is  $V_J / R$ , then the power dissipated by the resistance is  $P_J = V_J^2 / R$ , where  $V_J$  is a function of the temperature (see Eq. 4.38). It follows that the effective temperature  $T_{\text{eff}}$  can be determined by the self-consistent equation [53]

$$T_{\text{eff}}^5 = T_{\text{ph}}^5 + \frac{V_J^2(T_{\text{eff}}, \omega_B)}{R \Sigma \Omega}. \quad (4.39)$$

In this last relation,  $\Sigma$  is the material-dependent electron-phonon coupling constant, and  $\Omega$  the volume of  $R$ .

Figure 4.11 shows the I-V curve of a QPSJ embedded in an environment with  $g \ll 1$  and fixed temperature,  $k_B T / U_0 = 0.25$ , where the Joule heating is not

taken into account, together with the dual Shapiro steps smeared by the voltage-dependent effective temperature Eq. 4.39 which accounts for the exchange of energy between the electrons and the phonons in the resistance  $R$ . We notice a reduction of the width of the steps, as one expects, which compromise their experimental observation. However, this problem can be overcome by increasing the inductance  $L$  of the environment rather than the resistance  $R$ . Indeed,  $L$  plays the same role of  $R$  in the reduction of the fluctuations, as shown previously. As the dual Shapiro steps are replicas of the I-V characteristic at low current, we can estimate the leading dependence for the smearing by considering Eq. 4.35. We obtain the slope

$$G_0 R_Q \approx 2g \left( \frac{k_B T}{U_0} \right)^2 \left( \frac{E_L}{U_0} \right)^{2g}, \quad (4.40)$$

for  $g \ll 1$ . We observe that the smearing due to the temperature can partially be compensated by increasing the inductance of the environment.

## 4.5 Conclusions

In this chapter, we discussed the microwave response of a QPSJ embedded in an inductive-resistive environment. We focused on the regime of relatively small ratio of phase-slip energy  $U_0$  over inductive energy  $E_L$ . The response consists of a series of well-defined current Shapiro steps, located at multiples of  $e\omega_{\text{mw}}/\pi$ , if the environmental resistance is sufficiently large, such that the dimensionless conductance  $g < 1$ . These steps are in fact replicas of the QPSJ's Bloch nose, observed in the absence of microwaves. Charge fluctuations induced by the environment smear the steps. This smearing can be reduced by decreasing the dimensionless environmental conductance  $g$ , decreasing the dimensionless temperature  $k_B T/U_0$  and increasing the ratio  $U_0/E_L$ , which can be achieved by increasing environmental inductance  $L$ . Finally, we showed that the conductance  $g$  can not be decreased indefinitely, as heating effects may develop in the environment.

The results presented in this chapter are relevant for recent experiments on Josephson junction chains [97] and nanowires [101, 104]. In these works, typical phase-slip energies  $U_0$  are in the range of  $1 \div 10$  GHz, whereas the environmental inductances  $L$  are  $50 \div 500$  nH. This motivated the parameter choices used in this chapter:  $U_0/E_L$  ranges from  $0.001 \div 0.1$ ; at typical cryostat temperatures  $k_B T/U_0 \sim 0.1 \div 0.2$ . We found that, although dual Shapiro-like features could be visible experimentally for these parameters, their relative accuracy remains limited to about 0.001 by fluctuation effects.

To date, a systematic evidence for the existence of dual Shapiro steps is still lacking. The reason for this might well be that fluctuation effects have so far masked the steps for QPSJs with intermediate ratios of the parameter  $U_0/E_L$  and

not too small conductance  $g$ . Work on nanowire-based QPSJs with larger values of the ratio  $U_0/E_L$  and lower conductances  $g$  [102, 109] seems promising; at the same time these systems suffer from substantial heating effects [103]. We conclude that further work is necessary, both on nanowires and on Josephson junction chains.

## Conclusions

In conclusion, we have theoretically studied some phenomena concerning the electronic charge and heat transport in four different superconducting nanostructures based on tunnel junctions: a single NIS junction, a SINIS turnstile, a cascade electron refrigerator, and a quantum phase-slip junction. Our main findings, discussed in details in the four previous chapters of this PhD thesis, are the following:

- **first chapter** – evaluation of the subgap leakage current observed in the current-voltage characteristic of a NIS junction and its connection with the phenomenological Dynes parameter; such a subgap current can be reduced exponentially and the metrological accuracy reached by means of a highly-resistive transmission line.
- **second chapter** – derivation of the photon-assisted Andreev rate in a SINIS turnstile; the single-electron tunneling accuracy in this device can be increased up to the metrological requirement upon decreasing the Dynes parameter  $\gamma_{\text{Dynes}}$  and increasing the charging energy  $E_C$ .
- **third chapter** – study of the operation of an electronic cooler based on a combination of superconducting tunnel junctions; this device allows to cool a normal metal island down to about 100 mK starting from a bath temperature of 500 mK and it is more efficient than the simpler SINIS nanorefrigerator.
- **forth chapter** – determination of the smeared current-voltage characteristic of a current-biased quantum phase-slip junction under microwave irradiation and connected to an inductive and resistive environment; the smearing, due to thermal and quantum fluctuations, can be decreased upon increasing the inductance of the environment, thereby allowing the experimental observation of the dual or current Shapiro steps.



# **Appendices**



# Electron Tunneling in a SINIS Turnstile

## Introduction

In this Appendix, we derive the energy costs Eqs. (2.1) and (2.2) and the threshold voltages which determine the Coulomb diamonds for single- and double-electron tunneling processes in a SINIS turnstile.

### A.1 Energy of a single-island circuit

Let us consider a single metallic island (ISL) capacitively connected to  $M_S$  voltage sources via  $M_J$  tunnel junctions [see Fig. A.1(a)]. The total energy  $E$  of such a common electrode consists of the difference between two terms [39]. The first one is the electrostatic energy  $U$  due to the Coulomb interactions in terms of the  $n$  excess charges on the island. In terms of the potential  $V_I$  of ISL,  $U$  can be written as

$$U = \frac{1}{2} \sum_{i=1}^{M_S} C_i (V_I - V_i)^2, \quad (\text{A.1})$$

where  $V_i$  is the voltage source connected to the  $i$ -th junction with capacitance  $C_i$ . Since the total charge  $Q = -ne$  of the island is the sum of the charges on all the capacitors  $C_1, \dots, C_{M_J}, C_{g_1}, \dots, C_{g_k}$  of the system,

$$Q(n) = \sum_{i=1}^{M_S} C_i (V_I - V_i) = -ne,$$

the voltage  $V_I$  reads

$$V_I(n) = \frac{1}{C_\Sigma} \left( \sum_{i=1}^{M_S} C_i V_i - ne \right), \quad (\text{A.2})$$

where  $C_\Sigma = \sum_i C_i$  is the total capacitance. The insertion of this last expression in Eq. (A.1) yields

$$U(n) = \frac{1}{2C_\Sigma} \sum_{i=1}^{M_S} \sum_{j>i}^{M_S} C_i C_j (V_i - V_j)^2 + \frac{(ne)^2}{2C_\Sigma}, \quad (\text{A.3})$$

after some algebra. Now the electron number  $n$  appear explicitly in  $U(n)$ .

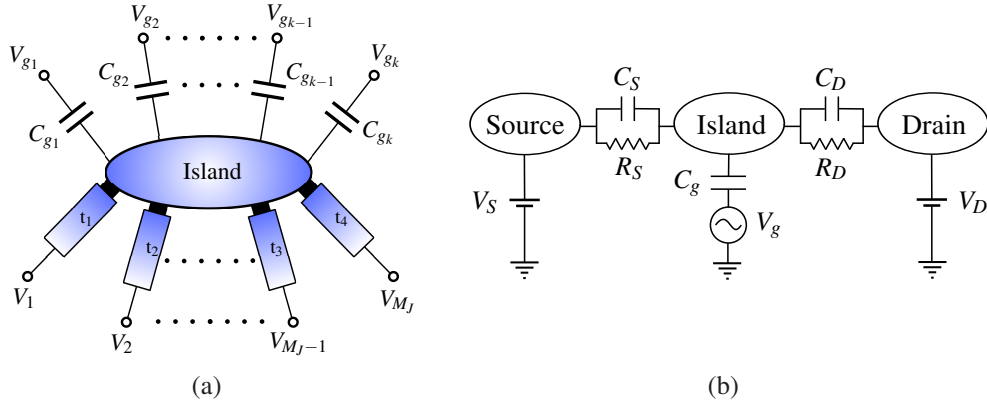


Figure A.1: (a) Sketch of a metallic island connected to  $M_J$  voltage sources via  $M_J$  tunnel junctions with capacitances  $C_1, \dots, C_{M_J}$  and to  $k = M_S - M_J$  gate voltages by means of the capacitors  $C_{g_1}, \dots, C_{g_k}$ . (b) Sketch of a single-electron transistor (SET) constituted by a drain electrode, a source electrode. The voltage gate  $V_g$  induces the charge  $n_g = C_g V_g / e$  on the central island.

The energy cost for changing  $n$  via tunneling events is the other contribution to the total energy of the island  $E$ . If one electron tunnels through the  $j$ -th junction, then the potential of the island changes by  $\Delta V_I = V_I(n+1) - V_I(n) = -e/C_\Sigma$  [see Eq.(A.2)]. This means that the charge  $C_i \Delta V_I = -eC_i/C_\Sigma$  is added to each capacitor in order to redistribute the tunneled particle  $-e$ . As a result, the work done by all the voltage sources is

$$W_j = -eV_j + \sum_{i=1}^{M_S} V_i \frac{eC_i}{C_\Sigma} = \frac{e}{C_\Sigma} \sum_{i=1}^{M_S} C_i (V_i - V_j),$$

which contains the energy related to the tunneling of the electron,  $-eV_j$ , as well as the energy cost to have an increment of the charge equal to  $+eC_i/C_\Sigma$  across the capacitance  $C_i$ . Summing up over all the tunnel junctions  $M_J$ , the total work is

$$W = \sum_{j=1}^{M_J} n_j W_j \quad (\text{A.4})$$

where  $n_j$  is the number of charges which overcome the  $j$ -th junction.

The total energy of the island, with  $n$  charges  $-e$  localized on it, is then given by the Gibbs free energy

$$E(n) = \frac{1}{2C_\Sigma} \sum_{i=1}^{M_S} \sum_{j>i}^{M_S} C_i C_j (V_i - V_j)^2 + \frac{(ne)^2}{2C_\Sigma} - \frac{e}{C_\Sigma} \sum_{j=1}^{M_J} n_j \sum_{i=1}^{M_S} C_i (V_i - V_j) . \quad (\text{A.5})$$

i.e., the difference between the energy stored into the ISL, Eq.(A.3), and the energy involved in the change of the number of the extra-charge, Eq.(A.4), acting as a chemical potential.

## A.2 The single-electron transistor (SET)

We describe here the operation of the so-called single-electron transistor (SET). Using the results derived in the previous section, we discuss under which conditions a single-electron current can flow through such a device.

### A.2.1 Energy cost

We start by applying Eq.(A.5) to the SET illustrated in Fig. A.1(b). Such a device is constituted by a single metallic island connected to the source ( $S$ ) and the drain ( $D$ ) metallic electrodes, kept at the voltages  $V_S = -V/2$  and  $V_D = +V/2$  respectively, via two tunnel junctions with capacitances  $C_S$  and  $C_D$ . The island is also connected to a gate voltage  $V_g$  by means of the capacitance  $C_g$ . Tunneling events are forbidden through  $C_g$ , meaning that  $V_g$  is used only to control the potential of the island. With  $M_S = 2$  and  $M_J = 1$ , the total energy (A.5) for this system reads

$$E_{\text{SET}}(n) = E_C (n - n_g)^2 + \frac{eV}{C_\Sigma} \left[ n_D \left( C_S + \frac{C_g}{2} \right) - n_S \left( C_D + \frac{C_g}{2} \right) \right] + \tilde{U} . \quad (\text{A.6})$$

Here we introduced the energy  $\tilde{U}$ ,

$$\tilde{U} = \frac{1}{2C_\Sigma} \left[ C_S C_D V^2 + C_S C_g \left( \frac{V}{2} + V_g \right) + C_D C_g \left( \frac{V}{2} - V_g \right) \right] - E_C n_g^2 ,$$

which is independent of  $n$ , the charging energy  $E_C = e^2/2C_\Sigma$ , the gate-induced charge  $n_g = V_g C_g/e$  and the number of tunneled electrons  $n_D$  and  $n_S$  through  $D$  and  $S$  respectively. For a symmetric device,  $C_D = C_S = C$ , Eq.(A.6) gives

$$E_{\text{SET}}(n) = E_C (n - n_g)^2 + \frac{1}{2} eV (n_D - n_S) + \tilde{U}' , \quad (\text{A.7})$$

where  $\tilde{U}'$  is  $\tilde{U}$  with  $C_D = C_S = C$ . From Eq.(A.7), it follows that the energy cost to add (+ $N$ , in) or remove ( $-N$ , out)  $N$  extra-electrons to or from the island is

$$\begin{aligned} E_D^{\text{in/out}}(n, N) &= E_{\text{SET}}^D(n \pm N) - E_{\text{SET}}^D(n) = \\ &= E_C N^2 \pm \frac{1}{2} e V N \pm 2 E_C (n - n_g) N, \end{aligned} \quad (\text{A.8})$$

if the tunneling process occurs through the drain ( $n_D \rightarrow n_D \pm N$ ), and

$$\begin{aligned} E_S^{\text{in/out}}(n, N) &= E_{\text{SET}}^S(n \pm N) - E_{\text{SET}}^S(n) = \\ &= E_C N^2 \mp \frac{1}{2} e V N \pm 2 E_C (n - n_g) N, \end{aligned} \quad (\text{A.9})$$

when the source channel is involved ( $n_S \rightarrow n_S \pm N$ ). The energy costs Eqs.(A.8) and (A.9) determine completely the electronic transport in a single-electron transistor. Since, in real experiments, the main contributions to the charge current through a SET are given by single- and two-particle tunneling processes, below we treat the cases  $N = 1$  and  $N = 2$  in more details.

## A.2.2 Single-electron tunneling

According to Eqs.(A.8) and (A.9), the change of the energy of the island caused by the transfer of one electron ( $N = 1$ ) through the insulating barriers of  $D$  and  $S$  is given by the relations

$$E_D^{\text{in/out}}(n, 1) = E_C \pm \frac{1}{2} e V \pm 2 E_C (n - n_g), \quad (\text{A.10})$$

and

$$E_S^{\text{in/out}}(n, 1) = E_C \mp \frac{1}{2} e V \pm 2 E_C (n - n_g), \quad (\text{A.11})$$

respectively. Tunneling events occur only if the energy of the island is minimized. Namely when the bias voltage  $V = V_D - V_S$  and the gate-induced charge  $n_g$  are such that Eqs. (A.10) and (A.11) are negative. The ensemble of values of the two parameters  $V$  and  $n_g$  which make the charge flow possible depends on the electronic properties of the metallic electrodes as well as of the island.

Let us first consider a SET entirely fabricated using normal metals, i.e., the NININ double junction. Imposing  $E_D^{\text{in/out}}(n, 1) < 0$  and  $E_S^{\text{in/out}}(n, 1) < 0$ , we see that the charge of the island changes by one electron if  $V$  is larger or smaller than

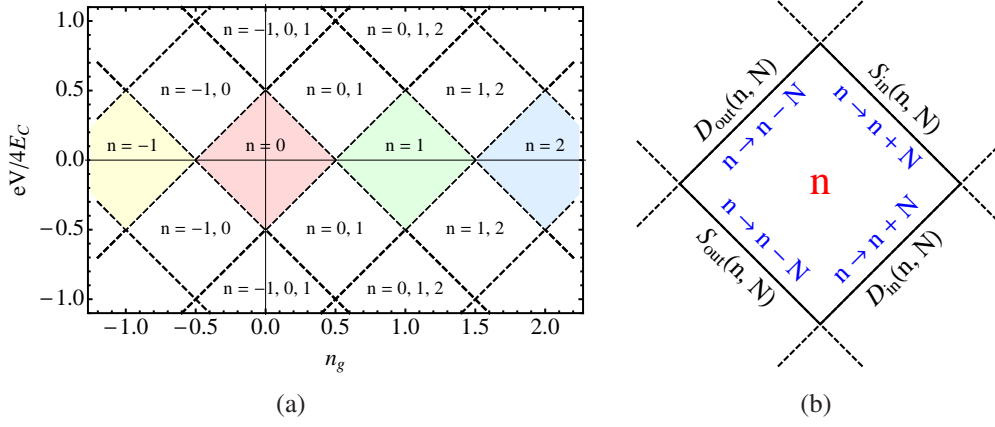


Figure A.2: (a) Coulomb diamonds for a SET with normal-metal electrodes. The stability regions for  $n = -1$ ,  $n = 0$ ,  $n = 1$ , and  $n = 2$  are in yellow, red, green, and blue respectively. The white diamonds are the regions which are unstable for the indicated values of  $n$ . (b) Sketch of a Coulomb diamond for an island with  $n$  electrons. In each side of the diamond are indicated the name of the thresholds (outside) and the increase/decrease of  $n$  (inside). S (source) and D (drain) indicates which electrode of the SET is involved in the tunneling in/out of the island.

the threshold potentials

$$\begin{aligned}
 eV &< eV_{\text{th}}^{D,\text{in}}(n, 1) = 4E_C \left( n_g - n - \frac{1}{2} \right), \\
 eV &> eV_{\text{th}}^{D,\text{out}}(n, 1) = 4E_C \left( n_g - n + \frac{1}{2} \right), \\
 eV &> eV_{\text{th}}^{S,\text{in}}(n, 1) = -4E_C \left( n_g - n - \frac{1}{2} \right), \\
 eV &< eV_{\text{th}}^{S,\text{out}}(n, 1) = -4E_C \left( n_g - n + \frac{1}{2} \right). \quad (\text{A.12})
 \end{aligned}$$

Here the superscript of each voltage indicates which channel is involved in the tunneling, drain ( $D$ ) or source ( $S$ ), and the direction of the transferred electron, going inside (in) or outside (out) the island. For a fixed value of the charge settled on the central electrode,  $Q = -n^*e$ , Eqs. (A.12) are crossing lines in the Cartesian plane  $V$  vs  $n_g$ . The resulting four intersection points are the edges of the so-called Coulomb diamond corresponding to  $n = n^*$ . According to the inequalities Eqs. (A.12), single-electron tunneling is forbidden for the values of  $V$  and  $n_g$  belonging to the area of such a  $n^*$ -diamond. The charge particle can overcome the tunnel barrier only if the bias and gate voltages are outside such a stability region for  $n = n^*$ . Figure A.2(a) shows the Coulomb diamonds for different values of  $n$ .

We see that the  $n$ -diamond shares only one point with the  $n \pm 1$ -diamond. Such a common value results from the crossing of four threshold lines occurring when  $V = 0$  and  $n_g = n \pm 1/2$ . As a result, the one-electron tunneling can be controlled by means of the gate voltage  $V_g$ . However, since  $V = 0$ , the direction of the corresponding single-particle current is random and its time average is zero, as it can be seen with the help of Fig. A.2(b). In other words, if  $n_g$  oscillates in time with the frequency  $f$ , the resulting current through the normal-metal transistor is non-synchronized with the variation of the gate voltage  $V_g$  and even almost frequency independent [1, 33]. As a result, the control of the single-electron tunneling becomes a difficult task. On the other hand, considering  $V \neq 0$  fixed and changing  $n_g$  in such a way that the system goes from the  $n$ -diamond to the  $n \pm 1$ -diamond, the instability regions where more than one value of  $n$  become accessible and an uncontrolled single- or multi-electron current can flow through the NININ SET. The increase of the number of islands and voltage gates helps to overcome this problem, but the system becomes more complex and more difficult to control [9, 27].

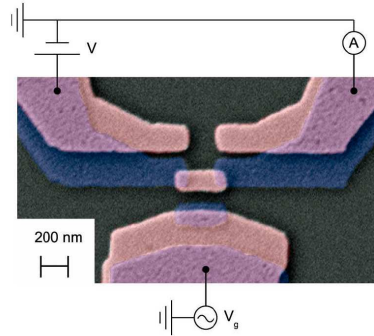


Figure A.3: Scanning electron micrograph of a SINIS turnstile [9].

When superconducting materials are used in the fabrication of the SET, a single-island device can sustain a single-electron current [9]. Excluding a double tunnel junction device completely superconducting, SISIS, where the Cooper-pair current represents an unavoidable and relevant source of error, we focus here on the hybrid SINIS structure of Fig. 2.1 where single-electron transport is usually dominant. Figure A.3 shows an image of the SINIS device used in Ref. [9].

Since tunneling events occurs only if the energy gap  $\Delta$  of the superconductor(s) is overcome, the transfer of charge inside or outside the island is energetically favorable for  $E_D^{\text{in/out}}(n, 1) < -\Delta$  and  $E_S^{\text{in/out}}(n, 1) < -\Delta$ . Then, in this case,

the threshold voltages reads

$$\begin{aligned}
eV < eV_{\text{th,SC}}^{D,\text{in}}(n, 1) &= 4E_C \left( n_g - n - \frac{1}{2} \right) - 2\Delta, \\
eV > eV_{\text{th,SC}}^{D,\text{out}}(n, 1) &= 4E_C \left( n_g - n + \frac{1}{2} \right) + 2\Delta, \\
eV > eV_{\text{th,SC}}^{S,\text{in}}(n, 1) &= -4E_C \left( n_g - n - \frac{1}{2} \right) + 2\Delta, \\
eV < eV_{\text{th,SC}}^{S,\text{out}}(n, 1) &= -4E_C \left( n_g - n + \frac{1}{2} \right) - 2\Delta. \tag{A.13}
\end{aligned}$$

Figure A.4 shows the Coulomb diamonds arising from Eqs. (A.13). In comparison with Fig. A.2(a), the stability regions are wider and overlap. In the overlapping region, two different charge state are stable. Its area decreases as the charging energy is increased and it reduces to a single point as in Fig. A.2(a) in the limit  $E_C \gg \Delta$ , i.e., when the superconducting gap becomes irrelevant.

### A.2.3 Two-electron tunneling

When two electrons per unit of time,  $N = 2$ , enter or leave the central electrode of a SET through one of the two insulating barriers, the change of energy of the island, according to Eqs.(A.8) and (A.9), reads

$$E_D^{\text{in/out}}(n, 2) = 4E_C \pm eV \pm 4E_C(n - n_g), \tag{A.14}$$

or

$$E_S^{\text{in/out}}(n, 2) = 4E_C \mp eV \pm 4E_C(n - n_g), \tag{A.15}$$

depending on which side of the SET is involved, the drain  $D$  with  $V_D = V/2$  or the source  $S$  with  $V_S = -V/2$  respectively. Like the single-electron case discussed in the previous section, imposing that Eqs. (A.14) and (A.15) are negative, we obtain the threshold conditions and voltages

$$\begin{aligned}
eV < eV_{\text{th}}^{D,\text{in}}(n, 2) &= 4E_C(n_g - n - 1), \\
eV > eV_{\text{th}}^{D,\text{out}}(n, 2) &= 4E_C(n_g - n + 1), \\
eV > eV_{\text{th}}^{S,\text{in}}(n, 2) &= -4E_C(n_g - n - 1), \\
eV < eV_{\text{th}}^{S,\text{out}}(n, 2) &= -4E_C(n_g - n + 1), \tag{A.16}
\end{aligned}$$

which define the Coulomb diamonds or stability regions, upon changing the number of extra electrons  $n$ , when the two-electron tunneling can occur. Equations

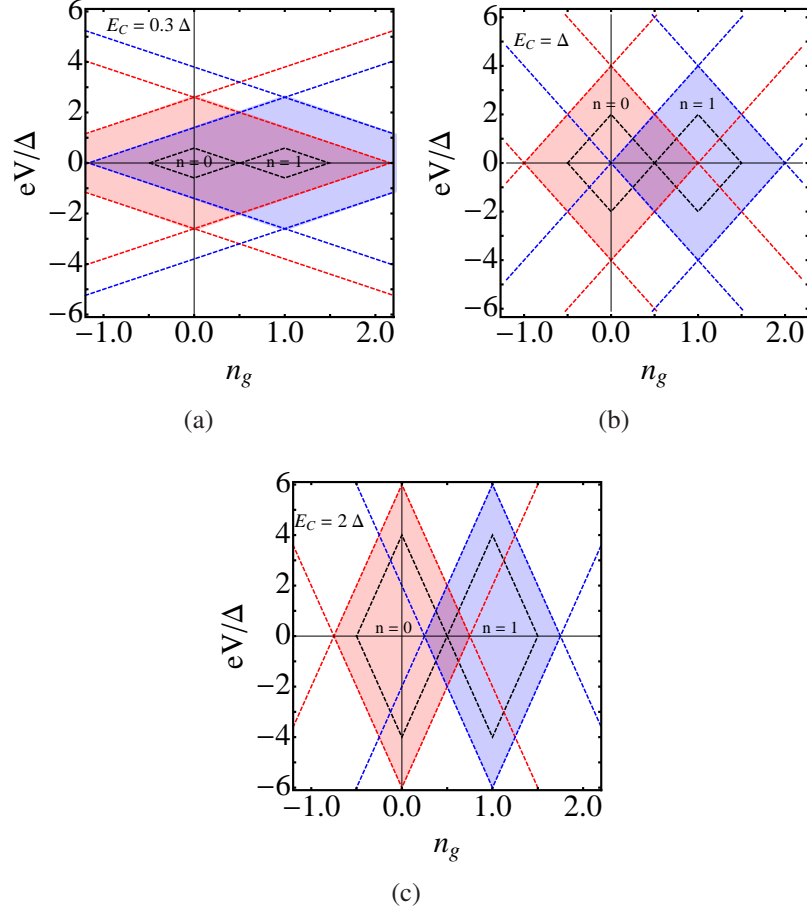


Figure A.4: Coulomb diamonds for a SINIS hybrid SET with (a)  $E_C = 0.3\Delta$ , (b)  $E_C = \Delta$ , and (c)  $E_C = 2\Delta$ . Note that increasing the charging energy  $E_C$  the diamonds become thinner along  $n_g$  and larger along  $eV/\Delta$ .

(A.16) hold for both the normal, NININ, and the hybrid, SINIS, structures. Indeed, the energy cost for the two-particle tunneling process between a normal metal and a superconductor, the so-called Andreev reflection, does not depend on the superconducting energy gap  $\Delta$ .

To analyze in details the interplay between single- and two-particle tunneling events, we focus here again on the SINIS turnstile. How relevant can be the Andreev reflection in the determination of the total current flowing through this superconducting device strongly depends on the ratio between the charging energy  $E_C$  and  $\Delta$ . Let us start by considering  $E_C < \Delta$ . In this regime, the Andreev-tunneling diamonds are smaller than the single-electron ones [see Fig. A.5(a)]. For the optimal bias voltage  $eV \simeq \Delta$ , the Andreev reflection always affects the

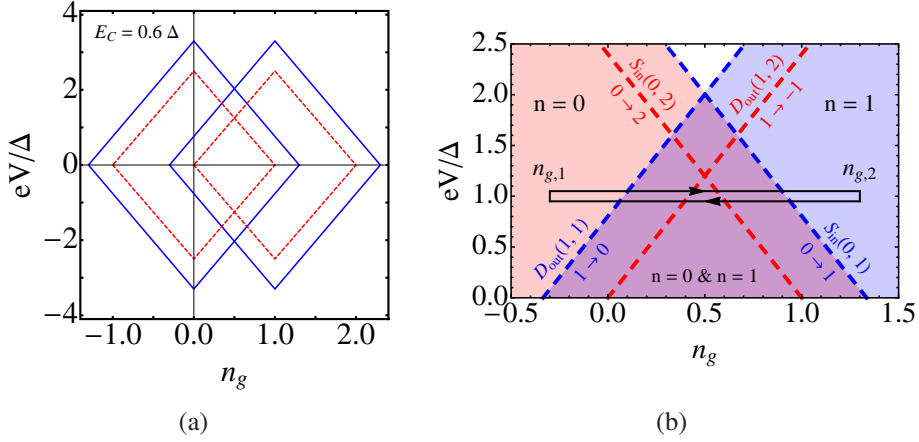


Figure A.5: Coulomb diamonds for one- (blue solid line) and two-electrons (red dashed line) tunnel processes in an SINIS hybrid SET. (a) When  $E_C < \Delta$  the threshold for the single-particle tunneling is crossed before the two-particle one. (b) On the contrary, for  $E_C > \Delta$  Andreev reflection occurs before the quasi-particle tunneling.

single-electron current. A loop crossing the two single-electron thresholds and passing over the overlapping region, like the one shown in Fig. A.5(b), inevitably touches the Andreev lines as well. Although these two-particle tunneling thresholds could be avoided in the limit  $E_C \ll \Delta$ , under this condition in the overlapping region also the charge states with  $n \neq 0, 1$  would be stable, and consequently the possibility to have only the single-electron tunneling would be compromised. Going back to the loop of Fig. A.5(b), we see that in the forward direction (increasing  $n_g$ ) the threshold  $0 \rightarrow 2$  is crossed before  $0 \rightarrow 1$ . As a result, the probability that the charge of the island goes from 0 to 1 before  $n_{g,2}$  is different from zero. A similar situation occurs when  $n_g$  is driven backward (decrease of  $n_g$ ), namely the  $1 \rightarrow 0$  transition can take place when the loop overcomes the Andreev line  $1 \rightarrow -1$  rather than the single-particle one.

On the other hand, for  $E_C > \Delta$  the two-particle tunneling stability regions contain the diamonds determined by Eqs. (A.13) [see Fig. A.6(a)]. In this case, we can have two possible loops for  $eV \simeq \Delta$ , as shown in Fig. A.6(b). We first consider L1. Increasing the induced gate charge starting from  $n_{g,1} > 0$  and with  $n = 0$ , we observe that the  $0 \rightarrow 1$  transition occurs before the two-electron one  $0 \rightarrow 2$ . In principle, Andreev reflection is suppressed. However, if the tunneling of one electron into the island through the source junction is slower than the time needed for  $n_g(t)$  to reach the  $0 \rightarrow 2$  threshold, then the localized charge can become  $-2e$ , rather than  $-1e$ . Eventually, this can affect the total current flowing

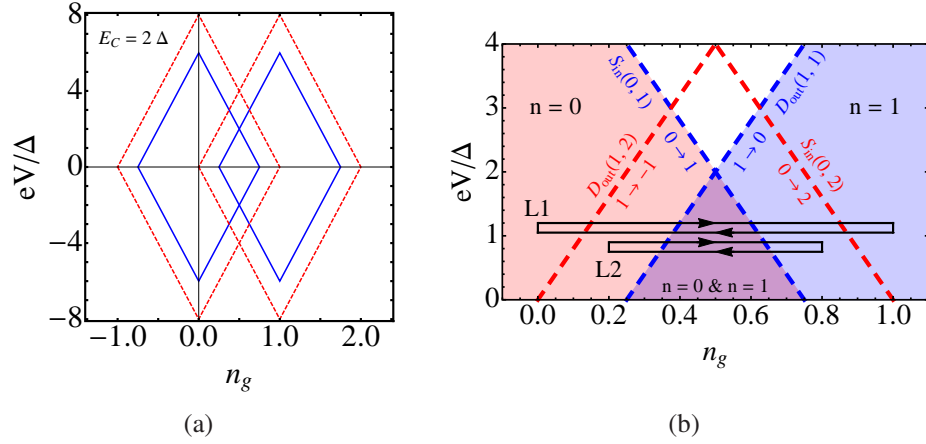


Figure A.6: Coulomb diamonds for one- (blue solid line) and two-electrons (red dashed line) tunnel processes in an SINIS hybrid SET. (a) When  $E_C < \Delta$  the threshold for the single-particle tunneling is crossed before the two-particle one. (b) On the contrary, for  $E_C > \Delta$  Andreev reflection occurs before the quasi-particle tunneling.

through the SINIS. Indeed, one of the two added electrons can go out through the drain even before going back to  $n_{g,1}$  because at  $n_{g,2}$  the charge state  $n = 2$  is unstable. Decreasing  $n_g$  from  $n_{g,2}$  to  $n_{g,1}$ , similar tunneling events occur. As a result, the maximum value of the frequency of the oscillating voltage gate  $V_g(t)$  and consequently the maximum amplitude of the total current  $I = ef$  can be limited by the tunneling time. In other words, for L1 the control of the single-electron tunneling can be tough. To overcome these issues, it is convenient to consider the loop L2 of Fig. A.6(b) where the Andreev-tunneling thresholds are avoided. Indeed, in this case, one expects to have an efficient single-electron hybrid turnstile where Andreev reflection can be suppressed.

## Caldeira-Legget Model and Fluctuation-Dissipation Theorem

According to the Caldeira-Legget model, the impedance  $Z(\omega)$  of an electric circuit can be modeled as an ensemble of infinite quantum harmonic LC oscillators with Hamiltonian

$$\hat{H}_{\text{env}} = \sum_{\lambda} \left[ \frac{\hat{Q}_{\lambda}^2}{2C_{\lambda}} + \frac{1}{2} C_{\lambda} \omega_{\lambda}^2 \left( \frac{\hbar}{e} \hat{\phi}_{\lambda} \right)^2 \right].$$

The charge  $\hat{Q}_{\lambda}$  and phase  $(\hbar/e)\hat{\phi}_{\lambda}$  operators play the role of the momentum and position respectively of the particle/oscillator  $\lambda$  with mass  $C_{\lambda}$  and characteristic frequency  $\omega_{\lambda}^2 = 1/L_{\lambda}C_{\lambda}$ . Each oscillator  $\lambda$  of the ensemble/environment affects both the charge  $\hat{Q}$  and phase  $\hat{\phi}$  of the circuit. In particular, the total phase fluctuation  $\hat{\phi}_{\text{env}}$  of  $\hat{\phi}$  due to  $Z(\omega)$  is given by the superposition of all the phases of the oscillators of the environment, i.e.,  $\hat{\phi}_{\text{env}} = \sum_{\lambda} \hat{\phi}_{\lambda}$ . Since  $\hat{\phi}_{\lambda}$  is the position operator of an harmonic oscillator,  $\hat{\phi}_{\text{env}}$  can be written as

$$\hat{\phi}_{\text{env}} = \sum_{\lambda} \rho_{\lambda} \left( \hat{c}_{\lambda}^{\dagger} + \hat{c}_{\lambda} \right), \quad (\text{B.1})$$

in terms of the creation  $\hat{c}_{\lambda}^{\dagger}$  and annihilation  $\hat{c}_{\lambda}$  operators of one photon. In Eq. (B.1), we introduced the coupling term  $\rho_{\lambda} = (e/\hbar)\sqrt{\hbar/2C_{\lambda}\omega_{\lambda}}$ . In the Heisenberg picture,  $\hat{\phi}_{\text{env}}$  depends explicitly on time, with  $\hat{c}_{\lambda}^{\dagger}(t) = e^{+i\omega_{\lambda}t} \hat{c}_{\lambda}^{\dagger}$  and  $\hat{c}_{\lambda}(t) = e^{-i\omega_{\lambda}t} \hat{c}_{\lambda}$ . The first time-derivative of Eq. (B.1) gives the fluctuating voltage operator

$$\hat{V}_{\text{env}}(t) = \frac{\hbar}{e} \frac{d\hat{\phi}_{\text{env}}(t)}{dt} = \frac{\hbar}{e} \sum_{\lambda} \rho_{\lambda} i\omega_{\lambda} \left[ \hat{c}_{\lambda}^{\dagger}(t) - \hat{c}_{\lambda}(t) \right], \quad (\text{B.2})$$

whose mean value over the eigenstates of  $\hat{H}_{\text{env}}$  is zero. On the other hand, the voltage-voltage correlation function  $\delta\hat{V}_{\text{env}}(t,0) = \langle \{ \hat{V}_{\text{env}}(t), \hat{V}_{\text{env}}(0) \} \rangle$  is

$$\delta\hat{V}_{\text{env}}(t,0) = \left( \frac{\hbar}{e} \right)^2 \sum_{\lambda\lambda'} \rho_{\lambda} \rho_{\lambda'} (i\omega_{\lambda}) (i\omega_{\lambda'}) C_{\lambda}(t,0), \quad (\text{B.3})$$

with

$$C_\lambda(t, 0) \equiv \left\langle \left\{ \left[ \hat{c}_\lambda^\dagger(t) - \hat{c}_\lambda(t) \right], \left[ \hat{c}_\lambda^\dagger(0) - \hat{c}_\lambda(0) \right] \right\} \right\rangle. \quad (\text{B.4})$$

The symbols  $\{, \}$  and  $\langle \dots \rangle$  in Eq. (B.4) indicate the anti-commutator and quantum mean value over the eigenstates of  $\hat{H}_{\text{env}}$  respectively. Assuming that the number of photons of the environment is infinite, the terms in Eq. (B.3) which create or destroy more than one photon can be neglected. Consequently, the correlation function  $\delta\hat{V}_{\text{env}}(t, 0)$  becomes

$$\delta\hat{V}_{\text{env}}(t, 0) \simeq \left( \frac{\hbar}{e} \right)^2 \sum_\lambda \rho_\lambda^2 \omega_\lambda^2 (e^{i\omega_\lambda t} + e^{-i\omega_\lambda t}) (1 + 2n_\lambda), \quad (\text{B.5})$$

where  $n_\lambda$  is the mean value of photons with frequency  $\omega_\lambda$ ;  $T_{\text{env}}$  is the temperature of the environment. The Fourier transform of Eq. (B.5) gives the spectral density function of the thermal bath,

$$\begin{aligned} [\delta\hat{V}_{\text{env}}(t, 0)]_\omega &\simeq \left( \frac{\hbar}{e} \right)^2 \sum_\lambda \rho_\lambda^2 \omega_\lambda^2 \coth \left( \frac{1}{2} \frac{\hbar\omega_\lambda}{k_B T_{\text{env}}} \right) \\ &\times 2\pi [\delta(\omega - \omega_\lambda) + \delta(\omega + \omega_\lambda)]. \end{aligned} \quad (\text{B.6})$$

To obtain Eq. (B.6) we assumed that  $n_\lambda$  is given by the Bose-Einstein distribution function  $n_{BE}(\omega_\lambda) = [\exp(\hbar\omega_\lambda/k_B T_{\text{env}}) - 1]^{-1}$  which satisfies the relation  $1 + 2n_{BE}(x) = \coth(x/2)$ .

On the other hand, the Fourier-transformed correlation function  $[\delta\hat{V}_{\text{env}}(t, 0)]_\omega$  satisfies the quantum fluctuation-dissipation relation

$$[\delta\hat{V}_{\text{env}}(t, 0)]_\omega = 2\hbar\omega \Re[Z(\omega)] \coth \left( \frac{1}{2} \frac{\hbar\omega}{k_B T} \right). \quad (\text{B.7})$$

Comparing Eq. (B.6) with Eq. (B.7), we finally get the expression

$$\Re[Z(\omega)] = \frac{R_K}{2} \sum_\lambda \rho_\lambda^2 \omega_\lambda [\delta(\omega - \omega_\lambda) + \delta(\omega + \omega_\lambda)], \quad (\text{B.8})$$

which allows to relate the macroscopic impedance  $Z(\omega)$  with the microscopic quantities characterizing the environment.

# Current and Heat Peak in a $S_1IS_2$ Josephson Junction

## Introduction

In this appendix we show how to estimate the charge and heat currents flowing through a  $S_1IS_2$  Josephson junction with energy gaps  $\Delta_1$  and  $\Delta_2 > \Delta_1$  when the bias voltage is equal to  $(\Delta_2 - \Delta_1)/e$ , i.e., we derive the optimal current  $I_{12,opt}$ , Eq. (3.9), and the corresponding cooling power  $\dot{Q}_{12,opt} \approx \Delta_1(I_{12,opt}/e)$ .

## C.1 Current peak

We start by considering Eq. (3.7). Rescaling the energy variable  $E$  with  $\Delta_1$  and imposing that  $eV_2 = \Delta_2 - \Delta_1$ , we get

$$I_{12,opt} = \frac{\Delta_1}{eR_2} \int_{-\infty}^{+\infty} dx N_1(x) N_2\left(x - \frac{\varepsilon}{\Delta_1}\right) \left[ f_2\left(x - \frac{\varepsilon}{\Delta_1}\right) - f_1(x) \right], \quad (C.1)$$

where we introduced the new variable  $x = E/\Delta_1$  and the energy difference  $\varepsilon = \Delta_2 - \Delta_1$ . The BCS density of states in Eq. (C.1) are

$$N_1(x) = \frac{|x|}{\sqrt{x^2 - 1}}, \quad N_2\left(x - \frac{\varepsilon}{\Delta_1}\right) = \frac{\left|x - \frac{\varepsilon}{\Delta_1}\right|}{\sqrt{\left(x - \frac{\varepsilon}{\Delta_1}\right)^2 - \left(\frac{\Delta_2}{\Delta_1}\right)^2}}, \quad (C.2)$$

and the Fermi-Dirac distribution functions read

$$f_1(x) = \left[ e^{(\Delta_1/k_B T_1)x} + 1 \right]^{-1}, \quad f_2\left(x - \frac{\varepsilon}{\Delta_1}\right) = \left[ e^{(\Delta_1/k_B T_2)(x - \varepsilon/\Delta_1)} + 1 \right]^{-1}. \quad (C.3)$$

Figure C.1 shows the plots of Eqs. (C.2) and (C.3) as well as the product  $N_1(x) N_2(x - \varepsilon/\Delta_1)$  and the difference  $f_2(x - \varepsilon/\Delta_1) - f_1(x)$ . In particular, we see from

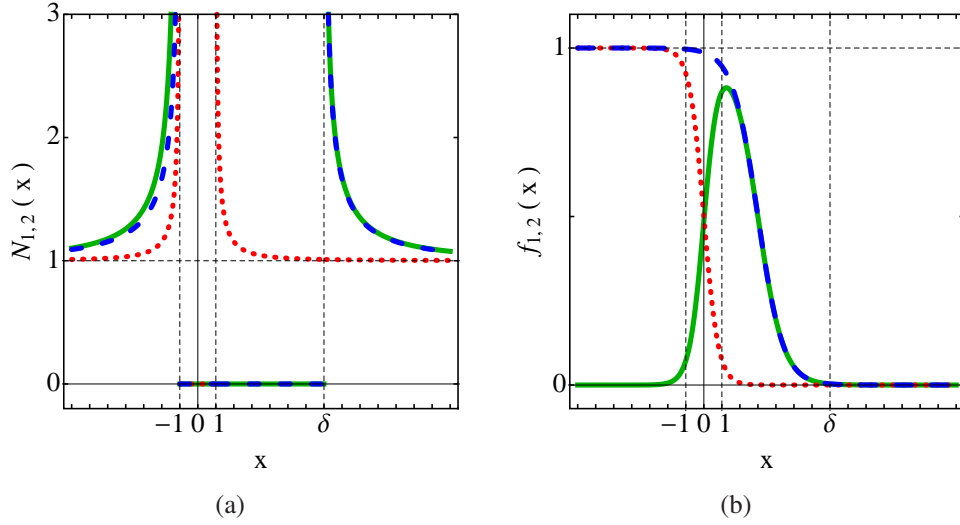


Figure C.1: (a) Plot of the density of states Eqs. (C.2):  $N_1(x)$  (red dotted line) and  $N_2(x - \varepsilon/\Delta_1)$  (blue dashed line). It is also shown their product,  $N_1(x)N_2(x - \varepsilon/\Delta_1)$  (green solid line). (b) Plot of the Fermi-Dirac distribution functions Eqs. (C.3):  $f_1(x)$  (red dotted line) and  $f_2(x - \varepsilon/\Delta_1)$  (blue dashed line). The green solid line is the difference  $f_2(x - \varepsilon/\Delta_1) - f_1(x)$ . In both panels  $\delta = 2(\Delta_2/\Delta_1) - 1$ .

Fig. C.1(a) that the integral Eq. (C.1) can be different from zero only when  $x \leq -1$  and  $x \geq \delta \equiv 2(\Delta_2/\Delta_1) - 1$ . As a result, the current at the peak can be written as

$$\begin{aligned} I_{12,opt} &= I_{12,opt}^{<0} + I_{12,opt}^{>0} \\ &= \frac{\Delta_1}{eR_2} \int_{-\infty}^{-1} dx \dots + \frac{\Delta_1}{eR_2} \int_{\delta}^{+\infty} dx \dots, \end{aligned} \quad (\text{C.4})$$

i.e., the sum of two integrals,  $I_{12,opt}^{<0}$  and  $I_{12,opt}^{>0}$ , involving negative and positive values of  $x$  respectively.

### C.1.1 Positive energies

Let us first consider  $I_{12,opt}^{>0}$ . Assuming that  $N_1(x) \approx 1$  when  $x \geq \delta$ , namely the ratio  $\Delta_2/\Delta_1$  is large enough,<sup>1</sup> and that the temperatures are small,  $k_B T_1 \leq k_B T_2 < \Delta_1$ , then one finds

$$I_{12,opt}^{>0} \simeq \frac{\Delta_1}{eR_2} \int_{\delta}^{+\infty} dx N_2\left(x - \frac{\varepsilon}{\Delta_1}\right) \left[ e^{-(\Delta_1/k_B T_2)(x - \varepsilon/\Delta_1)} - e^{-(\Delta_1/k_B T_1)x} \right]. \quad (\text{C.5})$$

<sup>1</sup>this approximation is valid, for instance, when S<sub>2</sub> is Vanadium and S<sub>1</sub> is Aluminum with  $\Delta_2/\Delta_1 \approx 4$ .

We see that only the exponentially-decaying tails of the Fermi functions (C.3) contribute to the current Eq. (C.5). It follows that the order of magnitude of the integral  $I_{12,opt}^{>0}$  is determined by the divergence of  $N_2[x - (\varepsilon/\Delta_1)]$  occurring for  $x = \delta$  [see Fig. C.1(a)]. Then, Eq. (C.5) can be written as

$$I_{12,opt}^{>0} \simeq \frac{\Delta_1}{eR_2} \sqrt{\frac{\Delta_2}{2\Delta_1}} \int_{\delta}^{+\infty} dx \frac{1}{\sqrt{x-\delta}} \left[ e^{-(\Delta_1/k_B T_2)(x-\varepsilon/\Delta_1)} - e^{-(\Delta_1/k_B T_1)x} \right], \quad (\text{C.6})$$

using the approximation  $\sqrt{x^2 - a^2} \approx \sqrt{2a}\sqrt{x-a}$ . The integral Eq. (C.6) can be calculated by means of the formula

$$\int_a^{+\infty} dx \frac{e^{-bx}}{\sqrt{x-a}} = \sqrt{\frac{\pi}{b}} e^{-ab}.$$

We finally obtain the current

$$I_{12,opt}^{>0} \approx \frac{\Delta_1}{eR_2} \sqrt{\frac{\pi}{2}} \sqrt{\frac{\Delta_2}{\Delta_1}} \left[ e^{-(\Delta_1/k_B T_2)(\Delta_2/\Delta_1)} \sqrt{\frac{k_B T_2}{\Delta_1}} - e^{-(\Delta_1/k_B T_1)\delta} \sqrt{\frac{k_B T_1}{\Delta_1}} \right]. \quad (\text{C.7})$$

## C.1.2 Negative energies

We now estimate  $I_{12,opt}^{<0}$ . Let us take into account the actual smearing of the density of states by shifting Eqs. (C.2) by the Dynes parameters  $\gamma_{1,2} \ll 1$ ,

$$N_1^s(x) = \frac{|x - \gamma_1|}{\sqrt{(x - \gamma_1)^2 - 1}}, \quad N_2^s\left(x - \frac{\varepsilon}{\Delta_1}\right) = \frac{\left|x - \frac{\varepsilon}{\Delta_1} - \gamma_2\right|}{\sqrt{\left(x - \frac{\varepsilon}{\Delta_1} - \gamma_2\right)^2 - \left(\frac{\Delta_2}{\Delta_1}\right)^2}}. \quad (\text{C.8})$$

As for the derivation of Eq. (C.6), if  $k_B T_1 \leq k_B T_2 < \Delta_1$  we can use the approximation  $\sqrt{x^2 - a^2} \approx \sqrt{2a}\sqrt{x-a}$  because the Fermi-Dirac functions Eqs. (C.3) provide

an exponential decay to  $I_{12,opt}^{<0}$  with the increasing of  $|x|$ . As a result, we can write

$$\begin{aligned}
I_{12,opt}^{<0} &\approx \frac{\Delta_1}{eR_2} \int_{-\infty}^{-1} dx \frac{|-1-\gamma_1|}{\sqrt{-1-\gamma_1-1}} \frac{1}{\sqrt{x-\gamma_1+1}} \\
&\times \frac{\left| -1 - \frac{\varepsilon}{\Delta_1} - \gamma_2 \right|}{\sqrt{-1 - \frac{\varepsilon}{\Delta_1} - \gamma_2 - \frac{\Delta_2}{\Delta_1}}} \frac{1}{\sqrt{x - \frac{\varepsilon}{\Delta_1} - \gamma_2 + \frac{\Delta_2}{\Delta_1}}} \\
&\times \left[ 1 - e^{(\Delta_1/k_B T_2)(x-\varepsilon/\Delta_1)} - 1 + e^{(\Delta_1/k_B T_1)x} \right] \\
&= \frac{\Delta_1}{eR_2} \int_{-\infty}^{-1} dx \frac{1}{\sqrt{-2}} \frac{1}{\sqrt{x+1-\gamma_1}} \frac{\left| -\frac{\Delta_2}{\Delta_1} - \gamma_2 \right|}{\sqrt{-2\frac{\Delta_2}{\Delta_1} - \gamma_2}} \frac{1}{\sqrt{x+1-\gamma_2}} \\
&\times \left[ e^{(\Delta_1/k_B T_1)x} - e^{(\Delta_1/k_B T_2)(x-\varepsilon/\Delta_1)} \right] \\
&= \frac{\Delta_1}{eR_2} \frac{1}{\sqrt{2}} \sqrt{\frac{\Delta_2}{2\Delta_1}} \int_1^{+\infty} dx \frac{1}{\sqrt{x-1+\gamma_1}} \frac{1}{\sqrt{x-1+\gamma_2}} \\
&\times \left[ e^{-(\Delta_1/k_B T_1)x} - e^{-(\Delta_1/k_B T_2)(x+\varepsilon/\Delta_1)} \right]. \tag{C.9}
\end{aligned}$$

The integral Eq. (C.9) is of the form

$$\int_1^{+\infty} dx \frac{e^{-cx}}{\sqrt{x-a}\sqrt{x-b}} = A + B \tag{C.10}$$

where

$$A = -e^{-c} \ln \left[ 2 - (a+b) + 2\sqrt{ab+1-(a+b)} \right] \tag{C.11}$$

$$B = c \int_1^{+\infty} dx e^{-cx} \ln \left[ 2x - (a+b) + 2\sqrt{x^2 - (a+b)x + ab} \right] \tag{C.12}$$

are obtained integrating by parts. A further integration by parts of Eq. (C.12) allows to write  $B = B_1 + B_2$  with

$$\begin{aligned}
B_1 &= c e^{-c} \left\{ -\sqrt{ab+1-(a+b)} + \left[ 1 - \frac{1}{2}(a+b) \right] \right. \\
&\times \left. \ln \left[ 2 - (a+b) + 2\sqrt{ab+1-(a+b)} \right] \right\} \tag{C.13}
\end{aligned}$$

$$\begin{aligned}
B_2 &= c^2 \int_1^{+\infty} dx e^{-cx} \left\{ -\sqrt{x^2 - (a+b)x + ab} + \left[ x - \frac{1}{2}(a+b) \right] \right. \\
&\times \left. \ln \left[ 2x - (a+b) + 2\sqrt{x^2 - (a+b)x + ab} \right] \right\}. \tag{C.14}
\end{aligned}$$

In other words,  $A$  and  $B_1$  are first and second order terms of the series expansion of Eq. (C.10). Imposing that  $a = 1 - \gamma_1$  and  $b = 1 - \gamma_2$ , Eqs. (C.11) and (C.13) become

$$\begin{aligned} A &= -e^{-c} \ln(\gamma_1 + \gamma_2 + 2\sqrt{\gamma_1\gamma_2}) \\ B_1 &= c e^{-c} \left[ -\sqrt{\gamma_1\gamma_2} + \frac{1}{2}(\gamma_1 + \gamma_2) \ln(\gamma_1 + \gamma_2 + 2\sqrt{\gamma_1\gamma_2}) \right] \\ &\approx c e^{-c} \frac{1}{2}(\gamma_1 + \gamma_2) \ln(\gamma_1 + \gamma_2 + 2\sqrt{\gamma_1\gamma_2}) . \end{aligned} \quad (\text{C.15})$$

Their ratio,

$$\frac{|A|}{|B_1|} \approx \frac{2}{c(\gamma_1 + \gamma_2)} \sim \frac{1}{\gamma_1 + \gamma_2} \gg 1$$

is much larger than 1 because the Dynes parameters  $\gamma_{1,2} \ll 1$ . It turns out that  $A$ , Eq. (C.15), is the leading term and Eq. (C.9) can be written as

$$\begin{aligned} I_{12,opt}^{<0} &\approx \frac{\Delta_1}{eR_2} \frac{1}{2} \sqrt{\frac{\Delta_2}{\Delta_1}} \left[ e^{-\Delta_1/k_B T_1} - e^{-(\Delta_1/k_B T_2)(\Delta_2/\Delta_1)} \right] \\ &\times \left[ -\ln(\gamma_1 + \gamma_2 + 2\sqrt{\gamma_1\gamma_2}) \right] . \end{aligned} \quad (\text{C.16})$$

### C.1.3 Total charge current

The total charge current is given by the sum of Eqs. (C.7) and (C.16). However, the leading term is  $I_{12,opt}^{<0}$  because of its logarithmic dependence on  $\gamma_{1,2} \ll 1$ . Assuming  $\Delta_2/\Delta_1 > T_2/T_1 > 1$ , then we find

$$\begin{aligned} I_{12,opt} \approx I_{12,opt}^{<0} &\approx \frac{\Delta_1}{eR_2} \frac{1}{2} \sqrt{\frac{\Delta_2}{\Delta_1}} e^{-\Delta_1/k_B T_1} \left[ -\ln(\gamma_1 + \gamma_2 + 2\sqrt{\gamma_1\gamma_2}) \right] \\ &= -\frac{\Delta_1}{eR_2} \frac{1}{2} \sqrt{\frac{\Delta_2}{\Delta_1}} e^{-\Delta_1/k_B T_1} \ln \left[ (\sqrt{\gamma_1} + \sqrt{\gamma_2})^2 \right] \\ &= -\frac{\sqrt{\Delta_1\Delta_2}}{eR_2} e^{-\Delta_1/k_B T_1} \ln(\sqrt{\gamma_1} + \sqrt{\gamma_2}) . \end{aligned}$$

## C.2 Heat peak

We consider now the heat Eq. (3.8). We write it in terms of the dimensionless variable  $x = E/\Delta_1$  and evaluate it for  $eV_2 = \Delta_2 - \Delta_1$ :

$$\dot{Q}_{12,opt} = \frac{\Delta_1^2}{e^2 R_2} \int_{-\infty}^{+\infty} dx x N_1(x) N_2\left(x - \frac{\varepsilon}{\Delta_1}\right) \left[ f_1(x) - f_2\left(x - \frac{\varepsilon}{\Delta_1}\right) \right]. \quad (\text{C.17})$$

As for Eq. (C.1), the functions  $N_1(x)$ ,  $N_2(x - \varepsilon/\Delta_1)$ ,  $f_1(x)$  and  $f_2(x - \varepsilon/\Delta_1)$  are given by Eqs. (C.2) and (C.3). Due to the trend of the densities of states of S<sub>1</sub> and S<sub>2</sub>, see Fig. C.1(a), the heat current Eq. (C.17) is the sum of two contributions,

$$\begin{aligned} \dot{Q}_{12,opt} &= \dot{Q}_{12,opt}^{<0} + \dot{Q}_{12,opt}^{>0} \\ &= \frac{\Delta_1^2}{e^2 R_2} \int_{-\infty}^{-1} dx \dots + \frac{\Delta_1^2}{e^2 R_2} \int_{\delta}^{+\infty} dx \dots, \end{aligned} \quad (\text{C.18})$$

which involve negative and positive energies. Proceeding as in the previous section, we estimate  $\dot{Q}_{12,opt}^{>0}$  and  $\dot{Q}_{12,opt}^{<0}$  to be

$$\begin{aligned} \dot{Q}_{12,opt}^{>0} &\approx \frac{\Delta_1^2}{e^2 R_2} \sqrt{\frac{\pi}{2}} \sqrt{\frac{\Delta_2}{\Delta_1}} \left\{ \left[ \frac{1}{2} \frac{k_B T_1}{\Delta_1} + \delta \right] e^{-(\Delta_1/k_B T_1)\delta} \sqrt{\frac{k_B T_1}{\Delta_1}} \right. \\ &\quad \left. - \left[ \frac{1}{2} \frac{k_B T_2}{\Delta_1} + \delta \right] e^{-(\Delta_1/k_B T_2)(\Delta_2/\Delta_1)} \sqrt{\frac{k_B T_2}{\Delta_1}} \right\}, \end{aligned} \quad (\text{C.19})$$

and

$$\begin{aligned} \dot{Q}_{12,opt}^{<0} &\approx \frac{\Delta_1^2}{e^2 R_2} \frac{1}{2} \sqrt{\frac{\Delta_2}{\Delta_1}} \left[ e^{-\Delta_1/k_B T_1} - e^{-(\Delta_1/k_B T_2)(\Delta_2/\Delta_1)} \right] \\ &\quad \times \left[ -\sqrt{\gamma_1 \gamma_2} - \ln(\gamma_1 + \gamma_2 + 2\sqrt{\gamma_1 \gamma_2}) \right]. \end{aligned} \quad (\text{C.20})$$

We obtained Eqs. (C.19) and (C.20) by means of the formulas

$$\int_a^{+\infty} dx \frac{x e^{-bx}}{\sqrt{x-a}} = \left( \frac{1}{2b} + a \right) e^{-ab} \sqrt{\frac{\pi}{b}},$$

and

$$\int_1^{+\infty} dx \frac{x e^{-cx}}{\sqrt{x-a}\sqrt{x-b}} \simeq A + B_1,$$

with

$$\begin{aligned}
A &= -e^{-c} \left\{ \sqrt{(1-a)(1-b)} + (a+b) \ln \left[ \sqrt{1-a} + \sqrt{1-b} \right] \right\} \\
&= -e^{-c} \left\{ \sqrt{\gamma_1 \gamma_2} + (2 - \gamma_1 - \gamma_2) \ln (\sqrt{\gamma_1} + \sqrt{\gamma_2}) \right\} \\
B_1 &= -c e^{-c} \frac{1}{4} \left\{ (-3a - 3b + 2) \sqrt{(1-a)(1-b)} \right. \\
&\quad \left. + (-3a^2 - 3b^2 - 2ab + 4a + 4b) \ln \left[ \sqrt{1-a} + \sqrt{1-b} \right] \right\} \\
&\simeq -c e^{-c} \frac{1}{4} \left\{ (-4 + 3\gamma_1 + 3\gamma_2) \sqrt{\gamma_1 \gamma_2} + 4(\gamma_1 + \gamma_2) \ln (\sqrt{\gamma_1} + \sqrt{\gamma_2}) \right\},
\end{aligned}$$

respectively. Comparing Eqs. (C.19) and (C.20), we see that the total heat current  $\dot{Q}_{12,opt}$  is determined by  $\dot{Q}_{12,opt}^{<0}$ . If  $\Delta_2/\Delta_1 > T_2/T_1 > 1$ , we finally find

$$\begin{aligned}
\dot{Q}_{12,opt} \approx \dot{Q}_{12,opt}^{<0} &\approx -\frac{\Delta_1^2}{e^2 R_2} \sqrt{\frac{\Delta_2}{\Delta_1}} e^{-\Delta_1/k_B T_1} \ln(\sqrt{\gamma_1} + \sqrt{\gamma_2}) \\
&= \frac{\Delta_1}{e} I_{12,opt}.
\end{aligned}$$



# QPSJ Hamiltonian for an Underdamped Josephson Junction

## Introduction

In this appendix, we will show how to obtain the Hamiltonian Eq. (4.7) of the current-biased quantum phase-slip junction (QPSJ) of Fig. 4.1(b) from that one of the Josephson junction of Fig. D.1(a) and we will prove that the two circuits of Fig. 4.1 are equivalent.

## D.1 Current-biased representation

### D.1.1 The QPSJ Hamiltonian

We start by considering the circuit depicted in Fig. D.1(a). Neglecting the contribution of the quasi-particle excitations, the Hamiltonian of a Josephson junction (JJ) biased by a time-dependent current  $I(t) = I_0 + I_{mw} \cos(\omega_{mw}t)$ , in parallel with a capacitance  $C$  and an  $R$ - $L$  environment is given by the sum of the charging energy, the non-linear Josephson energy and the energy of the environment [see Eq. (4.8)],

$$\hat{H}_s = \frac{1}{2C} \left[ \int_{-\infty}^t dt' I(t') + \hat{Q}_{RL} + \hat{Q} \right]^2 - E_J \cos(\hat{\phi}) + \hat{H}_{env} . \quad (\text{D.1})$$

The phase operator  $\hat{\phi}$  is the phase difference between the two superconductors forming the junction and  $\hat{Q}$  is its conjugate charge operator  $[\hat{\phi}, \hat{Q}] = 2ei$ , i.e., the charge tunneling through the junction. In Eq. (D.1), we also introduced  $\hat{Q}_{RL} = \sum_{\lambda} \hat{Q}_{\lambda}$  which accounts for the charge noise produced by the  $R$ - $L$  environment, as discussed in Sec. 4.2.

The equivalence between Hamiltonian (D.1) and the QPSJ Hamiltonian (4.7) can be demonstrated through the following steps. First, we apply the gauge and

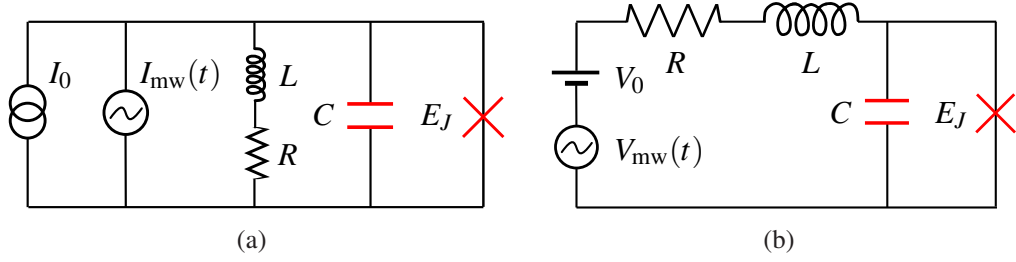


Figure D.1: Current-biased (a) and voltage-biased (b) Josephson junction with Josephson energy  $E_J$  in parallel with a capacitance  $C$  and embedded in a resistive ( $R$ ) and inductive ( $L$ ) electromagnetic environment. In both circuit, the total bias is the sum of a DC component,  $I_0$  (a) and  $V_0$  (b), and an AC one,  $I_{\text{mw}}(t)$  (a) and  $V_{\text{mw}}(t)$  (b).

the unitary transformations

$$\hat{U}_g(t) = \exp \left[ -i\hat{\phi} \int_{-\infty}^t dt' I(t')/2e \right] \quad \text{and} \quad \hat{U}_{\text{env}} = \exp \left[ -i\hat{\phi} \hat{Q}_{\text{RL}}/2e \right]$$

respectively to Eq. (D.1) and we get

$$\hat{H}'_s = \frac{\hat{Q}^2}{2C} - E_J \cos(\hat{\phi}) - \frac{\hbar I(t)}{2e} \hat{\phi} + \hat{H}_{\text{env}} [\{\hat{Q}_\lambda\}, \{\hat{\phi}_\lambda + \hat{\phi}\}]. \quad (\text{D.2})$$

Here the first and second term correspond to the standard Hamiltonian  $\hat{H}_J$  of an isolated JJ, where  $\hat{Q}$  gives now the charge localized across the capacitance of junction  $C$ . In the tight-binding regime,  $E_J \gg E_C$ ,  $\hat{H}'_s$  becomes

$$\hat{H}''_s = -U_0 \cos \left( \frac{\pi}{e} \hat{q} \right) - \frac{\hbar I(t)}{2e} \hat{\phi} + \hat{H}_{\text{env}} [\{\hat{Q}_\lambda\}, \{\hat{\phi}_\lambda + \hat{\phi}\}]. \quad (\text{D.3})$$

where  $\hat{q}$  is the quasi-charge operator of the QPSJ and

$$U_0 = 8\sqrt{E_J \hbar \omega_p / \pi} \exp(-\sqrt{8E_J/E_C}) = 2eV_c/2\pi \quad (\text{D.4})$$

the half-bandwidth of the first Bloch band of  $\hat{H}_J$ . Within this limit, an energy gap of the order of the plasma frequency  $\hbar \omega_p = \sqrt{8E_J E_C}$  separates the first from the second Bloch band. We neglect the possibility of inter-band Landau-Zener transitions assuming the low temperature and bias current limit ( $k_B T, \hbar I_0/2e, \hbar I_{\text{mw}}/2e$ )  $\ll \hbar \omega_p$  as well as considering an off-resonance microwave field,  $\omega_{\text{mw}} \ll \omega_p$ .

Finally, we apply the inverse unitary transformation  $\hat{U}_{\text{env}}^{-1}$  to Eq. (D.3) and we obtain the effective low-energy Hamiltonian

$$\hat{H} = -U_0 \cos \left[ \frac{\pi}{e} (\hat{q} + \hat{Q}_{\text{RL}}) \right] - \frac{\hbar I(t)}{2e} \hat{\phi} + \hat{H}_{\text{env}} [\{\hat{Q}_\lambda\}, \{\hat{\phi}_\lambda\}]. \quad (\text{D.5})$$

This is the energy operator (4.7) introduced in Sec. 4.2, describing a current-biased quantum phase-slip junction coupled to an external  $R$ - $L$  electromagnetic environment, as depicted in Fig. 4.1(b).

### D.1.2 The quasi-charge equation of motion

According to the Heisenberg picture, the Hamiltonian operator (D.5) generates the following first order differential equations for the time-dependent observables  $\hat{q}$ ,  $\hat{\phi}$ ,  $\hat{Q}_\lambda$ , and  $\hat{\phi}_\lambda$ :

$$\frac{d\hat{q}}{dt} = I(t), \quad (\text{D.6})$$

$$\frac{\hbar}{2e} \frac{d\hat{\phi}}{dt} = V_c \sin \left[ \frac{\pi}{e} (\hat{q} + \hat{Q}_{\text{RL}}) \right], \quad (\text{D.7})$$

$$\frac{d\hat{Q}_\lambda}{dt} = -\frac{1}{L_\lambda} \left( \frac{\hbar \hat{\phi}_\lambda}{2e} \right), \quad (\text{D.8})$$

$$\frac{\hbar}{2e} \frac{d\hat{\phi}_\lambda}{dt} = V_c \sin \left[ \frac{\pi}{e} (\hat{q} + \hat{Q}_{\text{RL}}) \right] + \frac{\hat{Q}_\lambda}{C_\lambda}. \quad (\text{D.9})$$

Here we used the commutation relation  $[\hat{\phi}, \hat{q}] = 2ei$ . In general, the dynamics of the quasi-charge operator  $\hat{\mathbf{q}}$  appearing in the non-linear potential  $-U_0 \cos(\pi \hat{\mathbf{q}}/e)$  contained in its Hamiltonian determines the  $I_J$ - $V_J$  characteristic of a QPSJ. If we describe the circuit of Fig. 4.1(b) by means of Eq. (D.5), then  $\hat{\mathbf{q}} = \hat{q} + \hat{Q}_{\text{RL}}$ . As a result, the potential  $V_J$  across the QPS junction in Fig. 4.1(b) is  $V_c \sin[\pi(\hat{q} + \hat{Q}_{\text{RL}})/e]$  and is related to the phase difference  $\hat{\phi}$  between the two superconductors of the JJ [see Eq. (D.7)]. On the other hand, the time derivative of  $\hat{\mathbf{q}}$ ,

$$\frac{d\hat{\mathbf{q}}}{dt} = \frac{d\hat{q}}{dt} + \frac{d\hat{Q}_{\text{RL}}}{dt} = I(t) + \sum_\lambda \frac{d\hat{Q}_\lambda}{dt}, \quad (\text{D.10})$$

represents the current  $I_J$  flowing through the QPS junction rather than  $d\hat{q}/dt$ , which gives the total bias current [see Eq. (D.6)].

In order to derive the equation of motion of  $\hat{\mathbf{q}}$ , we start by considering the relation

$$L \frac{d^2 \hat{\mathbf{q}}(t)}{dt^2} = L \frac{dI(t)}{dt} + L \sum_\lambda \frac{d^2 \hat{Q}_\lambda}{dt^2}, \quad (\text{D.11})$$

obtained from Eq. (D.10) by multiplying by  $L$  and deriving with respect to time. Here the momentum  $\hat{Q}_\lambda(t)$  of the oscillator  $\lambda$  satisfies the differential equation

$$\frac{d^2 \hat{Q}_\lambda}{dt^2} = -\omega_\lambda^2 \hat{Q}_\lambda - \frac{1}{L_\lambda} V_J [\hat{\mathbf{q}}(t)], \quad (\text{D.12})$$

according to Eqs. (D.8) and (D.9), with  $V_J[\hat{\mathbf{q}}(t)] = V_c \sin[\pi\hat{\mathbf{q}}(t)/e]$ . The solution of Eq. (D.12) can be written as

$$\hat{Q}_\lambda(t) = \hat{Q}_\lambda^{(0)} - \int_{-\infty}^t dt' \frac{\sin[\omega_\lambda(t-t')]}{\omega_\lambda L_\lambda} V_J[\hat{\mathbf{q}}(t')]$$

and the corresponding first and second derivatives respect to the time  $t$  are

$$\frac{d\hat{Q}_\lambda}{dt} = \frac{d\hat{Q}_\lambda^{(0)}}{dt} - \int_{-\infty}^t dt' \frac{\cos[\omega_\lambda(t-t')]}{L_\lambda} V_J[\hat{\mathbf{q}}(t')] , \quad (\text{D.13})$$

$$\begin{aligned} \frac{d^2\hat{Q}_\lambda}{dt^2} &= \frac{d^2\hat{Q}_\lambda^{(0)}}{dt^2} - \frac{1}{L_\lambda} V_J[\hat{\mathbf{q}}(t')] \\ &- \int_{-\infty}^t dt' (-\omega_\lambda) \frac{\sin[\omega_\lambda(t-t')]}{L_\lambda} V_J[\hat{\mathbf{q}}(t')] , \end{aligned} \quad (\text{D.14})$$

where  $\hat{Q}_\lambda^{(0)}(t)$  is the homogeneous solution. Introducing the admittance

$$Y(t-t') \equiv \theta(t-t') \sum_\lambda \frac{\cos[\omega_\lambda(t-t')]}{L_\lambda} , \quad (\text{D.15})$$

and assuming that its Fourier transform is  $Y(\omega) = 1/(R - i\omega L)$ , one finds that

$$\sum_\lambda \frac{\cos[\omega_\lambda(t-t')]}{L_\lambda} = \frac{1}{L} e^{-\frac{R}{L}(t-t')}$$

whose time derivative gives

$$-\sum_\lambda \omega_\lambda \frac{\sin[\omega_\lambda(t-t')]}{L_\lambda} = -\frac{R}{L} \frac{1}{L} e^{-\frac{R}{L}(t-t')} = -\frac{R}{L} \sum_\lambda \frac{\cos[\omega_\lambda(t-t')]}{L_\lambda} . \quad (\text{D.16})$$

Inserting Eq. (D.13) in Eq. (D.10), one finds that

$$\sum_\lambda \int_{-\infty}^t dt' \frac{\cos[\omega_\lambda(t-t')]}{L_\lambda} V_J[\hat{\mathbf{q}}(t')] = I(t) + \delta I(t) - \frac{d\hat{\mathbf{q}}}{dt} , \quad (\text{D.17})$$

where we introduced the current noise

$$\delta I(t) \equiv \sum_\lambda \frac{d\hat{Q}_\lambda^{(0)}}{dt} = \frac{d\hat{Q}_{\text{RL}}}{dt}$$

produced by the  $R$ - $L$  environment. Combining Eqs. (D.16) and (D.17) with Eqs. (D.14) and (D.11), we finally obtain the equation of motion for the quasi-charge operator  $\hat{\mathbf{q}}(t)$ ,

$$L \frac{d^2\hat{\mathbf{q}}(t)}{dt^2} + R \frac{d\hat{\mathbf{q}}(t)}{dt} + V_J[\hat{\mathbf{q}}(t)] = V_I(t) + \delta V_I(t) , \quad (\text{D.18})$$

written in terms of the potential and the voltage noise

$$V_I(t) \equiv \left[ L \frac{dI(t)}{dt} + RI(t) \right] \quad \text{and} \quad \delta V_I(t) \equiv \left[ L \frac{d\delta I(t)}{dt} + R\delta I(t) \right].$$

From Eq. (D.18) we see that the time evolution of  $\hat{\mathbf{q}}$  in the circuit of Fig. 4.1(b) is equivalent to the damped dynamics of a quantum phase-particle with mass  $L$  and position  $\hat{\mathbf{q}}$  moving in the periodic potential  $-U_0 \cos(\pi\hat{\mathbf{q}}/e)$  under the effect of the time-dependent and aleatory external force  $V_I(t) + \delta V_I(t)$ .

## D.2 Voltage-biased representation

### D.2.1 The QPSJ Hamiltonian

We now focus on the circuit depicted in Fig. D.1(b) where a Josephson junction is connected in series to a resistance  $R$  and an inductance  $L$  and is biased with the voltage  $V(t) = V_0 + V_{\text{mw}}(t)$  which is the superposition of a DC component  $V_0$  and a time-dependent term,  $V_{\text{mw}}(t) = V_{\text{mw}} \sin(\omega_{\text{mw}}t)$ , oscillating with frequency  $\omega_{\text{mw}}$ . Considering only  $R$  as external electromagnetic environment,<sup>1</sup> the Hamiltonian of such a system can be written as [93]

$$\hat{H}_s^V = \hat{H}_J + \hat{H}_L + \hat{H}_{\text{env}}^V. \quad (\text{D.19})$$

In other words,  $\hat{H}_s^V$  is the sum of the ordinary JJ energy,  $\hat{H}_J = \hat{Q}^2/2C - E_J \cos(\hat{\phi})$ , the inductive energy

$$\hat{H}_L = \frac{1}{2L} \left( \frac{\hbar}{2e} \right)^2 \left[ \frac{2e}{\hbar} \int_{-\infty}^t dt' V(t') + \hat{\phi}_R - \hat{\phi} \right]^2 \quad (\text{D.20})$$

depending on the phase difference noise  $\hat{\phi}_R = \sum_{\mu} \hat{\phi}_{\mu}$  generated by  $R$ , and the Caldeira-Legget Hamiltonian

$$\hat{H}_{\text{env}}^V = \sum_{\mu=1}^{+\infty} \left[ \frac{\hat{Q}_{\mu}^2}{2C_{\mu}} + \frac{1}{2L_{\mu}} \left( \frac{\hbar\hat{\phi}_{\mu}}{2e} \right)^2 \right], \quad (\text{D.21})$$

describing  $R$  as an ensemble of harmonic oscillators. The charge  $\hat{Q}_{\mu}$  and phase  $\hbar\hat{\phi}_{\mu}/2e$  operators are the momentum and position respectively of the oscillator  $\mu$  with mass  $C_{\mu}$  and characteristic frequency  $\omega_{\mu}^2 = 1/L_{\mu}C_{\mu}$ .

---

<sup>1</sup>note that in the current-biased case we assumed that the external environment was formed by both  $R$  and  $L$ .

For  $E_J \gg E_C = e^2/2C$ , the JJ is in the tight-binding limit and its Hamiltonian  $\hat{H}_J$  becomes

$$\hat{H}_J \simeq \hat{H}_J^{\text{TB}} = -U_0 \cos\left(\frac{\pi}{e}\hat{q}\right) \quad (\text{D.22})$$

where  $\hat{q}$  is the quasi-charge operator and  $U_0$  the half-bandwidth of the first Bloch band of  $\hat{H}_J$  [see Eq. (D.4)]. Within this approximation, the Hamiltonian (D.19) gives the energy of a voltage-biased QPSJ coupled to a resistive dissipative bath [see Fig. D.1(b)]. This statement becomes evident if two unitary transformations are applied to the tight-binding version of Eq. (D.19). The first one is the gauge transformation  $\hat{U}_g^V = \exp[-i\hat{q} \int^t dt' V(t')/\hbar]$ . It acts only on the Hamiltonian (D.20) eliminating the term  $\int^t dt' V(t')$  from it. Since  $\hat{U}_g^V$  depends on time, the term  $-V(t)\hat{q}$  appears in the new Hamiltonian as well. The second one is a unitary transformation involving the operators of the environment, i.e.,  $\hat{U}_{\text{env}}^V = \exp[-i\hat{q}\hat{\phi}_R/2e]$ . On one side it cancels the phase  $\hat{\phi}_R$  from the Eq. (D.20). On the other side, it shifts the charge  $\hat{Q}_\mu$  in Eq. (D.21) by  $-\hat{q}$ . As a result, one finally gets

$$\hat{H}^V = \frac{1}{2L} \left(\frac{\hbar\hat{\phi}}{2e}\right)^2 - U_0 \cos\left(\frac{\pi}{e}\hat{q}\right) - V(t)\hat{q} + \hat{H}_{\text{env}}^V[\{\hat{Q}_\mu - \hat{q}\}, \{\hat{\phi}_\mu\}] \quad (\text{D.23})$$

where the first three terms give the Hamiltonian of a voltage-biased ideal QPSJ and

$$\hat{H}_{\text{env}}^V[\{\hat{Q}_\mu - \hat{q}\}, \{\hat{\phi}_\mu\}] = \sum_{\mu=1}^{+\infty} \left[ \frac{(\hat{Q}_\mu - \hat{q})^2}{2C_\mu} + \frac{1}{2L_\mu} \left(\frac{\hbar\hat{\phi}_\mu}{2e}\right)^2 \right].$$

The Hamiltonian (D.23) describes the non-coherent tunneling of the phase through a tilted cosine potential.

## D.2.2 The quasi-charge equation of motion

Considering the Hamiltonian (D.23), we see that, in this case, only the quasi-charge operator  $\hat{q}$  determines the  $I_J$ - $V_J$  characteristic of the QPSJ in the voltage-biased circuit of Fig. 4.1(a). In order to derive the equation of motion for this observable, let us first write the corresponding Heisenberg equations for the oper-

ators  $\hat{q}$ ,  $\hat{\phi}$ ,  $\hat{Q}_\mu$ , and  $\hat{\phi}_\mu$ :

$$\frac{d\hat{q}}{dt} = -\frac{\hbar}{2e} \frac{\hat{\phi}}{L}, \quad (\text{D.24})$$

$$\frac{\hbar}{2e} \frac{d\hat{\phi}}{dt} = V_c \sin \left[ \frac{\pi}{e} \hat{q}(t) \right] - V(t) - \sum_{\mu} \left( \frac{\hat{Q}_\mu - \hat{q}}{C_\mu} \right), \quad (\text{D.25})$$

$$\frac{d\hat{Q}_\mu}{dt} = -\frac{\hbar}{2e} \frac{\hat{\phi}_\mu}{L_\mu}, \quad (\text{D.26})$$

$$\frac{\hbar}{2e} \frac{d\hat{\phi}_\mu}{dt} = \frac{\hat{Q}_\mu - \hat{q}}{C_\mu}. \quad (\text{D.27})$$

In this case,  $V_c \sin[\pi\hat{q}(t)/e]$  and  $d\hat{q}/dt$  are the potential  $V_J[\hat{q}(t)]$  and the current  $I_J$  of the QPS junction. Combining the time-derivative of Eq. (D.24) with Eqs. (D.25) and (D.27) and multiplying both sides by  $L$ , one gets

$$L \frac{d^2\hat{q}}{dt^2} = V(t) - V_J[\hat{q}(t)] + \sum_{\mu} \left( \frac{\hbar}{2e} \frac{d\hat{\phi}_\mu}{dt} \right). \quad (\text{D.28})$$

On the other hand, inserting Eq. (D.26) into the time derivative of Eq. (D.27), we obtain the second order differential equation

$$\frac{\hbar}{2e} \frac{d^2\hat{\phi}_\mu}{dt^2} = -\omega_\mu^2 \frac{\hbar\hat{\phi}_\mu}{2e} - \frac{1}{C_\mu} \frac{d\hat{q}}{dt}. \quad (\text{D.29})$$

The solution of Eq. (D.29) and its first time-derivative read

$$\begin{aligned} \frac{\hbar\hat{\phi}_\mu}{2e} &= \frac{\hbar\hat{\phi}_\mu^{(0)}}{2e} - \int_{-\infty}^t dt' \frac{\sin[\omega_\mu(t-t')]}{\omega_\mu C_\mu} \frac{d\hat{q}}{dt'}, \\ \frac{\hbar}{2e} \frac{d\hat{\phi}_\mu}{dt} &= \frac{\hbar}{2e} \frac{d\hat{\phi}_\mu^{(0)}}{dt} - \int_{-\infty}^t dt' \frac{\cos[\omega_\mu(t-t')]}{C_\mu} \frac{d\hat{q}}{dt'}, \end{aligned} \quad (\text{D.30})$$

where  $\hbar\hat{\phi}_\mu^{(0)}(t)/2e$  is the homogeneous solution of Eq. (D.29). Inserting Eq. (D.30) into Eq. (D.28), imposing that

$$\theta(t-t') \sum_{\mu} \frac{\cos[\omega_\mu(t-t')]}{C_\mu} = Z(t-t') = R \delta(t-t'),$$

i.e., the Fourier transform of the impedance  $Z(t-t')$  of the environment is equal to the resistance  $R$ , and defining the voltage noise as

$$\delta V(t) \equiv \sum_{\mu} \frac{\hbar}{2e} \frac{d\hat{\phi}_\mu^{(0)}}{dt} = \frac{\hbar}{2e} \frac{d\hat{\phi}_R}{dt},$$

we finally obtain the quasi-charge equation of motion

$$L \frac{d^2 \hat{q}}{dt^2} + R \frac{d\hat{q}}{dt} + V_J [\hat{q}(t)] = V(t) + \delta V(t) , \quad (\text{D.31})$$

which is similar to Eq. (D.18). Indeed, thanks to the Thévenin-Norton equivalence relations,  $V(t)$  and  $\delta V(t)$  are equal to the voltages  $V_I(t)$  and  $\delta V_I(t)$  of the current-biased representation discussed in the previous section. As a result, the dynamics of the quasi-charges  $\hat{\mathbf{q}}$  and  $\hat{q}$  is determined by the same equation in both representations. In other words, the circuit of Fig. 4.1(a) is equivalent to the circuit of Fig. 4.1(b).

# Voltage Across a Microwave Irradiated Quantum Phase-Slip Junction

## Introduction

In this appendix, we give a more detailed derivation of the main results presented in Secs. 4.3 and 4.4 of Chap. 4 about the voltage across a current-biased QPSJ, irradiated with microwaves and connected to a resistive ( $R$ ) and inductive ( $L$ ) electromagnetic environment [see Fig. 4.1(b)].

## E.1 Perturbative expansion at all orders in $U_0$ : Keldysh formalism

The  $I_J$ - $V_J$  characteristic of the current-biased QPSJ in the circuit of Fig. 4.1(b) is determined by the equations

$$\begin{aligned}
 I_J &= I_0 - \frac{V_J}{R}, \\
 V_J &= \langle \hat{V}_J(t) \rangle_{\text{DC}} = \left\langle V_c \sin \left[ \frac{\pi}{e} \left( \hat{q}(t) + \sum_{\lambda} \hat{Q}_{\lambda}(t) \right) \right] \right\rangle_{\text{DC}}, \quad (\text{E.1})
 \end{aligned}$$

i.e., by the time-average (DC component) of the quantum mean value  $\langle \dots \rangle$  of the voltage operator  $\hat{V}_J(t)$  over the states of the Hamiltonian of the system,

$$\hat{H} = -U_0 \cos \left[ \frac{\pi}{e} \left( \hat{q} + \sum_{\lambda} \hat{Q}_{\lambda} \right) \right] - \frac{\hbar I(t)}{2e} \hat{\phi} + \sum_{\lambda} \left[ \frac{\hat{Q}_{\lambda}^2}{2C_{\lambda}} + \frac{1}{2L_{\lambda}} \left( \frac{\hbar \hat{\phi}_{\lambda}}{2e} \right)^2 \right]. \quad (\text{E.2})$$

We calculated  $V_J$  using the Keldysh formalism [110–112] which is based on the time evolution of  $\hat{V}_J(t)$  in the interaction picture along the so-called Keldysh closed contour  $C_K$ , going forward and then backward in time, from  $t = -\infty$  to

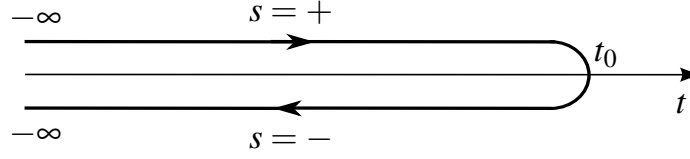


Figure E.1: Keldysh closed time-contour  $C_K$ . The forward/backward branch is indicated with the Keldysh index  $s = +/ -$ .

a certain time  $t_0$  and then back to  $t = -\infty$  [see Fig. E.1]. Writing the Hamiltonian as  $\hat{H} = \hat{H}_0 + \hat{W}$  where  $\hat{W}$  plays the role of the perturbation, the quantum statistical average of the generic operator  $\hat{O}_i(t_0)$  in interaction picture can be written as

$$\langle \hat{O}_i(t_0) \rangle_{\hat{H}} = \left\langle T_{C_K} \left[ \exp \left( -\frac{i}{\hbar} \oint_{C_K} dt' \hat{W}_i(t') \right) \hat{O}_i(t_0) \right] \right\rangle_{\hat{H}_0}. \quad (\text{E.3})$$

Here  $T_{C_K}$  is the time-ordering operator on the Keldysh contour  $C_K$ ,  $\hat{O}_i(t) = U_0^\dagger(t) \hat{O} U_0(t)$  and  $\hat{W}_i(t) = U_0^\dagger(t) \hat{W} U_0(t)$  with

$$U_0(t) = T \left[ \exp \left( -\frac{i}{\hbar} \int_{t_{in}}^t dt' \hat{H}_0(t') \right) \right], \quad (\text{E.4})$$

time evolution operator generated by the unperturbed Hamiltonian  $\hat{H}_0$ . The use of the contour  $C_K$  corresponds to switching adiabatically on and off the perturbation  $\hat{W}$  in such a way that the initial and final states are the same.

Assuming that the unperturbed Hamiltonian and the perturbation are

$$\hat{H}_0 = -\frac{\hbar I(t)}{2e} \hat{\phi} + \sum_{\lambda} \left[ \frac{\hat{Q}_{\lambda}^2}{2C_{\lambda}} + \frac{1}{2L_{\lambda}} \left( \frac{\hbar \hat{\phi}_{\lambda}}{2e} \right)^2 \right], \quad (\text{E.5})$$

$$\hat{W} = -U_0 \cos \left[ \frac{\pi}{e} \left( \hat{q} + \sum_{\lambda} \hat{Q}_{\lambda} \right) \right], \quad (\text{E.6})$$

respectively, and rewriting the potential operator  $\hat{V}_J(t)$  in Eq. (E.1) using the relation  $\sin(x) = \sum_{\eta_0=\pm} [(\eta_0/2i) \exp(ix\eta_0)]$ ,

$$\hat{V}_J(t) = V_c \sum_{\eta_0=\pm} \frac{\eta_0}{2i} \exp \left[ i \frac{\pi}{e} \left( \hat{q}(t) + \sum_{\lambda} \hat{Q}_{\lambda}(t) \right) \eta_0 \right],$$

the quantum mean value of the voltage across the QPSJ evaluated at the time  $t = t_0$

reads

$$\begin{aligned} \frac{V_J(t_0)}{V_c} &= \sum_{\eta_0=\pm} \frac{\eta_0}{2i} \left\langle T_{C_K} \exp \left\{ -\frac{i}{\hbar} \oint_{C_K} dt' (-U_0) \cos \left[ \frac{\pi}{e} \left( \hat{q}(t') + \sum_{\lambda} \hat{Q}_{\lambda}(t) \right) \right] \right\} \right. \\ &\quad \left. \times \exp \left[ i \frac{\pi}{e} \left( \hat{q}(t_0) + \sum_{\lambda} \hat{Q}_{\lambda}(t_0) \right) \eta_0 \right] \right\rangle_{\hat{H}_0}, \end{aligned}$$

according to Eq. (E.3). Using the definition of the time-ordered evolution operator on the Keldysh contour and expressing the cosine function in terms of the dichotomic variable  $\eta = \pm$ ,  $\cos(x) = \sum_{\eta=\pm} (1/2) \exp(ix\eta)$ , this last expression becomes

$$\begin{aligned} \frac{V_J(t_0)}{V_c} &= \sum_{n=0}^{+\infty} \frac{1}{n!} \left( \frac{iU_0}{2\hbar} \right)^n \sum_{\eta_0=\pm} \sum_{\eta_1=\pm} \sum_{\eta_2=\pm} \cdots \sum_{\eta_n=\pm} \oint_{C_K} dt_1 \oint_{C_K} dt_2 \cdots \oint_{C_K} dt_n \\ &\quad \times \frac{\eta_0}{2i} \left\langle T_{C_K} \exp \left\{ i \frac{\pi}{e} \sum_{k=0}^n \eta_k \left[ \hat{q}(t_k) + \sum_{\lambda} \hat{Q}_{\lambda}(t_k) \right] \right\} \right\rangle_{\hat{H}_0}. \quad (\text{E.7}) \end{aligned}$$

At this point, let us introduce the Keldysh index  $s_k = +/−$  which refers to the forward/backward branch of the closed contour  $C_K$ . Then, the  $k$ -th integral in Eq. (E.7) can be written as

$$\begin{aligned} \oint_{C_K} dt_k &= \oint_{-\infty}^{t_{k-1}} dt_k = \int_{-\infty}^{t_{k-1}} dt_k^+ + \int_{t_{k-1}}^{-\infty} dt_k^- \\ &= \int_{-\infty}^{t_{k-1}} dt_k^+ - \int_{-\infty}^{t_{k-1}} dt_k^- = \sum_{s_k=\pm} s_k \int_{-\infty}^{t_{k-1}} dt_k, \end{aligned}$$

where  $t_k^{+/-} = t_k^{s_k}$  is the time variable referring to the forward/backward branch. As a result, the time-ordering operator  $T_{C_K}$  is replaced by  $s_k$  and Eq. (E.7) can be recast in the form

$$\begin{aligned} \frac{V_J(t_0)}{V_c} &= \sum_{n=0}^{+\infty} \left( \frac{iU_0}{2\hbar} \right)^n \sum_{\{\eta_k\}} \frac{\eta_0}{2i} \int_{-\infty}^{t_0} dt_1 \int_{-\infty}^{t_1} dt_2 \cdots \int_{-\infty}^{t_{n-1}} dt_n \\ &\quad \times \sum_{\{s_k\}} s_1 \cdots s_n \left\langle \exp \left\{ i \frac{\pi}{e} \sum_{k=0}^n \eta_k \left[ \hat{q}(t_k^{s_k}) + \sum_{\lambda} \hat{Q}_{\lambda}(t_k^{s_k}) \right] \right\} \right\rangle_{\hat{H}_0}, \quad (\text{E.8}) \end{aligned}$$

for a given time ordering, for instance  $|t_n| < |t_{n-1}| < \cdots < |t_1| < |t_0|$ . In Eq. (E.8), we introduced the sums over all the possible configurations of  $\eta_k$  and  $s_k$ ,

$$\begin{aligned} \sum_{\{\eta_k\}} &= \sum_{\eta_0=\pm} \sum_{\eta_1=\pm} \sum_{\eta_2=\pm} \cdots \sum_{\eta_n=\pm} \\ \sum_{\{s_k\}} &= \sum_{s_1=\pm} \sum_{s_2=\pm} \cdots \sum_{s_n=\pm}. \end{aligned}$$

Since the operators  $\hat{q}$  and  $\hat{Q}_\lambda$  commute, the mean value in Eq. (E.8) is equal to the product of two terms. The first one,

$$F_q \equiv \left\langle \exp \left\{ i \frac{\pi}{e} \sum_{k=0}^n \eta_k \hat{q}(t_k^{s_k}) \right\} \right\rangle_{\hat{H}_0}, \quad (\text{E.9})$$

describes an ideal QPS junction. Whereas the second one,

$$F_{\text{env}} \equiv \left\langle \exp \left\{ i \frac{\pi}{e} \sum_{k=0}^n \eta_k \left[ \sum_{\lambda} \hat{Q}_\lambda(t_k^{s_k}) \right] \right\} \right\rangle_{\hat{H}_0}, \quad (\text{E.10})$$

accounts for the effect of the external electromagnetic environment. In the following, we calculate these two mean values for a fixed value of  $n$ .

### E.1.1 The mean value $F_q$

The time evolution operator for  $\hat{q}$  in the interaction picture is

$$U_0^{(1)}(t) = \exp \left\{ -\frac{i}{\hbar} \hat{\phi} \int_{t_{in}}^t dt' \left( -\frac{\hbar I(t')}{2e} \right) \right\},$$

see Eqs. (E.5) and (E.4), where we omitted the part depending on the operators of the environment  $\hat{Q}_\lambda$  and  $\phi_\lambda$  because they commute with  $\hat{q}$ . The time operator  $U_0^{(1)}(t)$  is the translation operator for  $\hat{q}$ . Since  $[\hat{\phi}, \hat{q}] = 2ei$ , we have

$$\begin{aligned} \hat{q}(t) &= U_0^{\dagger(1)}(t) \hat{q} U_0^{(1)}(t) = \hat{q} + \int_{t_{in}}^t dt' I(t') \\ &= \hat{q} + \int_{t_i}^t dt' [I_0 + I_{\text{mw}} \cos(\omega_{\text{mw}} t')] \\ &= \hat{q} + I_0 t + \frac{I_{\text{mw}}}{\omega_{\text{mw}}} \sin(\omega_{\text{mw}} t) + q_{in}. \end{aligned}$$

Here we introduced the constant quasi-charge  $q_{in}$  determined by means of the initial conditions. Using this last result, Eq. (E.9) becomes

$$F_q = \left\langle \exp \left\{ i \frac{\pi}{e} \hat{q} \sum_{k=0}^n \eta_k \right\} \right\rangle_{\hat{H}_0} \exp \left\{ i \frac{\pi}{e} \sum_{k=0}^n \eta_k \left[ I_0 t_k^{s_k} + \frac{I_{\text{mw}}}{\omega_{\text{mw}}} \sin(\omega_{\text{mw}} t_k^{s_k}) + q_{in} \right] \right\}.$$

Assuming that  $q_0$  the mean value of the quasi-charge in the ground state of  $\hat{H}_0$ , we finally get

$$F_q = \exp \left\{ i \frac{\pi}{e} (q_0 + q_{in}) \sum_{k=0}^n \eta_k \right\} \exp \left\{ i \frac{\pi}{e} \sum_{k=0}^n \eta_k \left[ I_0 t_k^{s_k} + \frac{I_{\text{mw}}}{\omega_{\text{mw}}} \sin(\omega_{\text{mw}} t_k^{s_k}) \right] \right\}. \quad (\text{E.11})$$

### E.1.2 The mean value $F_{\text{env}}$

Assuming that the external bath is an ensemble of independent harmonic oscillators, and introducing the creation,  $b_\lambda^\dagger$ , and the annihilation,  $b_\lambda$ , operators for a fixed value of the quantum number  $\lambda$ , the conjugated variables  $\hat{\phi}_\lambda$  and  $\hat{Q}_\lambda$  can be written as

$$\hat{\phi}_\lambda = \gamma_\lambda (b_\lambda^\dagger + b_\lambda) \quad , \quad \hat{Q}_\lambda = \frac{ie}{\gamma_\lambda} (b_\lambda^\dagger - b_\lambda) \quad ,$$

with  $\gamma_\lambda = \sqrt{2e^2/C_\lambda \hbar \omega_\lambda}$ ,  $\omega_\lambda^2 = 1/L_\lambda C_\lambda$ ,  $[b_\lambda, b_\lambda^\dagger] = 1$  and  $[\hat{\phi}_\lambda, \hat{Q}_\lambda] = 2ei$ . Consequently, the Hamiltonian of the environment is

$$\hat{H}_{\text{env}} = \sum_{\lambda=1}^{+\infty} \left[ \frac{\hat{Q}_\lambda^2}{2C_\lambda} + \frac{1}{2L_\lambda} \left( \frac{\hbar}{2e} \right)^2 \hat{\phi}_\lambda^2 \right] = \sum_{\lambda=1}^{+\infty} \hbar \omega_\lambda \left( b_\lambda^\dagger b_\lambda + \frac{1}{2} \right) .$$

The operator  $\hat{Q}_\lambda$  in the interaction picture evolves in time according to

$$U_0^{(2)}(t) = \exp \left\{ -\frac{i}{\hbar} t \sum_{\lambda=1}^{+\infty} \hbar \omega_\lambda \left( b_\lambda^\dagger b_\lambda + \frac{1}{2} \right) \right\}$$

meaning that

$$\hat{Q}_\lambda(t) = U_0^{\dagger(2)}(t) \hat{Q}_\lambda U_0^{(2)}(t) = \frac{ie}{\gamma_\lambda} \left( b_\lambda^\dagger e^{i\omega_\lambda t} - b_\lambda e^{-i\omega_\lambda t} \right) . \quad (\text{E.12})$$

Before using this relation, let us first rewrite Eq. (E.10) in the form

$$F_{\text{env}} = \prod_{\lambda=1}^{+\infty} \left\langle \exp \left\{ i \frac{\pi}{e} \sum_{k=0}^n \eta_k \hat{Q}_\lambda(t_k^{s_k}) \right\} \right\rangle_{\hat{H}_0} ,$$

since the environment is an ensemble of independent harmonic oscillators,  $[\hat{Q}_\lambda, \hat{Q}_{\lambda'}] = 0$ . In addition, Wick's theorem allows to recast  $F_{\text{env}}$  in the form

$$F_{\text{env}} = \prod_{\lambda=1}^{+\infty} \exp \left\{ -\frac{1}{2} \left( \frac{\pi}{e} \right)^2 \left\langle \sum_{k=0}^n \sum_{k'=0}^n \eta_k \eta_{k'} \hat{Q}_\lambda(t_k^{s_k}) \hat{Q}_\lambda(t_{k'}^{s_{k'}}) \right\rangle_{\hat{H}_0} \right\} . \quad (\text{E.13})$$

In order to evaluate  $F_{\text{env}}$  we need the mean value of the product of two charge operators  $\hat{Q}_\lambda(t)$  at different times, namely the correlation function

$$\left\langle \sum_{k=0}^n \sum_{k'=0}^n \eta_k \eta_{k'} \hat{Q}_\lambda(t_k) \hat{Q}_\lambda(t_{k'}) \right\rangle_{\hat{H}_0} = \sum_{k=0}^n \sum_{k'=0}^n \eta_k \eta_{k'} \left\langle \hat{Q}_\lambda(t_k) \hat{Q}_\lambda(t_{k'}) \right\rangle_{\hat{H}_0} . \quad (\text{E.14})$$

Such a thermal average satisfies the symmetry relation

$$\langle \hat{Q}_\lambda(t_k) \hat{Q}_\lambda(t_{k'}) \rangle = \langle \hat{Q}_\lambda(t_{k'}) \hat{Q}_\lambda(t_k) \rangle .$$

It follows that the substitution

$$\sum_{k=0}^n \sum_{k'=0}^n \dots \longrightarrow 2 \sum_{k=0}^n \sum_{k'=0}^k \dots = 2 \sum_{k=1}^n \sum_{k'=0}^{k-1} \dots$$

can be used to rewrite Eq. (E.13). Note that the index  $k'$  is always smaller than  $k$  meaning that  $|t_{k'}| > |t_k|$ , assuming valid the time ordering  $|t_n| < |t_{n-1}| < \dots < |t_1| < |t_0|$ . When  $t_k \neq t_{k'}$ , one gets

$$\langle \hat{Q}_\lambda(t_k) \hat{Q}_\lambda(t_{k'}) \rangle_{H_0} = \frac{e^2}{\gamma_\lambda^2} \left\{ \left[ 1 + n_B(\omega_\lambda) \right] e^{-i\omega_\lambda(t_k - t_{k'})} + n_B(\omega_\lambda) e^{i\omega_\lambda(t_k - t_{k'})} \right\} \quad (\text{E.15})$$

using Eq. (E.12), the mean values

$$\langle b_\lambda(t_k) b_\lambda(t_{k'}) \rangle_{\hat{H}_0} = 0 \quad \langle b_\lambda^\dagger(t_k) b_\lambda^\dagger(t_{k'}) \rangle_{\hat{H}_0} = 0$$

and imposing that the environment is at the thermal equilibrium, i.e.,

$$\langle b_\lambda^\dagger(t_k) b_\lambda(t_{k'}) \rangle_{\hat{H}_0} = n_B(\omega_\lambda) \quad \langle b_\lambda(t_k) b_\lambda^\dagger(t_{k'}) \rangle_{\hat{H}_0} = 1 + n_B(\omega_\lambda) ,$$

where  $n_B(\omega_\lambda) = [\exp(\hbar\omega_\lambda/k_B T) - 1]^{-1}$  is the Bose-Einstein distribution function. In particular, Eq. (E.15) gives

$$\langle \hat{Q}_\lambda(0) \hat{Q}_\lambda(0) \rangle_{H_0} = \langle \hat{Q}_\lambda^2(0) \rangle_{H_0} = \frac{e^2}{\gamma_\lambda^2} [1 + 2n_B(\omega_\lambda)] \quad (\text{E.16})$$

for  $t_k = t_{k'}$ . At this point, let us define the function

$$f_\lambda(t_k - t_{k'}) \equiv \langle \hat{Q}_\lambda(t_k) \hat{Q}_\lambda(t_{k'}) - \hat{Q}_\lambda^2(0) \rangle_{\hat{H}_0} .$$

Using Eqs. (E.15) and (E.16), it reads

$$\begin{aligned} f_\lambda &= \frac{e^2}{\gamma_\lambda^2} \left\{ \left[ 1 + n_B(\omega_\lambda) \right] \left[ e^{-i\omega_\lambda(t_k - t_{k'})} - 1 \right] + n_B(\omega_\lambda) \left[ e^{i\omega_\lambda(t_k - t_{k'})} - 1 \right] \right\} \\ &= \frac{e^2}{\gamma_\lambda^2} \left\{ \left[ 2n_B(\omega_\lambda) + 1 \right] \left[ \cos[\omega_\lambda(t_k - t_{k'})] - 1 \right] - i \sin[\omega_\lambda(t_k - t_{k'})] \right\} . \end{aligned} \quad (\text{E.17})$$

We see that it depends on the difference between  $t_k$  and  $t_{k'}$ . Depending on the position of  $t_k$  and  $t_{k'}$  on the Keldysh contour  $C_K$ , the difference  $t_k - t_{k'}$  can be positive or negative. Four cases are possible considering  $|t_{k'}| > |t_k|$ :

1.  $[t_k = t_k^+, t_{k'} = t_{k'}^+] \Rightarrow \langle \hat{Q}_\lambda(t_{k'}) \hat{Q}_\lambda(t_k) - \hat{Q}_\lambda^2(0) \rangle_{H_0} = f_\lambda [+ (t_{k'} - t_k)]$
2.  $[t_k = t_k^+, t_{k'} = t_{k'}^-] \Rightarrow \langle \hat{Q}_\lambda(t_{k'}) \hat{Q}_\lambda(t_k) - \hat{Q}_\lambda^2(0) \rangle_{H_0} = f_\lambda [+ (t_{k'} - t_k)]$
3.  $[t_k = t_k^-, t_{k'} = t_{k'}^+] \Rightarrow \langle \hat{Q}_\lambda(t_k) \hat{Q}_\lambda(t_{k'}) - \hat{Q}_\lambda^2(0) \rangle_{H_0} = f_\lambda [- (t_{k'} - t_k)]$
4.  $[t_k = t_k^-, t_{k'} = t_{k'}^-] \Rightarrow \langle \hat{Q}_\lambda(t_k) \hat{Q}_\lambda(t_{k'}) - \hat{Q}_\lambda^2(0) \rangle_{H_0} = f_\lambda [- (t_{k'} - t_k)]$

As a result,  $f_\lambda$  can be expressed in terms of the Keldysh index  $s_k$ , i.e.,  $f_\lambda = f_\lambda [s_k(t_{k'} - t_k)]$ .

Adding and subtracting the quantity  $\sum_{k,k'} \eta_k \eta_{k'} \langle \hat{Q}_\lambda^2(0) \rangle$ , Eq. (E.14) then becomes

$$\begin{aligned} \sum_{k=0}^n \sum_{k'=0}^n \eta_k \eta_{k'} \left\langle \hat{Q}_\lambda(t_k^{s_k}) \hat{Q}_\lambda(t_{k'}^{s_{k'}}) \right\rangle_{\hat{H}_0} &= \\ &= 2 \sum_{k=1}^n \sum_{k'=0}^{k-1} \eta_k \eta_{k'} f_\lambda [s_k(t_{k'} - t_k)] + \left( \sum_{k=0}^n \eta_k \right)^2 \langle \hat{Q}_\lambda^2(0) \rangle_{\hat{H}_0}. \end{aligned}$$

Inserting this last formula into Eq. (E.13) and reintroducing the sum over  $\lambda$  we get

$$\begin{aligned} F_{\text{env}} = \exp \left\{ -\frac{1}{2} \left( \frac{\pi}{e} \right)^2 \left[ 2 \sum_{k=1}^n \sum_{k'=0}^{k-1} \eta_k \eta_{k'} \sum_{\lambda=1}^{+\infty} f_\lambda [s_k(t_{k'} - t_k)] + \right. \right. \\ \left. \left. + \left( \sum_{k=0}^n \eta_k \right)^2 \sum_{\lambda=1}^{+\infty} \langle \hat{Q}_\lambda^2(0) \rangle_{H_0} \right] \right\}. \end{aligned} \quad (\text{E.18})$$

Let us first focus on the sum over  $\lambda$  of the function  $f_\lambda$  in this last expression. Equation (E.17) gives

$$\begin{aligned} \frac{1}{2} \left( \frac{\pi}{e} \right)^2 2 \sum_{\lambda=1}^{+\infty} f_\lambda [s_k(t_{k'} - t_k)] &= \sum_{\lambda=1}^{+\infty} \frac{1}{2} \left( \frac{\pi}{e} \right)^2 2 \frac{e^2}{2e^2} (C_\lambda \hbar \omega_\lambda) \\ &\times \left\{ \left[ 2n_B(\omega_\lambda) + 1 \right] \left[ \cos [s_k \omega_\lambda (t_{k'} - t_k)] - 1 \right] - i \sin [s_k \omega_\lambda (t_{k'} - t_k)] \right\} \end{aligned} \quad (\text{E.19})$$

taking also into account the constants which appear in the exponent of Eq. (E.18) and the definition of  $\gamma_\lambda$ . Since  $C_\lambda \hbar \omega_\lambda = \hbar / \omega_\lambda L_\lambda$  and  $\int_{-\infty}^{+\infty} d\omega \delta(|\omega| - \omega_\lambda) / 2 = 1$ , we rewrite Eq. (E.19) as

$$\frac{\hbar}{2} \left( \frac{\pi}{e} \right)^2 \sum_{\lambda=1}^{+\infty} \frac{1}{\omega_\lambda L_\lambda} \int_{-\infty}^{+\infty} \frac{d\omega}{2} \delta(|\omega| - \omega_\lambda) \otimes \left\{ \left[ 2n_B(\omega_\lambda) + 1 \right] \left[ \cos [s_k \omega_\lambda (t_{k'} - t_k)] - 1 \right] - i \sin [s_k \omega_\lambda (t_{k'} - t_k)] \right\}$$

and using the properties of the Dirac delta function we obtain

$$\frac{1}{2} \frac{\hbar}{2} \left( \frac{\pi}{e} \right)^2 \int_{-\infty}^{+\infty} \frac{d\omega}{\omega} \left\{ \left[ 2n_B(\omega) + 1 \right] \left[ \cos [s_k \omega (t_{k'} - t_k)] - 1 \right] - i \sin [s_k \omega (t_{k'} - t_k)] \right\} \sum_{\lambda=1}^{+\infty} \frac{1}{L_\lambda} \delta(|\omega| - \omega_\lambda).$$

Introducing the admittance of the environment

$$\Re[Y(\omega)] = \frac{\pi}{2} \sum_{\lambda=1}^{+\infty} \frac{\delta(|\omega| - \omega_\lambda)}{L_\lambda},$$

i.e., the real part of the Fourier transform of Eq. (D.15),<sup>1</sup> we finally obtain the charge-charge correlation function

$$J[s_k(t_{k'} - t_k)] = R_Q \int_{-\infty}^{+\infty} \frac{d\omega}{\omega} \Re[Y(\omega)] \otimes \left\{ \left[ 2n_B(\omega) + 1 \right] \left[ \cos [s_k \omega (t_{k'} - t_k)] - 1 \right] - i \sin [s_k \omega (t_{k'} - t_k)] \right\} \quad (\text{E.20})$$

with  $R_Q = h/4e^2$  the resistance quantum.

On the other hand, the other sum over  $\lambda$  in Eq. (E.18) involving the operator  $\hat{Q}_\lambda^2(0)$  is divergent. Indeed, if, for instance, the external environment can be described by means of an effective resistance  $R$  and an effective inductance  $L$  in parallel with the QPS junction, the admittance is

$$\Re[Y(\omega)] = \Re \left[ \frac{1}{R + i\omega L} \right] = \frac{1}{R} \left( \frac{1}{1 + \omega^2 \tau_L^2} \right) \quad \text{with} \quad \tau_L = \frac{L}{R}$$

<sup>1</sup>note that the same expression of  $\Re[Y(\omega)]$  can be also obtained imposing that the noise current  $\hat{I}_{\text{RL}} = d\hat{Q}_{\text{RL}}/dt$  satisfies the quantum fluctuation-dissipation theorem, see Eq. (4.9).

and consequently

$$\begin{aligned}
 F_{\text{div}} &\equiv \frac{1}{2} \left( \frac{\pi}{e} \right)^2 \sum_{\lambda=1}^{+\infty} \langle \hat{Q}_\lambda^2(0) \rangle_{H_0} = \frac{1}{2} \left( \frac{\pi}{e} \right)^2 \sum_{\lambda=1}^{+\infty} \frac{e^2}{\gamma_\lambda^2} \left[ 1 + 2n_B(\omega_\lambda) \right] \\
 &= \frac{R_Q}{2} \int_{-\infty}^{+\infty} \frac{d\omega}{\omega} \Re e [Y(\omega)] \coth \left( \frac{\hbar\omega}{2k_B T} \right) \\
 &= \frac{R_Q}{2R} \int_{-\infty}^{+\infty} \frac{d\omega}{\omega} \frac{1}{1 + \omega^2 \tau_L^2} \coth \left( \frac{\hbar\omega}{2k_B T} \right), \tag{E.21}
 \end{aligned}$$

which diverges. As a result, since  $F_{\text{div}}$  is time independent,  $F_{\text{env}}$  and consequently  $V_J(t_0)$  tend to zero. However, if we focus only on the configurations of  $\eta_k$  such that

$$\sum_{k=0}^n \eta_k = 0, \tag{E.22}$$

then  $F_{\text{env}} \neq 0$  as well as Eq. (E.8). The final expression of  $F_{\text{env}}$  is

$$F_{\text{env}} = \exp \left\{ - \sum_{k=1}^n \sum_{k'=0}^{k-1} \eta_k \eta_{k'} J[s_k(t_{k'} - t_k)] \right\}, \tag{E.23}$$

as long as Eq. (E.22) is satisfied.

### E.1.3 Final formula

Once we obtained Eqs. (E.11) and (E.23), the potential across the junction (E.8) becomes

$$\begin{aligned}
 \frac{V_J(t_0)}{V_c} &= \sum_{n=0}^{+\infty} \frac{1}{2i} \left( \frac{iU_0}{2\hbar} \right)^{2n+1} \sum_{\{\eta_k\}}' \sum_{\{s_k\}} \eta_0 \int_{-\infty}^{t_0} dt_1 \int_{-\infty}^{t_1} dt_2 \dots \int_{-\infty}^{t_{2n}} dt_{2n+1} \\
 &\times \exp \left\{ i \frac{\pi}{e} \sum_{k=0}^{2n+1} \eta_k \left[ I_0 t_k + \frac{I_{\text{mw}}}{\omega_{\text{mw}}} \sin(\omega_{\text{mw}} t_k) \right] \right\} \\
 &\times \left( \prod_{k=1}^{2n+1} s_k \right) \exp \left\{ - \sum_{k=1}^{2n+1} \sum_{k'=0}^{k-1} \eta_k \eta_{k'} J[s_k(t_{k'} - t_k)] \right\}, \tag{E.24}
 \end{aligned}$$

if the sum rule (E.22) is used in Eq. (E.18). To get Eq. (E.24) we replaced the index  $n$  with  $2n+1$  because

$$\sum_{k=0}^n \eta_k = \underbrace{\pm 1 \pm 1 \dots \pm 1}_{n+1 \text{ elements}} = 0 \iff (n \text{ is odd}).$$

Note that we used the prime ' symbol in the sum over all  $\eta_k$  configurations in order to indicate that Eq. (E.22) holds.

Equation (E.24) can be recast further as follows. First let us consider the correlation function  $-J(t)$ . As can be noticed from Eq. (E.20), it is the sum of an even real part and an odd imaginary part:

$$-J(t) = \underbrace{\Re[-J(t)]}_{\text{even}} + i \underbrace{\Im[-J(t)]}_{\text{odd}} = M(t) + i \text{sign}(t)A(t)$$

with

$$M(t) = \Re[-J(t)] \quad \text{and} \quad A(t) = \left| \Im[-J(t)] \right|.$$

Writing  $J(t)$  in this way, the following relation holds:

$$-\sum_{k=1}^{2n+1} \sum_{k'=0}^{k-1} \eta_k \eta_{k'} J[s_k(t_{k'} - t_k)] = \sum_{k=1}^{2n+1} \sum_{k'=0}^{k-1} \eta_k \eta_{k'} \left[ M(t_{k'} - t_k) \right] + \sum_{k=1}^{2n+1} i s_k \eta_k g_k. \quad (\text{E.25})$$

To get this expression we used the relation  $\text{sign}[s_k(t_{k'} - t_k)] = \text{sign}(s_k) = s_k$  and we defined the function  $g_k$  as

$$g_k = g(t_k) = \sum_{k'=0}^{k-1} \eta_{k'} A(t_{k'} - t_k). \quad (\text{E.26})$$

We see from Eq. (E.25) that the Keldysh index  $s_k$  appears only in the sum containing  $g_k$ . As a result, Eq. (E.24) contains the term

$$\begin{aligned} & \sum_{\{s_k\}} \left( \prod_{k=1}^{2n+1} s_k \right) \exp \left\{ i \sum_{k=1}^{2n+1} s_k \eta_k g_k \right\} = \\ & = \sum_{s_1=\pm} \dots \sum_{s_{2n+1}=\pm} \left( s_1 \dots s_{2n+1} \right) e^{i s_1 \eta_1 g_1} \dots e^{i s_{2n+1} \eta_{2n+1} g_{2n+1}}. \end{aligned}$$

This last relation is the product of  $2n + 1$  decoupled elements. Each of them is a sine function:

$$\sum_{s_k=\pm} s_k e^{i s_k \eta_k g_k} = e^{i \eta_k g_k} - e^{-i \eta_k g_k} = 2i \sin[\eta_k g_k].$$

Therefore we arrive at the equation

$$\begin{aligned}
& \sum_{\{s_k\}} \left( \prod_{k=1}^{2n+1} s_k \right) \exp \left\{ i \sum_{k=1}^{2n+1} s_k \eta_k g_k \right\} \\
&= (2i)^{2n+1} \prod_{k=1}^{2n+1} \sin [\eta_k g_k] \\
&= (2i)^{2n+1} \frac{1}{\eta_0} \left( \prod_{k=0}^{2n+1} \eta_k \right) \left( \prod_{k=1}^{2n+1} \sin [g_k] \right) \\
&= (2i)^{2n+1} \frac{1}{\eta_0} (-1)^{n+1} \left( \prod_{k=1}^{2n+1} \sin [g_k] \right).
\end{aligned}$$

Inserting it into Eq. (E.24), we finally obtain the series expansion

$$\begin{aligned}
\frac{V_J(t_0)}{V_c} &= \sum_{n=0}^{+\infty} \frac{(-1)^n}{2i} \left( \frac{U_0}{\hbar} \right)^{2n+1} \sum_{\{\eta_k\}}' \int_{-\infty}^{t_0} dt_1 \int_{-\infty}^{t_1} dt_2 \dots \int_{-\infty}^{t_{2n}} dt_{2n+1} \\
&\times \left( \prod_{k=1}^{2n+1} \sin [g_k] \right) \exp \left\{ \sum_{k=1}^{2n+1} \sum_{k'=0}^{k-1} \eta_k \eta_{k'} M(t_{k'} - t_k) \right\} \\
&\times \exp \left\{ i \omega_B \sum_{k=0}^{2n+1} \eta_k t_k \right\} \exp \left\{ i \alpha \sum_{k=0}^{2n+1} \sin(\omega_{mw} \eta_k t_k) \right\}. \quad (\text{E.27})
\end{aligned}$$

where  $\omega_B = \pi I_0/e$  and  $\alpha = \pi I_{mw}/e \omega_{mw}$ . Equation (E.27) is exact at all orders in  $U_0$ .

## E.2 First-order term

In this section, we focus on the first-order term of the quantum mean value Eq. (E.27) and calculate its time average. For  $n = 0$ ,  $\eta_0 = \pm$  and  $\eta_1 = \pm$  are the only dichotomic variables different from zero. The configurations such that  $\eta_0 + \eta_1 = 0$  [see Eq. (E.22)] are two:

$$\{\eta_k\} = \left\{ \left( \eta_0 = -, \eta_1 = + \right); \left( \eta_0 = +, \eta_1 = - \right) \right\}.$$

It follows that Eq. (E.27) gives

$$\frac{V_J^{(0)}(t_0)}{V_c} = \frac{1}{2i} \left( \frac{U_0}{\hbar} \right) \sum_{\{\eta_k\}=2}' \int_{-\infty}^{t_0} dt_1 \sin [g_1] \exp \left\{ \eta_0 \eta_1 M(t_0 - t_1) \right\}$$

$$\times \exp \left\{ i \omega_B (\eta_0 t_0 + \eta_1 t_1) \right\} \exp \left\{ i \alpha \left[ \eta_0 \sin (\omega_{\text{mw}} t_0) + \eta_1 \sin (\omega_{\text{mw}} t_1) \right] \right\}. \quad (\text{E.28})$$

Here  $g_1 = \eta_0 A(t_0 - t_1)$  [see Eq. (E.26)]. If we first write  $\sin [\eta_0 A(t_0 - t_1)]$  in terms of the complex exponential functions, then sum over  $\eta_0 = \pm$  and  $\eta_1 = \pm$  and finally put in evidence  $\exp [\pm i A(t_0 - t_1)]$ , Eq. (E.28) can be written as

$$\begin{aligned} \frac{V_J^{(0)}(t_0)}{V_c} &\simeq \left( \frac{U_0}{4\hbar} \right) \int_{-\infty}^{t_0} dt_1 e^{-M(t_0-t_1)} e^{-iA(t_0-t_1)} \\ &\quad \times \left[ e^{i\omega_B(t_0-t_1)} e^{i\alpha [\sin(\omega_{\text{mw}} t_0) - \sin(\omega_{\text{mw}} t_1)]} - h.c. \right] \\ &+ \left( \frac{U_0}{4\hbar} \right) \int_{-\infty}^{t_0} dt_1 e^{-M(t_0-t_1)} e^{iA(t_0-t_1)} \\ &\quad \times \left[ e^{-i\omega_B(t_0-t_1)} e^{-i\alpha [\sin(\omega_{\text{mw}} t_0) - \sin(\omega_{\text{mw}} t_1)]} - h.c. \right], \quad (\text{E.29}) \end{aligned}$$

i.e., as the sum of two integrals, one the complex conjugate of the other. This last expression can be further recast making the change of variable  $\tau = t_0 - t_1$  in the first integral and  $\tau = -(t_0 - t_1)$  in the second one. Finally we get the first-order quantum mean value

$$\frac{V_J^{(0)}(t_0)}{V_c} = \left( \frac{U_0}{4\hbar} \right) \int_{-\infty}^{+\infty} d\tau e^{J(\tau)} \left\{ e^{i\omega_B \tau} e^{i\alpha \tau_{\text{mw}}} - h.c. \right\} \quad (\text{E.30})$$

with

$$\tau_{\text{mw}} = \sin [\omega_{\text{mw}} (\tau - \text{sign}(\tau) t_0)] + \text{sign}(\tau) \sin [\omega_{\text{mw}} t_0].$$

When the microwave signal is switched off,  $I_{\text{mw}} = 0$ , Eq. (E.30) gives

$$\left. \frac{V_J^{(0)}(t_0)}{V_c} \right|_{I_{\text{mw}}=0} = \frac{V_J^{(\text{DC},0)}}{V_c}(\omega_B) = \left( \frac{U_0}{4\hbar} \right) \int_{-\infty}^{+\infty} d\tau \left\{ e^{J(\tau)} e^{i\omega_B \tau} - e^{J(\tau)} e^{-i\omega_B \tau} \right\}. \quad (\text{E.31})$$

We see that the voltage across the QPSJ is independent of the specific choice of the time  $t_0$  and is determined by the difference between the Fourier transforms of the charge-charge correlation function  $J(\tau)$  [see Eq. (E.20)] for positive and negative bias energy  $\hbar\omega_B$  respectively. This result is dual to the well-known expression of the Cooper-pair current through a Josephson junction in the presence of an external environment [1].

On the other hand, if  $I_{\text{mw}} \neq 0$ , the DC component of Eq. (E.30) can be obtained calculating the integral

$$\frac{1}{T_{\text{mw}}} \int_{t'}^{t'+T_{\text{mw}}} dt_0 \exp \left\{ i \alpha \sin [\omega_{\text{mw}} (\tau - \text{sign}(\tau) t_0)] + i \alpha \text{sign}(\tau) \sin [\omega_{\text{mw}} t_0] \right\},$$

namely the time average over one period of the microwave signal  $T_{\text{mw}} = 2\pi/\omega_{\text{mw}}$ , with  $t'$  an arbitrary initial time. In this last expression, the exponential function can be rewritten in terms of the Bessel functions of the first kind  $J_m(x)$  using the Jacobi-Anger expansion,

$$e^{ia \sin(x)} = \sum_{m=-\infty}^{+\infty} J_m(a) e^{imx}.$$

We straightforwardly find

$$\sum_{m=-\infty}^{+\infty} \sum_{m'=-\infty}^{+\infty} J_m(\alpha) J_{m'}(\alpha) e^{im\omega_{\text{mw}}\tau} \frac{1}{T_{\text{mw}}} \int_{t'}^{t'+T_{\text{mw}}} dt_0 e^{i\omega_{\text{mw}} t_0 \text{sign}(\tau)} (m'-m). \quad (\text{E.32})$$

The integral in Eq. (E.32) is equal to 0 if  $m' \neq m$  and to 1 when  $m' = m$ . As a result, the first-order potential across a current-biased QPS junction under microwave irradiation and embedded in an external electromagnetic environment is

$$\frac{V_J^{(\text{mw},0)}}{V_c}(\omega_B) = \left( \frac{U_0}{4\hbar} \right) \sum_{m=-\infty}^{+\infty} J_m^2(\alpha) \int_{-\infty}^{+\infty} d\tau \left[ e^{J(\tau)} e^{i\omega_B \tau} e^{im\omega_{\text{mw}}\tau} - h.c. \right]. \quad (\text{E.33})$$

Using Eq. (E.31), the voltage Eq. (E.33) becomes

$$\frac{V_J^{(\text{mw},0)}}{V_c}(\omega_B) = \sum_{m=-\infty}^{+\infty} J_m^2(\alpha) \left[ \frac{V_J^{(\text{DC},0)}}{V_c}(\omega_B + m\omega_{\text{mw}}) \right]. \quad (\text{E.34})$$



# Bibliography

- [1] G.-L. Ingold and Y. V. Nazarov, *Single charge tunneling: Coulomb blockade phenomena in nanostructures*, ch. 2. Springer, 1992.
- [2] H. Pothier, S. Guéron, N. O. Birge, D. Esteve, and M. H. Devoret, “Energy distribution function of quasiparticles in mesoscopic wires,” *Phys. Rev. Lett.*, vol. 79, pp. 3490–3493, Nov 1997.
- [3] H. Courtois, M. Meschke, J. T. Peltonen, and J. P. Pekola, “Origin of hysteresis in a proximity Josephson junction,” *Phys. Rev. Lett.*, vol. 101, p. 067002, Aug 2008.
- [4] F. Giazotto, T. T. Heikkilä, A. Luukanen, A. M. Savin, and J. P. Pekola, “Opportunities for mesoscopics in thermometry and refrigeration: Physics and applications,” *Rev. Mod. Phys.*, vol. 78, pp. 217–274, Mar 2006.
- [5] J. M. Rowell and D. C. Tsui, “Hot electron temperature in InAs measured by tunneling,” *Phys. Rev. B*, vol. 14, pp. 2456–2463, Sep 1976.
- [6] D. R. Schmidt, C. S. Yung, and A. N. Cleland, “Nanoscale radio-frequency thermometry,” *Appl. Phys. Lett.*, vol. 83, no. 5, pp. 1002–1004, 2003.
- [7] M. Nahum, T. M. Eiles, and J. M. Martinis, “Electronic microrefrigerator based on a normal-insulator-superconductor tunnel junction,” *Appl. Phys. Lett.*, vol. 65, no. 24, pp. 3123–3125, 1994.
- [8] M. M. Leivo, J. P. Pekola, and D. V. Averin, “Efficient Peltier refrigeration by a pair of normal metal/insulator/superconductor junctions,” *Appl. Phys. Lett.*, vol. 68, no. 14, pp. 1996–1998, 1996.
- [9] A. Kemppinen, M. Meschke, M. Mottonen, D. V. Averin, and J. P. Pekola, “Quantized current of a hybrid single-electron transistor with superconducting leads and a normal-metal island,” *The European Physical Journal Special Topics*, vol. 172, no. 1, pp. 311–321, 2009.

- 
- [10] J. P. Pekola, O.-P. Saira, V. F. Maisi, A. Kemppinen, M. Möttönen, Y. A. Pashkin, and D. V. Averin, “Single-electron current sources: Toward a refined definition of the ampere,” *Rev. Mod. Phys.*, vol. 85, pp. 1421–1472, Oct 2013.
- [11] J. Bardeen, L. N. Cooper, and J. R. Schrieffer, “Theory of superconductivity,” *Phys. Rev.*, vol. 108, pp. 1175–1204, Dec 1957.
- [12] I. Giaever, H. R. Hart, and K. Megerle, “Tunneling into superconductors at temperatures below 1 K,” *Phys. Rev.*, vol. 126, pp. 941–948, May 1962.
- [13] A. F. Andreev, “The thermal conductivity of the intermediate state in superconductors,” *Sov. Phys. JEPT*, vol. 19, p. 1228, 1964.
- [14] G. E. Blonder, M. Tinkham, and T. M. Klapwijk, “Transition from metallic to tunneling regimes in superconducting microconstrictions: Excess current, charge imbalance, and supercurrent conversion,” *Phys. Rev. B*, vol. 25, pp. 4515–4532, Apr 1982.
- [15] V. F. Maisi, O.-P. Saira, Y. A. Pashkin, J. S. Tsai, D. V. Averin, and J. P. Pekola, “Real-time observation of discrete Andreev tunneling events,” *Phys. Rev. Lett.*, vol. 106, p. 217003, May 2011.
- [16] J. P. Pekola, V. F. Maisi, S. Kafanov, N. Chekurov, A. Kemppinen, Y. A. Pashkin, O.-P. Saira, M. Möttönen, and J. S. Tsai, “Environment-assisted tunneling as an origin of the Dynes density of states,” *Phys. Rev. Lett.*, vol. 105, p. 026803, Jul 2010.
- [17] R. C. Dynes, V. Narayanamurti, and J. P. Garno, “Direct measurement of quasiparticle-lifetime broadening in a strong-coupled superconductor,” *Phys. Rev. Lett.*, vol. 41, pp. 1509–1512, Nov 1978.
- [18] T. Greibe, M. P. V. Stenberg, C. M. Wilson, T. Bauch, V. S. Shumeiko, and P. Delsing, “Are “pinholes” the cause of excess current in superconducting tunnel junctions? A study of Andreev current in highly resistive junctions,” *Phys. Rev. Lett.*, vol. 106, p. 097001, Feb 2011.
- [19] O.-P. Saira, M. Möttönen, V. F. Maisi, and J. P. Pekola, “Environmentally activated tunneling events in a hybrid single-electron box,” *Phys. Rev. B*, vol. 82, p. 155443, Oct 2010.
- [20] J. M. Martinis and M. Nahum, “Effect of environmental noise on the accuracy of Coulomb-blockade devices,” *Phys. Rev. B*, vol. 48, pp. 18316–18319, Dec 1993.

- [21] J. M. Hergenrother, J. G. Lu, M. T. Tuominen, D. C. Ralph, and M. Tinkham, “Photon-activated switch behavior in the single-electron transistor with a superconducting island,” *Phys. Rev. B*, vol. 51, pp. 9407–9410, Apr 1995.
- [22] H. Grabert, G.-L. Ingold, and B. Paul, “Phase diffusion and charging effects in Josephson junctions,” *EPL (Europhysics Letters)*, vol. 44, no. 3, p. 360, 1998.
- [23] J. Siewert, Y. V. Nazarov, and G. Falci, “A generalized model of non-thermal noise in the electromagnetic environment of small-capacitance tunnel junctions,” *EPL (Europhysics Letters)*, vol. 38, no. 5, p. 365, 1997.
- [24] F. W. J. Hekking and Y. V. Nazarov, “Interference of two electrons entering a superconductor,” *Phys. Rev. Lett.*, vol. 71, pp. 1625–1628, Sep 1993.
- [25] F. W. J. Hekking and Y. V. Nazarov, “Subgap conductivity of a superconductor-normal metal tunnel interface,” *Phys. Rev. B*, vol. 49, pp. 6847–6852, Mar 1994.
- [26] J. Flowers, “The route to atomic and quantum standards,” *Science*, vol. 306, p. 1324, 2004.
- [27] L. J. Geerligs, V. F. Anderegg, P. A. M. Holweg, J. E. Mooij, H. Pothier, D. Esteve, C. Urbina, and M. H. Devoret, “Frequency-locked turnstile device for single electrons,” *Phys. Rev. Lett.*, vol. 64, pp. 2691–2694, May 1990.
- [28] H. Pothier, P. Lafarge, C. Urbina, D. Esteve, and M. H. Devoret, “Single-electron pump based on charging effects,” *EPL (Europhysics Letters)*, vol. 17, no. 3, p. 249, 1992.
- [29] S. V. Lotkhov, S. A. Bogoslovsky, A. B. Zorin, and J. Niemeyer, “Operation of a three-junction single-electron pump with on-chip resistors,” *Appl. Phys. Lett.*, vol. 78, no. 7, 2001.
- [30] J. J. Vartiainen, M. Mottonen, J. P. Pekola, and A. Kemppinen, “Nanoampere pumping of cooper pairs,” *Appl. Phys. Lett.*, vol. 90, no. 8, pp. –, 2007.
- [31] M. D. Blumenthal, B. Kaestner, L. Li, S. Giblin, T. J. B. M. Janssen, M. Pepper, D. Anderson, G. Jones, and D. A. Ritchie, “Gigahertz quantized charge pumping,” *Nature Phys.*, vol. 3, p. 343, 2007.

- [32] B. Kaestner, V. Kashcheyevs, G. Hein, K. Pierz, U. Siegner, and H. W. Schumacher, “Robust single-parameter quantized charge pumping,” *Appl. Phys. Lett.*, vol. 92, no. 19, pp. –, 2008.
- [33] J. P. Pekola, J. J. Vartiainen, M. Mottonen, O.-P. Saira, M. Meschke, and D. V. Averin, “Hybrid single-electron transistor as a source of quantized electric current,” *Nature Phys.*, vol. 4, p. 120, 2008.
- [34] D. Averin and Y. Nazarov, “Virtual electron diffusion during quantum tunneling of the electric charge,” *Phys. Rev. Lett.*, vol. 65, pp. 2446–2449, 1990.
- [35] D. Averin, A. Korotkov, A. Manninen, and J. Pekola, “Resonant tunneling through a macroscopic charge state in a superconducting single electron transistor,” *Phys. Rev. Lett.*, vol. 78, pp. 4821–4824, 1997.
- [36] D. V. Averin and J. P. Pekola, “Nonadiabatic charge pumping in a hybrid single-electron transistor,” *Phys. Rev. Lett.*, vol. 101, p. 066801, Aug 2008.
- [37] T. Aref, V. F. Maisi, M. V. Gustafsson, P. Delsing, and J. P. Pekola, “Andreev tunneling in charge pumping with SINIS turnstiles,” *EPL (Europhysics Letters)*, vol. 96, no. 3, p. 37008, 2011.
- [38] A. Di Marco, V. F. Maisi, J. P. Pekola, and F. W. J. Hekking, “Leakage current of a superconductor-normal metal tunnel junction connected to a high-temperature environment,” *Phys. Rev. B*, vol. 88, p. 174507, Nov 2013.
- [39] M. Tinkham, *Introduction to Superconductivity*. New York: Dover Publications, Inc., 2 ed., 1996.
- [40] F. W. J. Hekking, L. I. Glazman, K. A. Matveev, and R. I. Shekhter, “Coulomb blockade of two-electron tunneling,” *Phys. Rev. Lett.*, vol. 70, pp. 4138–4141, Jun 1993.
- [41] A. O. Caldeira and A. J. Leggett, “Quantum tunnelling in a dissipative system,” *Ann. Phys.*, vol. 149, p. 374, 1983.
- [42] A. O. Caldeira and A. J. Leggett, “Quantum tunnelling in a dissipative system,” *Ann. Phys.*, vol. 153, p. 445, 1984.
- [43] A. Leggett, S. Chakravarty, A. Dorsey, M. Fisher, A. Garg, and W. Zwerger, “Dynamics of the dissipative two-state system,” *Rev. Mod. Phys.*, vol. 59, p. 1, 1987.

- [44] J. T. Muhonen, M. Meschke, and J. P. Pekola, "Micrometre-scale refrigerators," *Reports on Progress in Physics*, vol. **75**, p. 046501, (2012).
- [45] D. M. Rowe, ed., *CRC Handbook of Thermoelectrics*. CRC Press, (1995).
- [46] A. M. Clark, N. A. Miller, A. Williams, S. T. Ruggiero, G. C. Hilton, L. R. Vale, J. A. Beall, K. D. Irwin, and J. N. Ullom, "Cooling of bulk material by electron-tunneling refrigerators," *Appl. Phys. Lett.*, vol. 86, 2005.
- [47] P. J. Lowell, G. C. O'Neil, J. M. Underwood, and J. N. Ullom, "Macroscale refrigeration by nanoscale electron transport," *Appl. Phys. Lett.*, vol. 102, 2013.
- [48] O. Quaranta, P. Spathis, F. Beltram, and F. Giazotto, "Cooling electrons from 1 to 0.4 K with V-based nanorefrigerators," *Appl. Phys. Lett.*, vol. 98, 2011.
- [49] J. P. Pekola, R. Schoelkopf, and J. Ullom, "Cryogenics on a chip," *Phys. Today*, vol. 57, p. 41, 2004.
- [50] A. J. Manninen, J. K. Suoknuuti, M. M. Leivo, and J. P. Pekola, "Cooling of a superconductor by quasiparticle tunneling," *Appl. Phys. Lett.*, vol. 74, p. 3020, 1999.
- [51] R. C. Dynes, J. P. Garno, G. B. Hertel, and T. P. Orlando, "Tunneling study of superconductivity near the metal-insulator transition," *Phys. Rev. Lett.*, vol. 53, p. 2437, 1984.
- [52] D. Anghel and J. Pekola, "Noise in refrigerating tunnel junctions and in microbolometers," *J. Low Temp. Phys.*, vol. 123, p. 197, 2001.
- [53] F. C. Wellstood, C. Urbina, and J. Clarke, "Hot-electron effects in metals," *Phys. Rev. B*, vol. 49, p. 5942, 1994.
- [54] B. Frank and W. Krech, "Electronic cooling in superconducting tunnel junctions," *Phys. Lett. A*, vol. 235, p. 281, 1997.
- [55] F. Giazotto and J. P. Pekola, "Josephson tunnel junction controlled by quasiparticle injection," *J. Appl. Phys.*, vol. 97, 2005.
- [56] A. V. Timofeev, C. P. Garcia, N. B. Kopnin, A. M. Savin, M. Meschke, F. Giazotto, and J. P. Pekola, "Recombination-limited energy relaxation in a Bardeen-Cooper-Schrieffer superconductor," *Phys. Rev. Lett.*, vol. 102, p. 017003, 2009.

- [57] J. P. Pekola, A. J. Manninen, M. M. Leivo, K. Arutyunov, J. K. Suoknuuti, T. I. Suppala, and B. Collaudin, “Microrefrigeration by quasiparticle tunnelling in NIS and SIS junctions,” *Physica B: Condensed Matter*, vol. 280, p. 485, 2000.
- [58] S. Rajauria, H. Courtois, and B. Pannetier, “Quasiparticle-diffusion-based heating in superconductor tunneling microcoolers,” *Phys. Rev. B*, vol. 80, p. 214521, 2009.
- [59] G. C. O’Neil, P. J. Lowell, J. M. Underwood, and J. N. Ullom, “Measurement and modeling of a large-area normal-metal/insulator/superconductor refrigerator with improved cooling,” *Phys. Rev. B*, vol. 85, p. 134504, 2012.
- [60] H. Q. Nguyen, T. Aref, V. J. Kauppila, M. Meschke, C. B. Winkelmann, H. Courtois, and J. P. Pekola, “Trapping hot quasi-particles in a high-power superconducting electronic cooler,” *New Journal of Physics*, vol. 15, p. 085013, 2013.
- [61] L. M. A. Pascal, A. Fay, C. B. Winkelmann, and H. Courtois, “Existence of an independent phonon bath in a quantum device,” *Phys. Rev. B*, vol. 88, p. 100502, 2013.
- [62] H. Q. Nguyen, L. M. A. Pascal, Z. H. Peng, O. Buisson, B. Gilles, C. B. Winkelmann, and H. Courtois, “Etching suspended superconducting tunnel junctions from a multilayer,” *Appl. Phys. Lett.*, vol. 100, 2012.
- [63] A. Barone and G. Paternò, *Physics and Applications of the Josephson Effect*. New York: John Wiley and Sons, 1982.
- [64] K. K. Likharev, *Dynamics of the Josephson Junctions and Circuits*. London: Gordon and Breach Science Publishers, 1986.
- [65] J. Clarke and A. I. Braginski, *The SQUID Handbook: Applications of the SQUIDS and SQUID Systems, Volume II*. Wiley-VCH, 2006.
- [66] T. A. Fulton, P. L. Gammel, D. J. Bishop, L. N. Dunkleberger, and G. J. Dolan, “Observation of combined Josephson and charging effects in small tunnel junction circuits,” *Phys. Rev. Lett.*, vol. 63, pp. 1307–1310, Sep 1989.
- [67] Y. Makhlin, G. Schön, and A. Shnirman, “Quantum-state engineering with Josephson-junction devices,” *Rev. Mod. Phys.*, vol. 73, p. 357, 2001.
- [68] M. H. Devoret, A. Wallraff, and J. M. Martinis, “Superconducting qubits: A short review,” *arXiv:cond-mat/0411174*, 2004.

- [69] J. Martinis, “Superconducting phase qubits,” *Quantum Inf. Process*, vol. 8, p. 81, 2009.
- [70] T. D. Ladd, F. Jelezko, R. Laflamme, Y. Nakamura, C. Monroe, and J. L. O’Brien *Nature (London)*, vol. 464, p. 45, 2010.
- [71] A. Schmid, “Diffusion and localization in a dissipative quantum system,” *Phys. Rev. Lett.*, vol. 51, p. 1506, 1983.
- [72] M. H. Devoret, J. M. Martinis, and J. Clarke, “Measurements of macroscopic quantum tunneling out of the zero-voltage state of a current-biased Josephson junction,” *Phys. Rev. Lett.*, vol. 55, pp. 1908–1911, Oct 1985.
- [73] A. Leggett and A. Garg, “Quantum mechanics versus macroscopic realism: Is the flux there when nobody looks?,” *Phys. Rev. Lett.*, vol. 54, pp. 857–860, Mar 1985.
- [74] G. Schön and A. Zaikin, “Quantum coherent effects, phase transitions, and the dissipative dynamics of ultra small tunnel junctions,” *Phys. Rep.*, vol. 198, p. 237, 1990.
- [75] A. J. Leggett, “Testing the limits of quantum mechanics: motivation, state of play, prospects,” *Journal of Physics: Condensed Matter*, vol. 14, no. 15, p. R415, 2002.
- [76] M. Schlosshauer, *Decoherence and the Quantum-To-Classical Transition*. Springer Ed., 2010.
- [77] U. Weiss, *Quantum Dissipative Systems*. Singapore: World Scientific Publishing, 4 ed., 2012.
- [78] R. Kautz, “Noise, chaos, and the Josephson voltage standard,” *Reports on Progress in Physics*, vol. 59, p. 935, 1996.
- [79] S. Shapiro, “Josephson currents in superconducting tunneling: The effect of microwaves and other observations,” *Phys. Rev. Lett.*, vol. 11, p. 80, 1963.
- [80] S. Shapiro, A. Janus, and S. Holly, “Effect of microwaves on Josephson currents in superconducting tunneling,” *Rev. Mod. Phys.*, vol. 36, p. 223, 1964.
- [81] B. Taylor, W. Parker, and D. Langerberg, “Determination of  $\frac{e}{h}$ , using macroscopic quantum phase coherence in superconductors: Implications for quantum electrodynamics and the fundamental physical constants,” *Rev. Mod. Phys.*, vol. 41, p. 375, 1969.

- [82] C.A.Hamilton *Review of Scientific Instruments*, vol. 71, p. 3611, 2000.
- [83] H. Scherer and B. Camarota *Measurement Science and Technology*, vol. 23, p. 124010, 2012.
- [84] J. Kohlmann and R. Behr, *Superconductivity - Theory and Applications*. InTech, 2011.
- [85] K. K. Likharev and A. Zorin, "Theory of the Bloch-wave oscillations in small Josephson junctions," *J. Low Temp. Phys.*, vol. 59, p. 347, 1985.
- [86] K. K. Likharev and A. Zorin, "Bloch oscillations in small Josephson junctions: Possible fundamental standard of DC current and other applications," *IEEE Trans. Magn.*, vol. 21, p. 943, 1985.
- [87] D. V. Averin, A. B. Zorin, and K. K. Likharev, "Bloch oscillations in small Josephson junctions," *Sov. Phys. JETP*, vol. 61, p. 407, 1985.
- [88] D. Averin, Y. Nazarov, and A. Odintsov, "Incoherent tunneling of the Cooper pairs and magnetic flux quanta in ultrasmall Josephson junctions," *Physica B*, vol. 165, p. 945, 1990.
- [89] J. E. Mooij, T. P. Orlando, L. Levitov, L. Tian, C. H. van der Wal, and S. Lloyd, "Josephson persistent-current qubit," *Science*, vol. 285, p. 1036, 1999.
- [90] J. E. Mooij and C. J. P. M. Harmans, "Phase-slip flux qubits," *New J. Phys.*, vol. 7, p. 219, 2005.
- [91] J. Mooij and Y. Nazarov, "Superconducting nanowires as quantum phase-slip junctions," *Nature Physics*, vol. 2, p. 169, 2006.
- [92] A. Zazunov, N. Didier, and F. W. J. Hekking, "Quantum charge diffusion in underdamped Josephson junctions and superconducting nanowires," *Europhysics Letters*, vol. 83, p. 47012, 2008.
- [93] W. Guichard and F. W. J. Hekking, "Phase-charge duality in Josephson junction circuits: role of inertia and effect of microwave irradiation," *Phys. Rev. B*, vol. 81, p. 064508, 2010.
- [94] K. A. Matveev, A. I. Larkin, and L. I. Glazman, "Persistent current in superconducting nanorings," *Phys. Rev. Lett.*, vol. 89, p. 096802, Aug 2002.
- [95] I. M. Pop, I. Protopopov, F. Lecocq, Z. Peng, B. Pannetier, O. Buisson, and W. Guichard, "Measurement of the effect of quantum phase slips in a Josephson junction chain," *Nature Physics*, vol. 6, p. 589, 2010.

- [96] G. Rastelli, I. M. Pop, and F. W. J. Hekking, “Quantum phase slips in Josephson junction rings,” *Phys. Rev. B*, vol. 87, p. 174513, May 2013.
- [97] T. Weißl, G. Rastelli, I. Matei, I. M. Pop, O. Buisson, F. W. J. Hekking, and W. Guichard, “Bloch band dynamics of a Josephson junction in an inductive environment,” *arXiv:1407.7728*, 2014.
- [98] A. M. Hriscu and Y. V. Nazarov, “Model of a proposed superconducting phase slip oscillator: A method for obtaining few-photon nonlinearities,” *Phys. Rev. Lett.*, vol. 106, p. 077004, 2011.
- [99] A. M. Hriscu and Y. V. Nazarov, “Coulomb blockade due to quantum phase slips illustrated with devices,” *Phys. Rev. B*, vol. 83, p. 174511, 2011.
- [100] M. Vanević and Y. V. Nazarov, “Quantum phase slips in superconducting wires with weak inhomogeneities,” *Phys. Rev. Lett.*, vol. 108, p. 187002, 2012.
- [101] O. Astafiev, L. B. V. Ioffe, S. Kafanov, Y. A. Pashkin, K. Y. Arutyunov, D. Shahar, O. Cohen, and J. S. Tsai, “Coherent quantum phase slip,” *Nature*, vol. 484, p. 355, 2012.
- [102] T. T. Hongisto and A. B. Zorin, “Single-charge transistor based on the charge-phase duality of a superconducting nanowire circuit,” *Phys. Rev. Lett.*, vol. 108, p. 097001, Feb 2012.
- [103] C. H. Webster, J. C. Fenton, T. T. Hongisto, S. P. Giblin, A. B. Zorin, and P. A. Warburton, “Nbsi nanowire quantum phase-slip circuits: dc supercurrent blockade, microwave measurements, and thermal analysis,” *Phys. Rev. B*, vol. 87, p. 144510, Apr 2013.
- [104] J. T. Peltonen, O. Astafiev, Y. P. Korneeva, B. M. Voronov, A. A. Korneev, I. M. Charaev, A. V. Semenov, G. N. Golt’sman, L. B. Ioffe, T. M. Klapwijk, and J. S. Tsai, “Coherent flux tunneling through nbn nanowires,” *Phys. Rev. B*, vol. 88, p. 220506, 2013.
- [105] I. Safi, “Time-dependent transport in arbitrary extended driven tunnel junctions,” *arXiv:cond-mat/1401.5950v1*, 2014.
- [106] W. Zwerger, “Quantum effects in the current-voltage characteristic of a small Josephson junction,” *Phys. Rev. B*, vol. 35, p. 4737, 1987.
- [107] G.-L. Ingold and H. Grabert, “Effect of zero point phase fluctuations on Josephson tunneling,” *Phys. Rev. Lett.*, vol. 83, p. 3721, 1999.

- [108] G.-L. Ingold, H. Grabert, and U. Eberhardt, “Cooper-pair current through ultrasmall Josephson junctions,” *Phys. Rev. B*, vol. 50, p. 395, 1994.
- [109] J. S. Lehtinen, T. Rantala, and K. Y. Arutyunov, “Coulomb blockade and Bloch oscillations in superconducting Ti nanowires,” *Phys. Rev. Lett.*, vol. 109, p. 187001, 2012.
- [110] L. V. Keldysh, “Diagram technique for nonequilibrium processes,” *Sov. Phys. JETP*, vol. 20, p. 1018, 1965.
- [111] J. Rammer, *Quantum Field Theory of Non-Equilibrium States*. Cambridge University Press, 2007.
- [112] A. Kamenev, *Field Theory of Non-Equilibrium Systems*. Cambridge University Press, 2011.